UC Berkeley
UC Berkeley Electronic Theses and Dissertations

Title
Membrane Curvature Sensing and Stabilization in Macroautophagy

Permalink
https://escholarship.org/uc/item/16t2k5wr

Author
Jensen, Liv E

Publication Date
2023

Peer reviewed|Thesis/dissertation

Membrane Curvature Sensing and Stabilization in Macroautophagy

By

Liv Elisabeth Jensen

A dissertation submitted in partial satisfaction of the

requirements for the degree of

Doctor of Philosophy

in

Molecular and Cell Biology

in the

Graduate Division

of the

University of California, Berkeley

Committee in charge:

Professor James H. Hurley, Chair
Professor David G. Drubin
Professor Daniel A. Fletcher
Professor Alanna Schepartz

Summer 2023

Abstract

Membrane Curvature Sensing and Stabilization in Macroautophagy

by

Liv Elisabeth Jensen

Doctor of Philosophy in Molecular and Cell Biology

University of California, Berkeley

Professor James H. Hurley, Chair

A fundamental question in the central cellular recycling pathway of macroautophagy (hereafter autophagy) is how the autophagosome membrane is shaped around its cargo. At its heart, autophagosome biogenesis is a membrane remodeling event that sequesters cytoplasmic inclusions targeted for lysosomal degradation. And, while the biochemical basis for the recruitment of core autophagy proteins and individual subreactions has been largely worked out, critically, the physical mechanisms for membrane engulfment of cargo have yet to be elucidated. Among the most important outstanding questions are how membrane shape participates in the recruitment of early autophagy proteins and how the highly curved phagophore membrane is stabilized during autophagy initiation.

Here, we use in vitro reconstitution on membrane nanotubes investigate how core autophagy proteins in the LC3 lipidation cascade and PI3K kinase complexes interact with curved membranes, providing insight into the possible roles in regulating membrane shape during autophagosome biogenesis. I found that ATG12–ATG5-ATG16L1 was up to 100-fold enriched on highly curved nanotubes relative to flat membranes. At high surface density, ATG12–ATG5-ATG16L1 binding increased the curvature of the nanotubes. While WIPI2 binding directs membrane recruitment, the amphipathic helix α2 of ATG16L1 is responsible for curvature sensitivity. Molecular dynamics simulations revealed that helix α2 of ATG16L1 inserts shallowly into the membrane, explaining its curvature-sensitive binding to the membrane. These observations show how the binding of the ATG12–ATG5-ATG16L1 complex to the early phagophore rim could stabilize membrane curvature and facilitate autophagosome growth. Further, reconstitution of the Class III PI3K complexes on membrane nanotubes shows that both Complex I and Complex II are similarly curvature sensitive, opening questions about the role of membrane curvature in the differential regulation of PI3K complex localization and regulation in the cell. Finally, these insights were facilitated by improvements and simplifications to existing membrane tube and *in vitro* reconstitution methods, which accelerated the work of precise biophysical quantification. Together, this work provides mechanistic insight into the physical basis of membrane remodeling in autophagosome biogenesis.

To my family.

If you could get a packet of creativity and buy it somewhere, that would be the ideal thing.

-Sydney Brenner

Table of Contents

List of Figures

List of Tables

Acknowledgements

Chapter 1: Physical mechanisms of phagophore expansion in macroautophagy

Introduction

Macroautophagy, hereafter autophagy, is the process in which cytosolic cargoes such as protein aggregates, damaged organelles, intracellular pathogens, or bulk cytoplasm are engulfed in a double-membrane vesicle and targeted to the lysosome for degradation (Mizushima et al., 2011). Autophagic dysfunction results in defects in the clearance of aggregates and damaged organelles, contributing to human neurodegenerative diseases, including Parkinson's Disease (Klionsky et al., 2021; Pickrell & Youle, 2015). During cargo engulfment, the cup-shaped phagophore grows progressively larger (Hayashi-Nishino et al., 2009) and ultimately closes into the double-membraned autophagosome. The past few years have brought rapid progress in understanding how autophagy is initiated, cargo selected, and lipids are sourced and transferred for autophagosome expansion (Chang, Jensen, et al., 2021; Melia et al., 2020; Nakatogawa, 2020). In this context, the physical mechanism of membrane shaping and stabilization during autophagosome growth remains one of the most prominent open questions. Additionally, the process of membrane remodeling that enables trafficking of source vesicles to the nascent autophagosome remains an important unsolved puzzle.

During autophagosome biogenesis, autophagic cargo receptor proteins are first recruited to cytosolic cargoes. This promotes the recruitment of the core autophagy machinery, including the ULK1 protein kinase complex, the Class III phosphatidyl-inositol-3-phosphate kinase (PI3K) Complex I, and the LC3 lipidation machinery. LC3 family proteins are covalently tethered to the phagophore membrane and promote its association to many core autophagy proteins and to the autophagic cargo. The phagophore expands around cargo, and ultimately ESCRT proteins are recruited to close the phagophore around cargo, yielding a double membrane vesicle, the autophagosome. Autophagosomes subsequently fuse with lysosomes, and their contents degraded.

In a membrane-centered view, autophagosomes grow from seed vesicles into membrane sheets which grow, wrap, and finally fully engulf autophagic cargo (Figure 1.2). Electron microscopy has revealed that autophagosomes are large intracellular structures, with a diameter of 100's to 1000's of nanometers (Nguyen et al., 2017). Autophagosome biogenesis takes place on a timescale of 10's of minutes, and the membrane intermediates in autophagosome biogenesis form cup-like structures with a highly curved rim (Bieber et al., 2022). Intermediate snapshots of autophagosome biogenesis provide a framework for understanding cargo engulfment in autophagy, yet the mechanism by which the phagophore is shaped around autophagic cargo remains unknown.

Energetic constraints on phagophore expansion

To understand how cargo is engulfed in an autophagosome, it is critical to understand the physical mechanism and energetic requirements for phagophore expansion. In a simple model of autophagosome biogenesis, three main constraints on phagophore expansion can be considered: (1) lipid flux into the nascent phagophore from a lipid source/donor, (2) adhesion between the phagophore membrane and the autophagic cargo, and (3) membrane bending as the phagophore engulfs cargo. Here, the current state of our understanding of how these three parameters influence phagophore expansion around cargo is discussed.
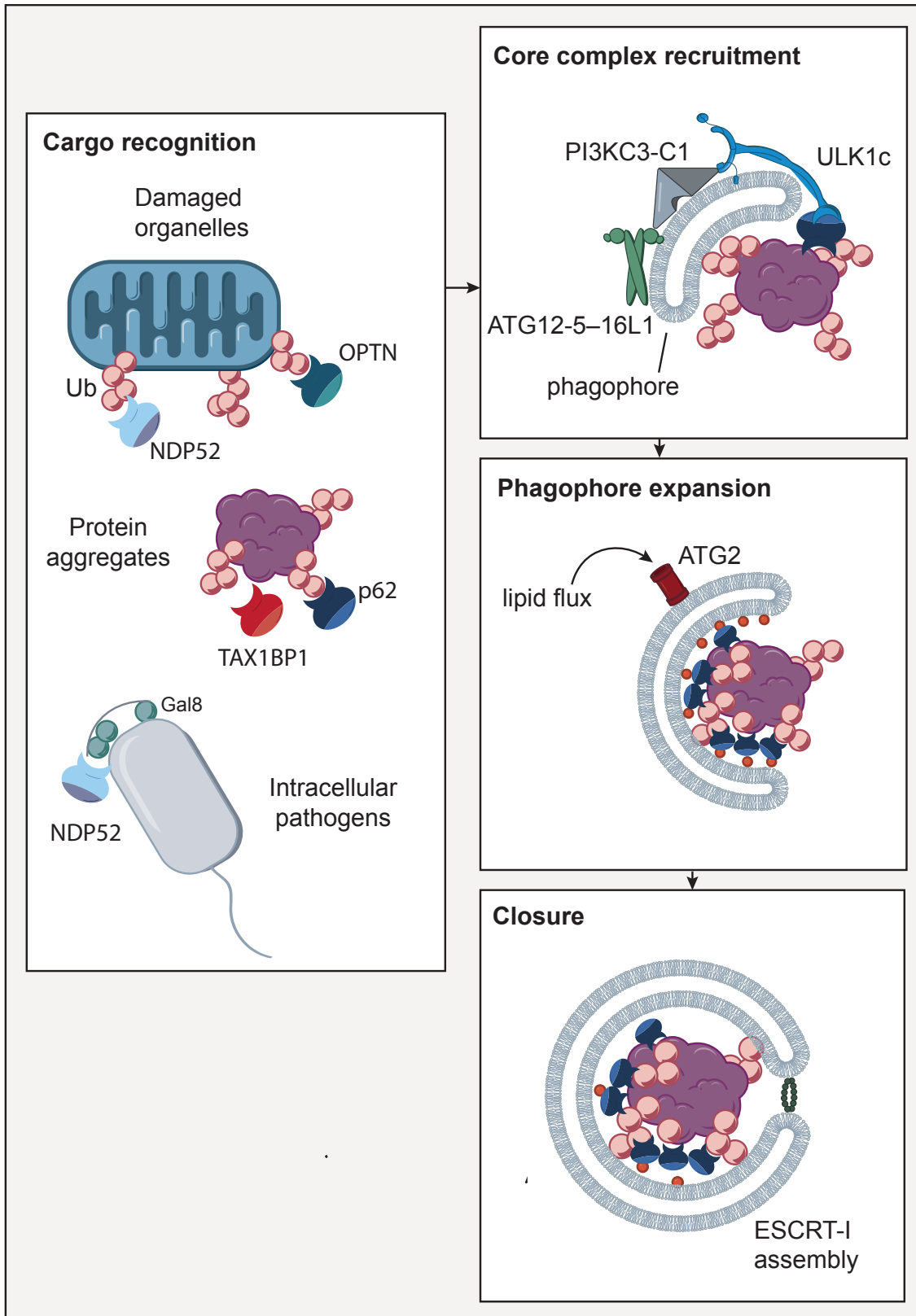
Figure 1.1 Overview of autophagosome biogenesis
Autophagosome biogenesis proceeds in four steps from cargo recognition to core complex recruitment, phagophore expansion, and ESCRT-mediated closure.
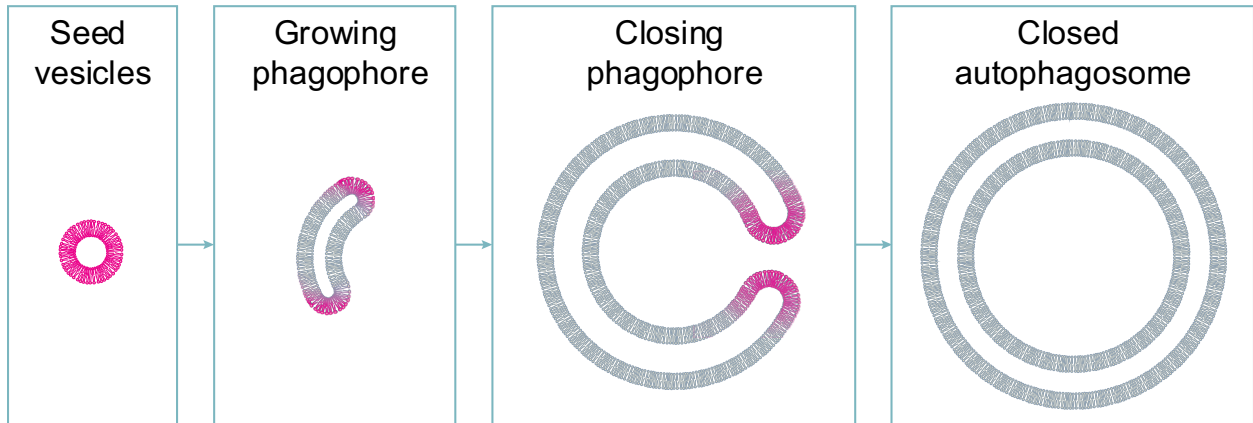
Figure 1.2 Membrane intermediates in autophagosome biogenesis
Autophagosomes grow from seed vesicles which expand into a membrane sheet, which engulfs cargo, ultimately closing to form a double membrane vesicle. Membrane shape changes over the course of autophagosome biogenesis, magenta highlights show regions of high curvature on seed vesicles, growing membrane sheets, and closing cup-shaped phagophores.

Lipid flux into the phagophore

Growth of the phagophore membrane requires input of lipids from other donor membranes in the cell, which in mammalian cells happens through the coordinated action of two central autophagy proteins, ATG2A and ATG9A, together with lipid biosynthesis machinery (Schutter et al., 2020). The initial membrane seeds have been shown in yeast to come from Atg9 vesicles which originate at the Golgi (Sawa-Makarska et al., 2020; Yamamoto et al., 2012). Atg9 vesicles traffic to contact sites with the endoplasmic reticulum (ER) which for the sites of autophagosome biogenesis (Hayashi-Nishino et al., 2009; Yla-Anttila et al., 2009). There, direct lipid transport from the ER into the phagophore is mediated by ATG2A (Maeda et al., 2019; Osawa et al., 2019). ATG9A is a lipid scramblase which drives equilibration of ER-derived lipids between the inner and outer leaflets of the phagophore (Maeda et al., 2020; Matoba et al., 2020). ATG9A scramblase activity is essential for phagophore membrane expansion; in the absence of ATG9A, lipid flux through ATG2A would promote expansion of only the outer leaflet of the phagophore and would eventually create an insurmountable asymmetry between the inner and outer leaflets of the membrane. Thus, at the outset, the rate at which the phagophore can expand is limited by the maximal flux of lipids into the phagophore through ATG2A, the maximal rate of lipid scrambling by ATG9A, and the maximal rate of lipid synthesis at the ER. Modeling of the apparent maximal rates for lipid flux into the phagophore has shown that these rates agree in large part with physiological measurements (von Bülow & Hummer, 2020).

In vitro activity assays of ATG2A and ATG9A have shown that both proteins are active independent of nucleotide hydrolysis, and structural studies have demonstrated their lack of a nucleotide binding pocket. It follows that without nucleotide hydrolysis, ATG2A and ATG9A are only competent to mediate lipid flux down a concentration gradient, and therefore could not support phagophore growth against an energetic barrier, such as posed by the highly curved phagophore rim, discussed below. That is, there must be some other force driving phagophore expansion around cargo, which ATG2A and ATG9A passively accommodate.

Phagophore-cargo adhesion

The second factor influencing phagophore expansion around cargo, relevant in selective autophagy, is phagophore-cargo adhesion. Phagophore-cargo adhesion is achieved at least in part through interactions between the ATG8 proteins tethered to the phagophore and cargo receptor proteins, including p62, NDP52, OPTN, NBR1, and TAX1BP1 (Johansen & Lamark, 2020). In mammals, there are six ATG8 proteins (LC3A-C, GABARAP, -L1, -L2) which become covalently linked through their c-terminal glycine to phosphatidylethanolamine (PE) lipid headgroups in the phagophore membrane through the coordinated action of an E1/E2/E3-like conjugation system comprising ATG7, ATG3, and the ATG12–5-16L1 complex. ATG8 proteins contain a ubiquitin fold and interact with many autophagy proteins, including cargo receptors, through a conserved LC3 Interacting Region (LIR) motif. Canonical LIR motifs contain a central four-amino-acid sequence, [W/F/Y]-X-X-[L/I/V], and interact with ATG8 proteins with dissociation constants in the range of low micromolar to high nanomolar (Wirth et al., 2019).

There are several ways in which phagophore-cargo adhesion could impact phagophore expansion around cargo. First, and most simply, this adhesion specifies the direction of phagophore cup expansion (i.e., towards cargo rather than towards cytoplasm). In a simple

model of cargo engulfment, this interaction has been described in terms of a wetting phenomenon, in which a cargo droplet preferentially interacts with the phagophore rather than the cytoplasm, and in which the phagophore acts as a deformable surface which is wetted by the autophagic cargo droplet (Agudo-Canalejo et al., 2021). This directional bending occurs only if the adhesion between the phagophore and cargo is stronger than that of the phagophore and the cytoplasm, or if there is a difference between the spontaneous curvatures of the inner and outer phagophore membranes. Piecemeal autophagy (sequestration of some, but not all, of a cargo droplet) can occur when surface tension or deformability of the droplet are modified relative to the deformability of the phagophore membrane. Alternatively, in the case of a relatively very deformable cargo droplet, the wetting energy may not be sufficient to induce phagophore bending towards the cargo.

The second way in which cargo adhesion could influence phagophore expansion is through a progressive ratcheting mechanism of the leading edge of the phagophore towards the cargo. Consider the cargo as a surface to which the phagophore membrane becomes progressively attached. At the edges of the wetted surface are un-bound ATG8 proteins on the surface of the phagophore and un-bound cargo receptor proteins on the surface of the cargo. In this model, with thermal fluctuations, the phagophore stochastically moves towards or away from the cargo, making new attachments when it comes close to cargo. Because there are many ATG8-receptor interactions adhering the phagophore to the cargo, these new attachments are effectively permanent, as they act through an avidity-like effect to retain the phagophore membrane in close proximity to the cargo.

In a model of phagophore expansion, this ratcheting mechanism could in principle generate a treadmilling mode of successive membrane adhesion close to the phagophore rim, which would draw new lipids into the phagophore through ATG2A and ATG9A. Such treadmilling would require either local lipidation of ATG8 proteins at the phagophore rim, or ATG8 proteins that are lipidated to the outer phagophore membrane would have to move across the highly curved rim to contact cargo receptor proteins. Both possibilities bring up interesting unresolved questions about the occupancy and ultrastructure of the phagophore rim. In particular, several recent studies suggest that there are specific autophagy proteins that preferentially associate with the phagophore rim (Le Bars et al., 2014; Sakai et al., 2020). These rim-resident proteins could present a diffusive barrier for ATG8 proteins on the outer phagophore surface to cross the phagophore rim. Alternatively, because it is known that the ATG8 lipidation machinery is not captured in the lumen of the autophagosome, ATG8 lipidation occurring locally at the phagophore rim would require a mechanism for the retention of the lipidation machinery at the phagophore rim as the phagophore membrane expands through treadmilling. Understanding which proteins occupy the phagophore rim space, and at what surface density, will be an interesting continuing area of research.

Notably, autophagy also occurs in the absence of any solid or droplet-like cargo. In bulk autophagy, the phagophore instead engulfs cytoplasm without any preferential adhesion to its contents. Because bulk autophagy robustly engulfs cytoplasm in the absence of cargo adhesion, it follows that cargo-phagophore adhesion is not an essential driving force for phagophore expansion, and other mechanisms must exist to thermodynamically drive phagophore engulfment of cargo.

Membrane morphology

The third and final energetic input in this simplified model of phagophore expansion around cargo is the contribution of membrane energy, comprised of both membrane bending and stretching energies. Because membrane shape is dynamic during autophagosome biogenesis, it is of particular importance to address the mechanism by which the phagophore is shaped, and the energetic barrier membrane curvature poses to phagophore expansion. To do this, it is necessary to first discuss the behavior of membranes from a thermodynamic perspective.

Biological membranes can take on a variety of shapes, description of which is aided greatly by a discussion of surface curvature (Figure 1.3). Consider that a membrane approximates a planar surface (x,y) which can be deformed in smooth curves in the z direction. The curvature of the surface at any point can be described by two principal curvatures at that point. The principal curvatures are the slopes of the surface with respect to the tangential plane at two orthogonal axes of curvature. Describing the surface curvature in this way thus defines a set of curvature types at any given point across the surface: flat, spherical, cylindrical, and saddle curvature. Here, flat curvature describes the case where both principal curvatures are zero. Spherical curvature occurs where both principal curvatures have the same sign (i.e. the surface tends above or below the tangential plane for both axes) (Figure 1.3A). Vesicles are an example of a biological membrane with spherical curvature. A surface with cylindrical curvature occurs has one principal curvature equal to zero, like a membrane tube (Figure 1.3B). Finally, saddle curvature occurs at points where the 2 principal curvatures have opposing signs, which occurs in a biological setting at points of membrane constriction, for instance at intermediate shapes preceding membrane scission (Figure 1.3C).

The thermodynamics of membrane morphology were described by Canham and Helfrich in continuum models of membrane bending (Canham, 1970; Helfrich, 1973). Their models succinctly describe how the energy of an entire membrane system is the sum over every infinitesimally small piece of membrane area (dA) of the membrane bending energy (κ), the energy input required to deform a membrane away from its spontaneous curvature. Consider how easily a sheet of notepaper is bent compared with a sheet of construction paper, paperboard, or cardboard. Each kind of paper has a different bending rigidity– if the paper is released, it will relax back to its preferred flat curvature.

At the scale of a biological membrane like a phagophore, organelle, or cell membrane, bending also requires energetic input. A derivation from first principles and using a few heuristics estimates that the energy required to bend a membrane is on the order of 20 k_BT (Deserno, 2007, 2015). This is close enough to thermal energy that small interventions with respect to membrane shape, like protein insertion into the membrane or leaflet asymmetry, are sufficient to alter membrane morphology, but energetically costly enough that membranes do not spontaneously remodel themselves in an unregulated manner.

Typical biological membranes have a thickness of approximately 10 nm, and the smallest possible vesicle size is approximately two times this thickness. Cryo-electron tomography analysis of phagophore intermediates demonstrates that the phagophore rim is among the most stridently curved membrane surfaces within the cell, with a mean intermembrane spacing
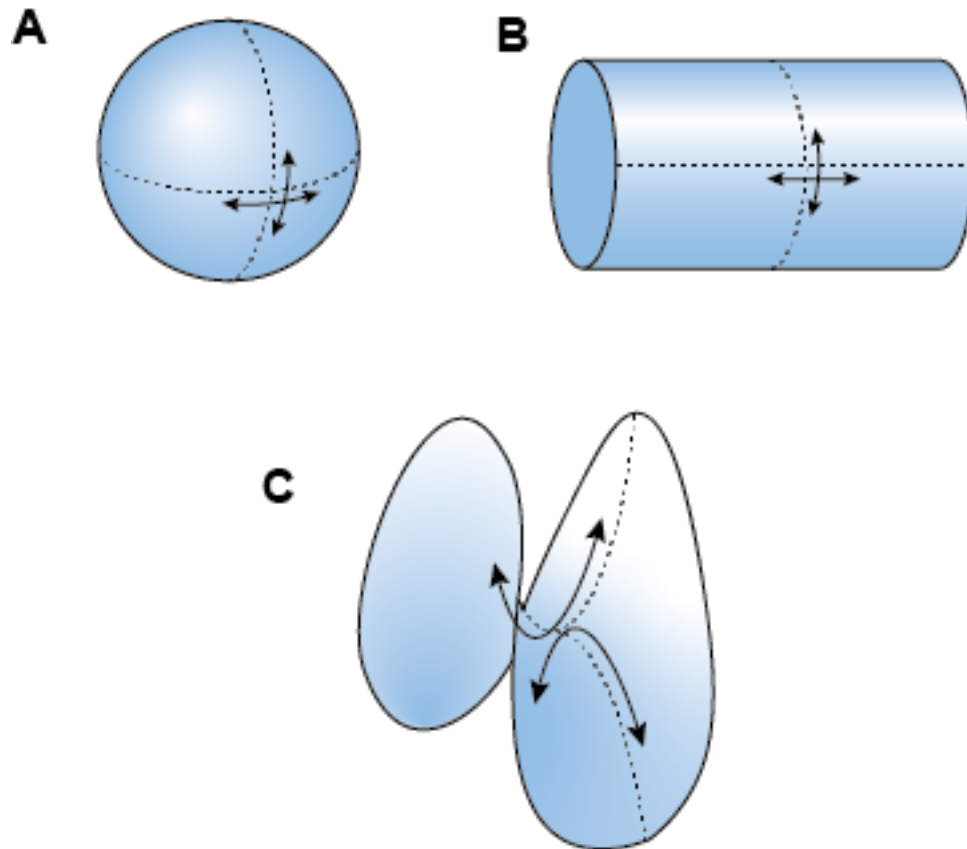
Figure 1.3 Surface curvature
The curvature of a surface is defined by the 2 principal curvatures of that surface, orthogonal to each other and to the surface normal. (**A**) For spherical surfaces, both principal curvatures are positive. (**B**) Tubular or cylindrical surfaces have positive and neutral curvature. (**C**) Saddle points have both positive and negative principal curvatures.

(measured from the center of one bilayer to the center of the other) of 9-11nm (Bieber et al., 2022). Derivations of membrane bending energy show that bending energy scales with the square of the radius of curvature of the membrane. So, as the radius of curvature of a membrane decreases, the energy input required to deform a flat membrane into that shape increases, up to the limit of the highest curvature possible for a membrane. It follows that the high curvature of the phagophore rim is an energetically costly intermediate structure in autophagosome biogenesis.

Combining the vocabulary of membrane curvature and an understanding of membrane energetics enables a description of membrane morphology in autophagosome biogenesis. The phagophore initiates from ATG9 vesicles, which are highly curved along both principal axes of curvature, having a diameter of approximately 50 nm (Park et al., 2023). Because ATG9 vesicles and early phagophores are so highly curved, this membrane curvature could serve as a recruitment platform for early autophagy proteins.   Indeed, several early-acting core autophagy proteins have been shown to preferentially interact with highly curved vesicles (Fan et al., 2011; Lystad et al., 2019; Nath et al., 2014; Ragusa et al., 2012). One intriguing model for the role these curvature sensors play in early autophagosome biogenesis is nucleating initiation sites through a scaffolding mechanism (Ragusa et al., 2012).

As the phagophore expands through lipid flux through ATG2A and ATG9A, it forms a cup-shaped intermediate with low negative curvature on the inner face and low positive curvature on the outer face . Along the rim of the cup-shaped phagophore, the membrane is highly curved. Because the diameter of the phagophore cup is much larger than the thickness of the rim, curvature along the phagophore rim is approximately cylindrical. In this simplified model of phagophore expansion, the phagophore rim at this point represents an energetically expensive intermediate. Modeling phagophore engulfment of a spherical cargo shows how engulfment of the first half of the cargo requires expansion of the phagophore rim circumference, which reaches a maximum at 50% of the cargo engulfed, after which the phagophore rim shrinks as the cargo is further engulfed (**Error! Reference source not found.**). The changing circumference of the phagophore rim therefore represents a dynamic energetic cost during autophagic cargo engulfment. During the initial engulfment of cargo, expansion of the highly curved phagophore rim costs an energetic penalty, which increases at a decreasing rate, while in later stages of engulfment, contraction of the phagophore rim is energetically favorable. As cargo becomes almost entirely engulfed in the phagophore membrane, the phagophore rim shrinks to become a pore with saddle curvature. At this point, energy input is again required to catalyze the scission of the inner surface of the phagophore from the outer, creating the inner and outer membranes of the autophagosome.

Throughout cargo engulfment, the phagophore membrane takes on several distinct morphologies that require energy input. This raises the question of by what mechanism the growing phagophore is shaped. Curvature generation in biological membranes has been extensively studied, and several well-characterized modes of curvature generation are outlined below.

Mechanisms of membrane curvature generation

Biological membranes can be shaped by proteins, or they may have intrinsic curvature. For instance, asymmetries in the phosopholipid bilayer can drive membrane curvature. A commonly discussed mechanism for bilayer asymmetry is the asymmetric distribution of cone-shaped lipids. Many phospholipids such as phosphocholine are approximately cylindrical, and so distribute evenly in the bilayer. However, other phospholipids have smaller or larger headgroups, giving them a conical cross-section in the plane of the membrane, and creating differential pressure at different distances from the bilayer midline (Campelo et al., 2008; Deserno, 2007). Differential enrichment of conical lipids like phosphoethanolamine and phosphoglycerol in the inner and outer leaflets of a membrane can lead to intrinsic curvature of the membrane towards the smaller headgroups, as these headgroups pack more closely together.

The other common way that membrane curvature is generated is through interaction with membrane-shaping proteins (Simunovic et al., 2016). Several mechanisms have been shown to mediate protein-induced membrane bending, including **scaffolding** by curved proteins, protein **insertion** into the membrane, and curvature induction by **intrinsically disordered regions**. Much of the discussion of curvature-generating proteins overlaps with curvature-sensing proteins. To clarify, curvature-sensing and curvature-generating are two modes of the same activity by proteins, differing only in the surface density of the curvature-sensor/generator. At low surface densities, proteins act as curvature sensors, preferentially occupying curved regions of membrane. At high surface densities, the same motifs that enable curvature sensing act in close proximity to one another to exert a bending force upon the membrane itself. It is interesting to consider how strongly proteins sense/induce membrane curvature; this will be discussed further, below.

Curved proteins have been shown to **scaffold** membrane budding events in the cell (Cail & Drubin, 2023) . In a scaffolding mechanism, a membrane interacting protein with a curved shape interacts with the membrane along its curved face, thereby deforming the membrane to the shape of the protein. Some scaffolding proteins have been shown to oligomerize into higher order assemblies that coordinate the large-scale remodeling of membranes into vesicles (e.g. COPII) or tubes (e.g. AP-1) (Hooy et al., 2022). The mechanism of specification of spherical or cylindrical membrane curvature by scaffolding proteins remains an interesting outstanding question: perhaps the ordered assembly of curvature generators dictates the resulting curvature of the membrane. In a similar vein, could disruption of a cylindrical protein scaffold catalyze the transition to spherical curvature?

Other curvature inducing proteins do so through **insertion** of an amphipathic helix or hydrophobic loop into the outer leaflet of a membrane. Insertion of a portion of the protein into the bilayer acts as an inclusion, generating additional pressure on the outer leaflet relative to the inner leaflet. This leaflet asymmetry results in the membrane bending away from the protein-bound leaflet. The amphipathic helix is a common membrane interacting motif, which has been shown to mediate curvature sensing activity of several proteins. Additionally, mutational analysis and modeling has shown how particular properties of amphipathic helices promote more or less curvature induction. Of note, shallow insertion of an amphipathic helix into the membrane has been shown to induce membrane curvature more strongly than deeper insertion

(Campelo et al., 2008). Additionally, basic residues flanking the hydrophobic face of an amphipathic helix promote interaction with acidic lipid headgroups in the membrane, promoting curvature sensing activity(Drin & Antonny, 2010).

Some proteins, such as BAR domain-containing proteins, generate curvature through a combination of scaffolding and insertion mechanisms (Simunovic et al., 2016). BAR domains are banana-shaped protein folds which are thought to mold membrane curvature to their curved surface, in addition to inserting into the membrane at the distal ends of the domain. BAR proteins are among the strongest of known membrane curvature sensors/inducers, and have been implicated in a nmber of membrane remodeling events in the cell. In a similar mechanism, some proteins achieve potent curvature sensitivity through the concatenation of multiple amphipathic helices. The connection of multiple amphipathic helices in ArfGAP1 has been shown to be critical for its potent membrane curvature sensitivity (Mesmin et al., 2007). Multimerization of curvature sensing motifs could be general mechanism for increasing curvature sensitivity of membrane associating proteins.

Finally, some curvature sensing proteins do so through the activity of **intrinsically disordered regions** (IDRs) (Busch et al., 2015; Snead & Stachowiak, 2018). Biophysical characterization of IDR-containing curvature sensors has shown how curvature sensitivity is dependent on the size of the IDR (Zeno et al., 2019). This led to a model in which IDRs are proposed generate curvature in a space-filling model exterior to the outer leaflet of the bending membrane. In a contrasting example, consistent with the previous model, self-associating IDRs have been shown to generate inward curvature towards the protein-coated surface (Yuan et al., 2021).

Membrane curvature sensing in macroautophagy
Membrane shape is dynamic during autophagosome biogenesis, and the shaping of the autophagosome is central to the biological function of autophagy: the sequestration of inclusions away from the cytoplasm. The diversity of membrane curvature observed across systems and techniques highlights membrane shape dynamics as a core feature of autophagosome biogenesis (Nguyen et al., 2017). Within the core autophagy proteins, several have been shown to sense membrane curvature. The Class III PI3K complexes preferentially associate with small vesicles (Brier et al., 2019; Fan et al., 2011). ATG3 contains an amphipathic helix which likewise directs its recruitment to small vesicles (Nath et al., 2014). Another component of the LC3 lipidation machinery, ATG16L1, also associates with highly curved membranes but not with flat membranes in the absence of other factors (Lystad et al., 2019). Finally, the lipid transfer protein ATG2A also associates with highly curved vesicles (Chowdhury et al., 2018).
As membrane curvature sensors are so common among core autophagy proteins, it is interesting to speculate about their role in autophagosome biogenesis and how they may act in response to, or in regulating membrane shape in autophagy. To develop a more quantitative understanding of how core autophagy proteins regulate or are regulated by membrane curvature, I took a bottom-up approach, reconstituting curvature sensors on synthetic membrane substrates *in vitro*, using biophysical methods to characterize their behavior on curved membranes.
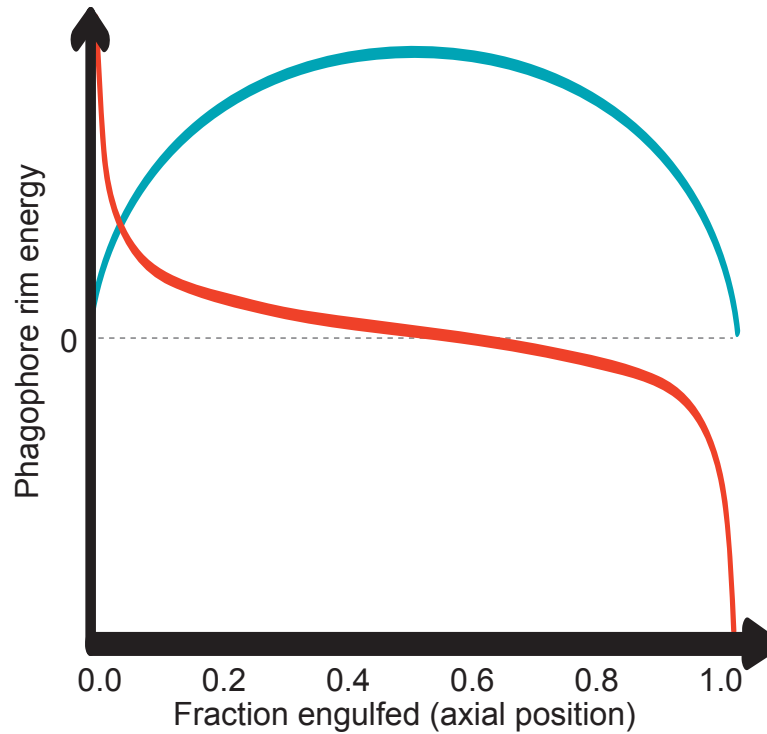
Figure 1.4. Schematic of how phagophore rim energy changes as a function of spherical cargo engulfment progression

Membrane bending energy of the phagophore rim (blue) is directly proportional to the circumference of the phagophore rim. First derivative of the change in rim energy with respect to fraction of cargo engulfed shown in orange. Membrane bending energy at the phagophore rim should increase as cargo is engulfed, reaching a maximum when 50 percent of a spherical cargo is engulfed. The amount of additional energy input required to expand the phagophore rim as a function of the fraction of cargo engulfed decreases throughout cargo engulfment, becoming negative after 50 percent of cargo is engulfed.

Chapter 2: *In vitro* reconstitution methods for studying protein-membrane interactions and membrane curvature

Introduction

To understand what role membrane curvature plays in autophagosome biogenesis, it is necessary to come up with an appropriate *in vitro* reconstituted system which contains few confounding elements. Several assays have already been developed to investigate how and to what degree proteins associate with membranes. Among these, there are a few tradeoffs in terms of physiological relevance, biophysical precision, and ease of experimental setup and throughput. Outlined below is an overview of these methods and their practical use in investigating membrane curvature sensing/inducing proteins, together with the expansions that I made to them during my thesis research.

Giant unilamellar vesicles

Giant unilamellar vesicles (GUVs) are a simple tool for evaluating protein association with flat membranes. Using fluorescently labeled proteins and membranes, protein recruitment to the surface of GUVs can be assessed by fluorescence microscopy. This method is sensitive, since it directly measures protein recruitment to membrane surfaces at concentration thresholds that are below the detection limit for bulk methods like SUV pelleting, discussed below. Preparation of GUVs is straightforward: a lipid suspension in organic solvent like chloroform is dried on a support of polyvinyl alcohol (PVA), and then rehydrated in a sucrose solution for 30 minutes. This produces a mix of vesicles that are 5-50μm in diameter, which when diluted in iso-osmotic imaging buffer will settle to the bottom of an imaging chamber due to the high density of sucrose. Notably, while the curvature of GUVs is variable on the micron scale, for physiological mechanisms involving radii of curvature on the scale of 10s of nanometers, the curvature of GUVs is essentially flat and invariant.

GUV protein recruitment assays are similar in many ways to supported lipid bilayer (SLB) recruitment experiments, as both membrane substrates provide a flat membrane platform on which the kinetics of protein recruitment to their surface can be visualized. and are more challenging to analyze. Nevertheless, GUVs are often a better substrate for investigating protein association to membranes because they can be manipulated to form regions of varying curvature (see below), and because they use significantly less lipid material to form. While SLBs require suspensions of milligrams of lipids, GUVs can be efficiently formed with several μg of lipids.

Small unilamellar vesicles

Small unilamellar vesicles (SUVs) are membrane vesicles with a diameter from 10's-100's of nanometers which can be incubated with purified proteins or cell lysates to evaluate the interaction of a protein with a membrane surface. SUVs can be generated from a variety of lipid sources (e.g. synthetic lipids, tissue homogenate, or cellular membrane fractions) dissolved in an organic solvent, dried into a film under a stream of nitrogen, and then rehydrated in aqueous buffer. At this point, the rehydrated lipids are a heterogeneous mix of multilamellar liposomes of different sizes. To refine this mix, the lipid suspension is subjected to either sonication, which yields vesicles smaller than 100nm in diameter, or extrusion through filters of varying pore size, yielding vesicles from 100-40nm diameter. Biophysical characterization of these preparations by light scattering has confirmed their approximate dimensions. Protein association with SUVs can

be assessed by co-incubation of proteins and SUVs, followed by ultracentrifugation to pellet the membrane fraction and analysis by SDS-PAGE.

Such SUV binding experiments provide a straightforward experimental framework to test the relative affinity of proteins to membrane surfaces and their response to varying membrane curvature or composition. This approach has several noteworthy limitations, however. First, SUVs formed by sonication or extrusion are still heterogeneous across a range of diameters; phosphatidylcholine liposomes extruded through 100nm filters were observed by electron microscopy to have diameters of 69.3 ± 38.7nm (MacDonald et al., 1991). Additionally, comparison of protein recruitment to SUVs of varying sizes should be done in the presence of constant lipid concentration. Because liposome extrusion through membranes of varying sizes depletes the total lipid amount in solution, it is important to use a membrane dye to track the total yield of SUVs after extrusion.

Finally, SUVs are well-suited for studying membrane remodeling events associated with spherical curvature, but many physiological events occur on cylindrical or saddle-shaped membranes, or membranes with varying curvature. SUV binding assays compare the affinity of proteins to curved membranes relative to the protein's propensity to stay in solution. They do not directly compare the affinity of proteins for regions of varying curvature on a continuous membrane surface. While this complication does not pose much of an issue in interpretation of simple systems with a single protein component, it is an important point as the complexity of the system increases. For instance, in cases where multiple interacting proteins with varying membrane affinity and curvature sensitivity are recruited to a membrane surface, it is difficult to disentangle their respective roles with SUV assays alone. Therefore, interpretation of SUV assays in these cases should be carefully considered.

Membrane Tubes Pulled from GUVs by Optical Trap

To more accurately reflect the membrane morphologies that proteins encounter during autophagosome biogenesis, more physiological membrane substrates can be generated from GUVs

A

Membrane tube
(~20-100nm radius)

GUV (~flat)

Streptavidin
bead

Optical trap

B

Fluorescent protein localization

Curvature
sensitive

Curvature
insensitive
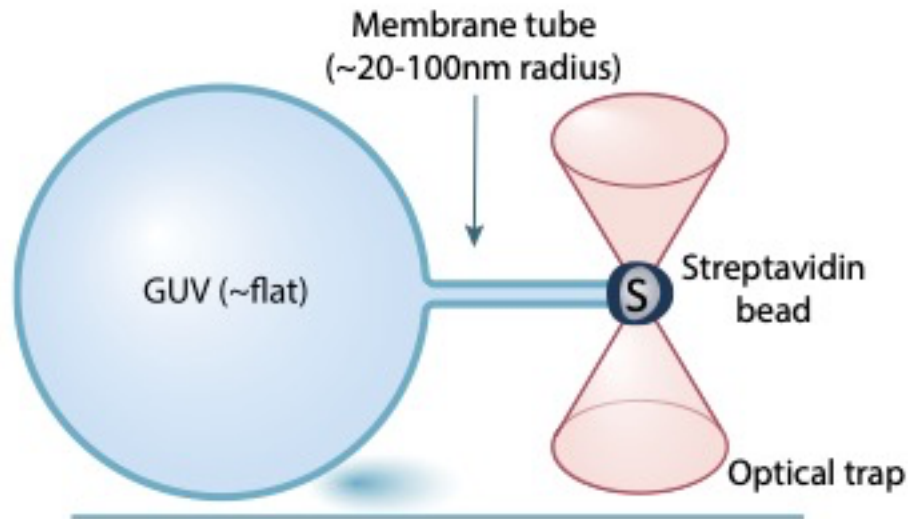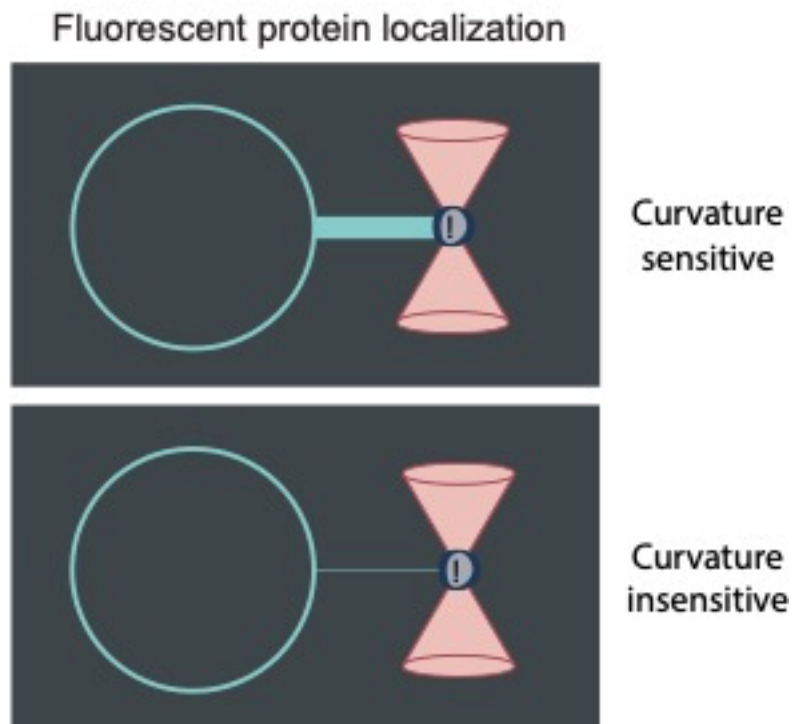
with an optical trap[1] (

---

[1] Optical traps use long wavelength lasers to control the localization of spherical objects due to their differential refractive index from the surrounding medium. When an external force is applied to the bead, it is displaced from the center of the trap, and for small displacements from the trap center, it experiences a Hookean

Figure 2.1). Optically trapped beads have been used to pull tubular membrane tethers from cellular membranes to characterize their mechanical properties (Dai & Sheetz, 1995). Subsequently, this technique was expanded to investigate the characteristics of synthetic lipid membranes of controlled composition *in vitro* (Heinrich & Waugh, 1996). Additionally, aspiration of vesicles onto micropipettes can be used to control the membrane tension of the vesicles, and has been applied to optical trapping experiments to solve for the membrane bending rigidity (Cuvelier et al., 2005; Evans & Needham, 1987; Prevost et al., 2017). Further, visualization of membrane tethers by confocal fluorescence microscopy has been utilized to quantify the behavior of membrane curvature sensing and inducing proteins (Heinrich et al., 2010; Roux et al., 2005; Sorre et al., 2009). The membrane remodeling and scission activity of membrane tube associating proteins has also been extensively characterized by this method (Renard et al., 2015; Schoneberg et al., 2018). The combined technological advances in optically trapped membrane tubes and their visualization enable robust biophysical quantification of membrane remodeling *in vitro*.

While such an experiment requires specialized equipment combining confocal fluorescence microscopy and an optical trap, it has the benefit of enabling direct visualization of membrane curvature sensing of proteins in a quantitative and physiologically relevant manner. In this setup, a streptavidin coated silica bead is caught in an optical trap and brought into contact with an immobilized GUV containing a minor fraction of biotinylated lipids and then retracted to form a membrane tube. Importantly, this creates a continuous membrane surface with adjoining regions of high (membrane tube) and low (GUV surface) membrane curvature, which is analogous to the membrane curvature of a nascent phagophore (i.e. the highly curved phagophore rim has cylindrical curvature and is immediately adjacent to the low curvature inner and outer phagophore membranes).

Membrane tubes pulled from GUVs with an optical trap also enable robust quantification of the membrane tube radius and the membrane curvature sensitivity of fluorescently labeled proteins. In canonical membrane tube experiments, GUVs are first aspirated onto a glass micropipette by applying a defined suction pressure with a microfluidic controller. GUV aspiration coupled with optical trap force measurements enables precise quantification of the membrane tension of the GUV, which determines the radius of the membrane tube. Critically, this means that tube radii can be precisely measured even when they fall below the diffraction limit for optical microscopy. The precision of membrane curvature of this technique exceeds that of SUV extrusion, enabling the differentiation of subtle variations in membrane curvature sensing on the order of several nanometers. This is particularly important at autophagy-relevant curvatures of low 10s of nanometers.

Another advantage of using optically trapped membrane tubes to study membrane curvature is that it is possible to compare localization of labeled proteins to curved versus flat membranes on a continuous membrane surface. The ratio of protein surface density on the

---

force pulling it back towards the trap center. Because the force experienced by the bead is linearly correlated with displacement from the trap center, force applied to the bead can be calculated by measuring the displacement of the bead from the trap center with a quadrant photodiode (QPD), which measures the localization of scattered light by the trapped bead. Optical traps vary in their trap stiffness, i.e. the force required to pull the bead out of the trap completely.

membrane tube compared to the GUV surface enables thermodynamic evaluation of the system which is inaccessible with other methods for studying membrane curvature-dependent protein recruitment. The important property of the optically trapped membrane tube experiment that enables quantitative biophysical measurement is that the membrane tube and GUV surface are part of the same system, so variations to, for instance, lipid composition from GUV to GUV are controlled for.

Analysis and quantification of curvature sensitivity of proteins in this system is also straightforward. Incubation of the GUV/membrane tube system with fluorescently labeled proteins enables direct visualization of protein partitioning onto the tube or GUV surface by confocal fluorescence microscopy. Enrichment of a curvature sensitive protein on the membrane tube can be quantified by taking the ratio of fluorescence intensities of the protein on the tube and the protein on the GUV, normalizing for membrane surface area. Curvature sensitive proteins will have a higher surface density on the membrane tube relative to their density on the GUV surface, while curvature insensitive proteins have the same surface density on the membrane tube as on the GUV surface (Figure 2.1).

In principle, a curvature sensitive protein will become increasingly enriched on the membrane tube as its curvature approaches the preferred curvature of the protein. This follows from the predicted Gaussian dependence of enrichment on curvature, with maximum enrichment at the spontaneous curvature of the protein (Simunovic et al., 2016). In practice however, there are few proteins that exhibit spontaneous curvature in the range of experimentally accessible membrane tube radii. Therefore, it is often most informative to analyze curvature sensitivity as a
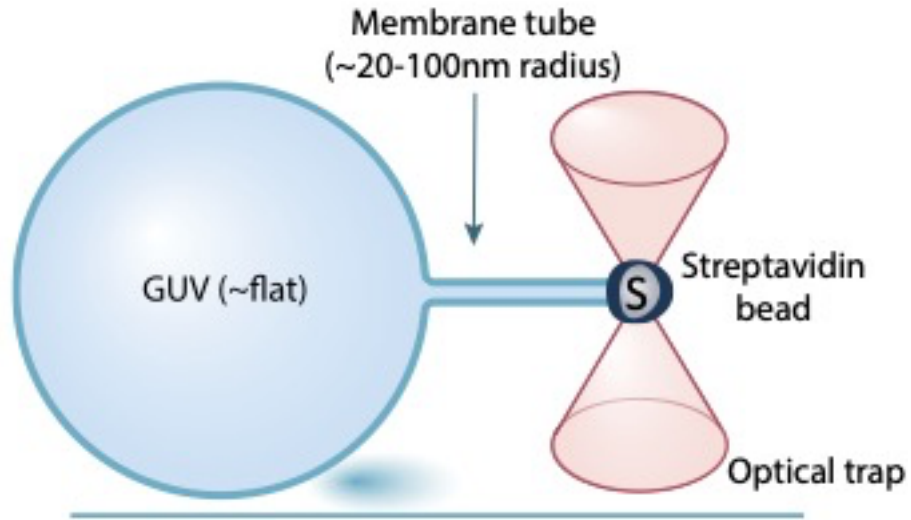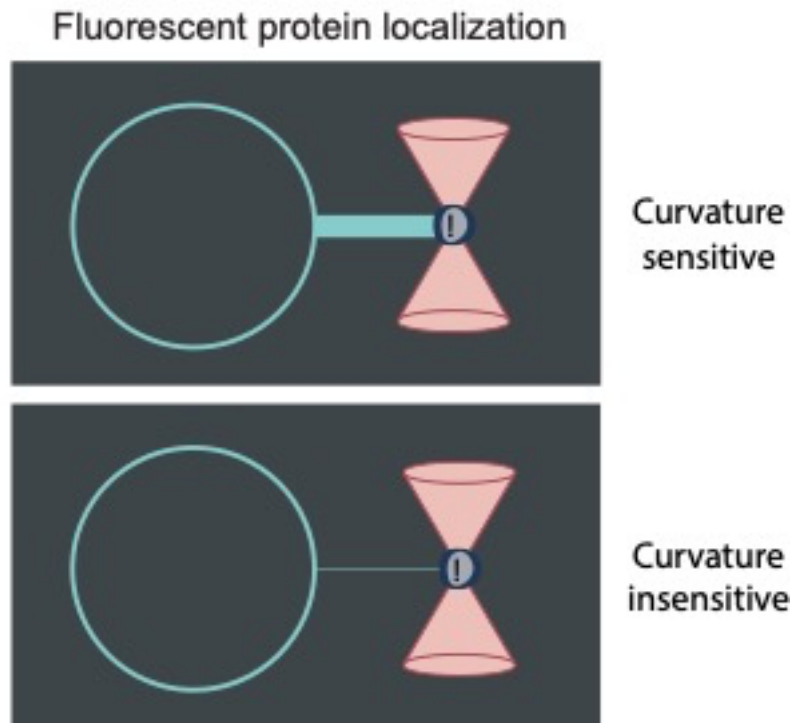
Figure 2.1 Membrane tube pulled from a GUV with an optical trap
(**A**)An immobilized giant unilamellar vesicle (left), with a minor fraction of biotinylated lipids, is brought into proximity with a streptavidin coated bead held in an optical trap. Upon retracting the optical trap, a narrow tube is formed between the GUV and the bead. In this setup, the GUV has a radius of 10s of μm, and is therefore nearly flat at the molecular scale. The 'flat' membrane of the GUV is contiguous with the highly curved membrane tube. (**B**) Differential localization of fluorescently labeled protein on the basis of curvature sensitivity. Curvature sensitive proteins are enriched on the tube compared to the GUV (top).

function of the slope of protein sorting (S) versus curvature (C), where more curvature sensitive proteins have a higher slope, and less curvature sensitive proteins have a lower slope.

Simplified Flow Cell Construction and Experimental Setup for Membrane Tubes Formed by an Optical Trap

To expedite data acquisition and minimize sample loss in optical trapping experiments, I developed a simplified experimental workflow and imaging chamber design. Constructing an imaging chamber for canonical aspirated GUV membrane tube experiments requires fashioning aspiration pipettes from glass filament, installing these pipettes onto micromanipulators attached to a microfluidic controller, building an open-sided imaging chamber, and finding and manipulating GUVs and beads within the imaging chamber. Together, these steps yield a procedure so prone to failure that it takes weeks or months of effort to collect even small data sets of membrane tube experiments. Therefore, to collect datasets large enough to address physiological questions about membrane shape, it is necessary to simplify the instrumentation. Here, I will describe the challenges presented by the standard instrumentation for optically trapped membrane tube experiments, and then detail the improvements I made to the setup to enable more efficient data collection.

Aspiration pipettes are typically used to control the membrane tension of a GUV during a membrane tube experiment, yet they are difficult and time-consuming to create and to wield. Pipettes are pulled by an automated program on a pipette-puller but must subsequently be molded by hand with a microforge. Pipettes must then be backfilled with imaging buffer, and their small inner diameter makes it difficult to remove air bubbles, which interfere with precise aspiration control by the microfluidic controller. Pipettes often break due to rough handling while removing air bubbles. The pipettes are then loaded onto pipette holders connected to the microfluidic controller. These pipette holders have small pieces that are easily fumbled and must be carefully wielded to prevent introduction of new air bubbles or pipette breakage. Finally, adjusting the buffer flow through the pipette with the microfluidic controller requires fine control of the pressure requested through the controller, for which the control software is not optimized, and equilibrating the pressure at the aspiration pipette outlet is prone to under- and overshooting. Additionally, pulling tubes from aspirated GUVs is difficult. Aspirating GUVs onto a pipette increases their membrane tension to a point where large forces are required to pull membrane tubes, and frequently beads will get pulled out of the trap by the GUV instead of pulling a membrane tube from the GUV. Membrane tension of GUVs can be lowered by creating an osmolarity offset in the imaging buffer compared to the GUV interior, but stable aspiration of GUVs results in relatively high membrane tension regardless of the osmotic offset, leading to persistent problems with pulling tubes.

Introducing the aspiration pipette into the imaging chamber is also fraught. To accommodate the pipette, the imaging chamber is constructed from two opposed glass coverslips with a spacing of 2mm. Such an open-sided imaging chamber has an approximate volume of 1 ml and is subject to flow currents generated by evaporation at the open edges. This buffer flow can impact retention of a GUV at an aspiration pipette and impact force measurements by the optical trap. It is time intensive and incompletely effective to limit these currents by sealing the edges of the imaging chamber with mineral oil. The large size of the imaging chamber also requires large amounts of purified protein to test protein association with membrane tubes. The

workaround of injecting protein onto membrane tubes with a second pipette is also time intensive, error-prone, and still requires a large volume of protein to backfill the injection pipette. Together, these complications almost entirely confound the real work of collecting data from membrane tube experiments.

Because the aspiration pipette is a particularly error-prone component of the instrument setup for optically trapped membrane tubes, I posited that developing a method for generating membrane tubes that eschewed the pipette would enable higher throughput experimentation amenable to collection of informative datasets in a reasonable time. Therefore, I worked to develop a method for generating membrane tubes that retained as much quantitative information as possible without the aspiration pipette.

Removing the aspiration pipette from the setup first necessitated another method for immobilizing GUVs to pull membrane tubes from them. I initially tested whether functionalizing the surface of the coverglass could be used to immobilize GUVs on the surface. I incubated imaging chambers with a solution of 0.1mg/ml streptavidin for 10 minutes, followed by passivation with 1mg/ml BSA (bovine serum albumin) before rinsing the chamber with imaging buffer and adding in GUVs. I found that, while streptavidin functionalization of the coverglass indeed immobilized the biotinylated GUVs, it was now much more difficult to generate attachments between the GUV and the streptavidin coated bead needed to form membrane tubes. This was likely due to desorbed streptavidin from the coverglass competing with the streptavidin beads for biotin groups on the GUV surface.

I next tested whether decreasing the degree of coverglass passivation could generate a sparsely adhesive surface which would immobilize GUVs while maintaining sufficient passivation to keep the GUVs from bursting upon contact with the coverglass. Typically, imaging chambers are incubated with 1mg/ml BSA for 10 minutes to passivate the surface to prevent GUVs from bursting upon contact with the coverglass. I reasoned that a shorter incubation with BSA would yield incomplete passivation, causing the GUVs to associate with the coverglass, but maintaining their integrity. Indeed, a 30 second incubation with 1mg/ml BSA was sufficient to prevent GUVs from bursting as they settled on the coverglass surface, and to immobilize them so that membrane tubes could be pulled from them with the optical trap.

Immobilizing GUVs on the coverglass surface has the advantage that an aspiration pipette is not required, but without an aspiration pipette, the experiment no longer contains information about the GUV membrane tension. Nevertheless, tube radius can still be calculated by measuring fluorescence intensity and comparing to fluorescence intensity measurements in aspirated GUV experiments where membrane tension is known.

Without an aspiration pipette, the imaging chambers could also be modified to decrease their volume, thereby decreasing the amount of reagents needed to perform experiments and enabling rapid troubleshooting experiments with simple flow cells. I constructed flow cells from 2 layers of coverglass sandwiching a layer of parafilm, all melted together with a hot plate. Parafilm was used to form the edges of the flow cell instead of commonly used double-sided tape because of geometric constraints of the particular microscope stage used, although double-sided tape would have been simpler and faster. The new flow cells decreased the volume of each
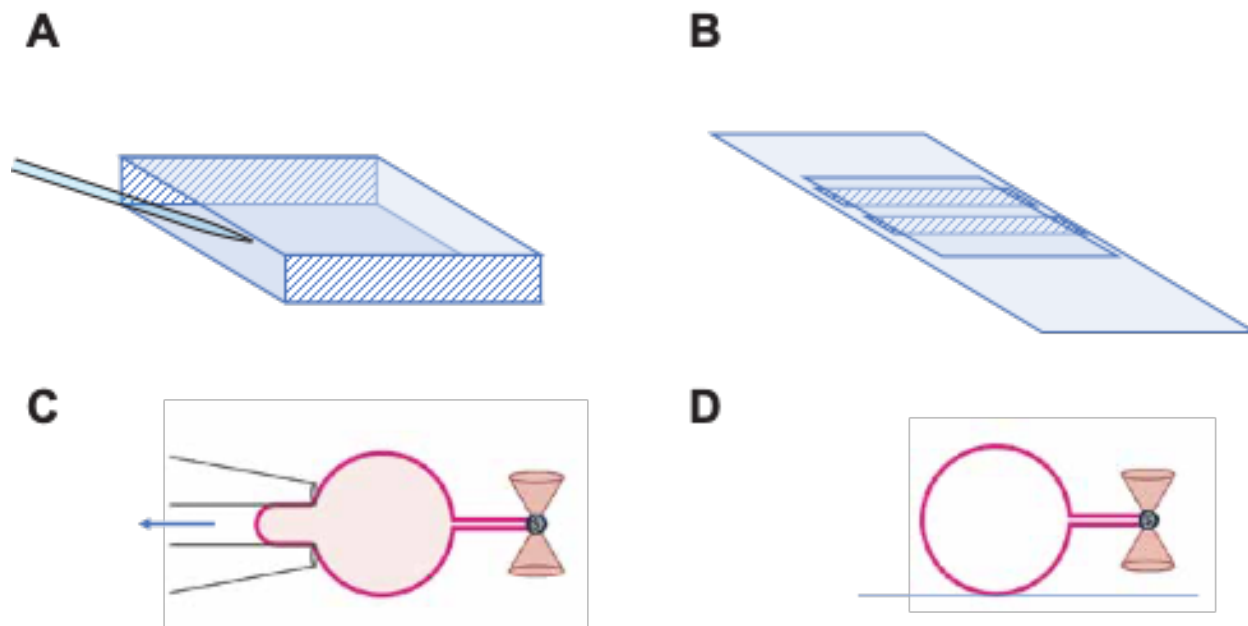
Figure 2.2 Imaging chambers for optically trapped membrane tubes
(**A**) Open-sided microscope chamber for pulling membrane tubes from GUVs immobilized on an aspiration pipette, as in (**C**). Two pieces of coverglass are positioned with a 2mm space to allow for introduction of the aspiration pipette. (**C**) Schematic of pulling a membrane tube from a GUV immobilized on an aspiration pipette. Control of the aspiration pressure enables quantitation of the membrane tension and thereby membrane tube radius from a readout of the force of the membrane tube pulling on the bead held in the optical trap. (**B**) Simplified small volume microscope chamber constructed from 2 layers of coverglass sandwiching two strips of melted parafilm, which form the sides of the flow cell. (**D**) Schematic of simplified setup for pulling membrane tubes with an optical trap, using flow cells as in (**B**), where GUVs are immobilized by sparse tethering to the flow cell surface.

experiment to less than 10ul and could be easily sealed at the edges to unwanted evaporation. Importantly for rapidly troubleshooting experimental conditions, many of these flow cells can be constructed in advance of a microscopy session, minimizing downtime in between individual membrane tubes pulled.

Flow-induced membrane tubes

Even with the above simplifications, optically trapped membrane tubes are still a low throughput method, with a maximum rate of data collection of only a few tubes per day. Collection of more replicates in parallel could enable more robust quantitation of membrane curvature sensing and the analysis of the kinetics of membrane remodeling. Additionally, optically trapped membrane tubes are not suitable for visualization at higher resolution, for instance by electron microscopy (EM). This led me to pursue a method to generate highly curved membrane tubes as substrates for *in vitro* reconstitution of membrane remodeling that did not require an optical trap.

Pucadyil and colleagues have developed a method for generating membrane tubes in microfluidic flow cells using buffer flow across a supported lipid bilayer (Dar et al., 2015, 2017). These flow-induced membrane tubes enable visualization of membrane association of fluorescently labeled proteins by confocal microscopy and kinetic evaluation of membrane remodeling events. In this approach, a solution of lipids in organic solvent are dried into a film on a passivated glass imaging coverslip, and then a microfluidic flow cell is constructed around the lipid film. Aqueous buffer is injected into the flow cell to first hydrate the lipid film and then to induce the formation of membrane tubes. At low flow rates (~50µl/minute), the flow of buffer across the supported lipid bilayer induces the extension of membrane tubes across the flow cell over the course of several minutes. Under continued flow, these membrane tubes become sparsely tethered to the coverglass surface at points of incomplete passivation. When flow is turned off, these tethering points anchor the membrane tubes, preventing them from retracting towards the inlet.

This method has the advantage of enabling the visualization of ~10 membrane tubes in parallel, but it is also less information-rich than membrane tubes pulled from GUVs. For membrane tubes pulled from GUVs, the highly curved membrane tube is directly contiguous with the comparatively flat GUV surface. This enables a quantitative analysis of protein partitioning on a membrane substrate with directly juxtaposed regions of high and low curvature. In contrast, flow induced membrane tubes only provide information about protein residence on a single curved membrane; there is no flat membrane sink for comparison. Thus, it is a technique suited to *in vitro* reconstitution of physiological membrane remodeling events that do not directly involve highly variable membrane curvature, like autophagy. Flow-induced tubes are well-suited to the study of proteins that form coats on tubular membranes and membrane scission machinery.

Using this approach as guide, I developed a similar setup to generate membrane tubes on an existing confocal fluorescence microscope with an inverted stage. I designed and built flow cells that could be connected to a syringe pump that could maintain flow rates in the range of 20-50µl. Briefly, I used a diamond drill bit to drill an inlet and outlet into a glass slide. Fluidic ports were glued over these outlets in the glass slide with a hot glue gun. A lipid film was dried

21

A
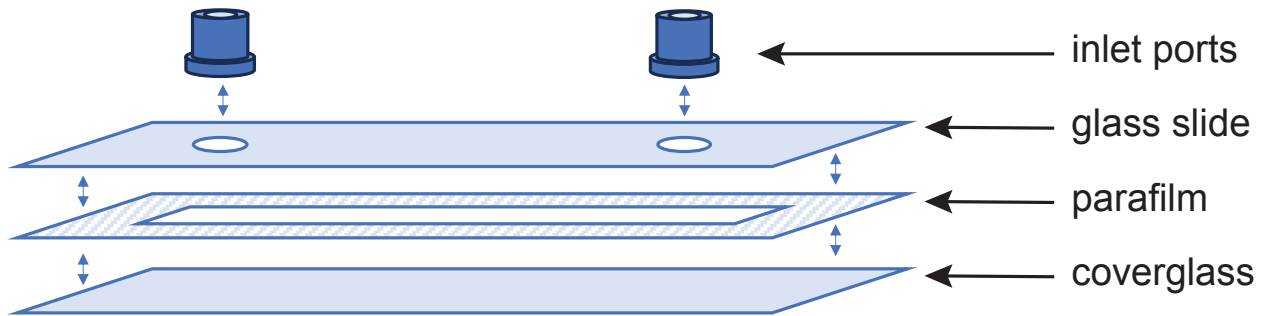
B
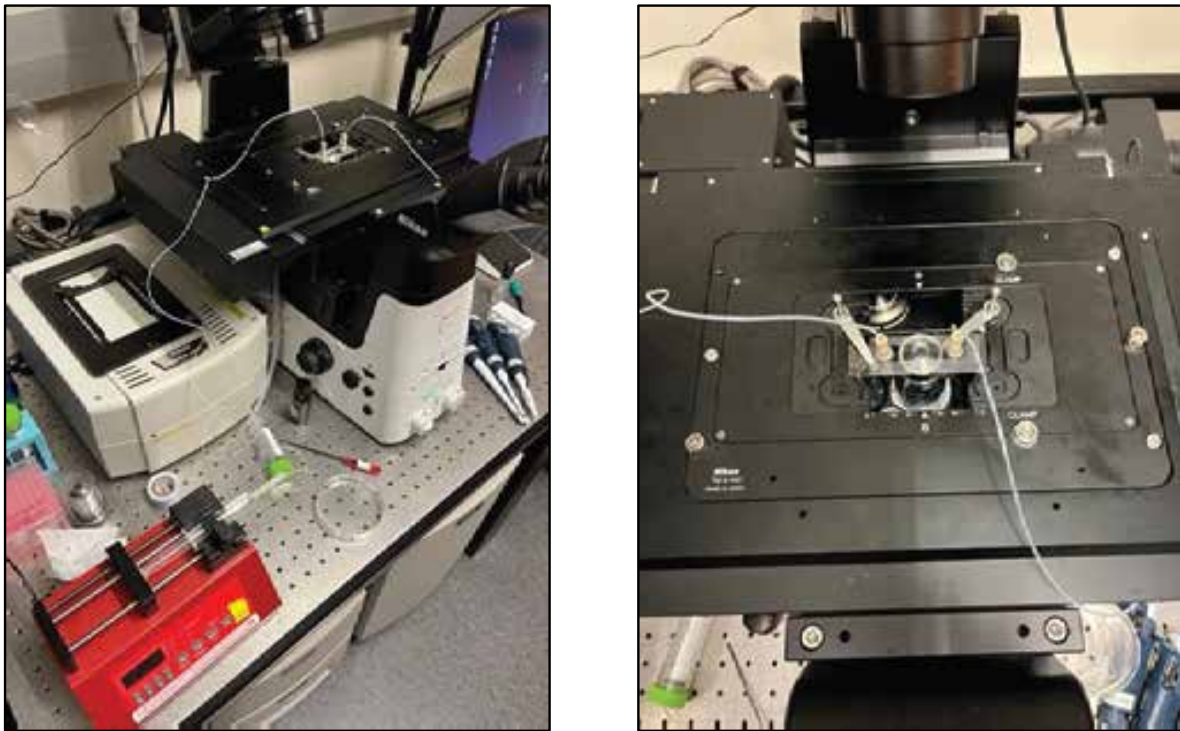
Figure 2.3 Membrane tube flow cell assembly
(**A**) Flow cells for generating and visualizing membrane tubes constructed from a layer of parafilm sandwiched between a layer of coverglass and a glass slide with drilled inlet and outlet. Ports are glued to the inlet and outlet to connect the flow cell to tubing the membrane syringe pump. (**B**) Flow cell setup on an inverted confocal microscope.

onto a coverslip, then the coverslip and slide were constructed into a flow cell by sandwiching a layer of melted parafilm between them. Tubing was connected between a luer syringe port and the flow cell inlet. Valves were inserted into the tubing so that buffer flow could be stopped completely during experiments. I used this setup to evaluate the membrane tube association of AP proteins.

In addition to visualizing protein association to tubular membranes by optical microscopy, I was curious about the basis of protein/ tube association at molecular resolution, accessible by electron microscopy. To do this, I needed a simpler way to generate membrane tubes on an electron microscopy grid that did not require a flow cell, the disassembly of which would be required for plunge freezing. I had observed that in experiments where I had pulled membrane tubes from GUVs immobilized to glass coverslips the application of buffer flow after the GUVs had adhered to the flow cell surface also generated membrane tubes in a less controlled manner. In these simple flow cells, well-controlled buffer flow rate was not required to form membrane tubes, I reasoned that a simple setup to provide buffer flow across EM grid-adhered might be sufficient to generate membrane tubes. So, I incubated GUVs on EM grids after which I pipetted buffer across them while wicking from the opposite side of the grid with a kimwipe. I found that this method formed membrane tubes on grids even in the absence of a strongly tubulating protein.

A

Buffer flow

GUV

Membrane tube

B

C

50 nm

50 nm
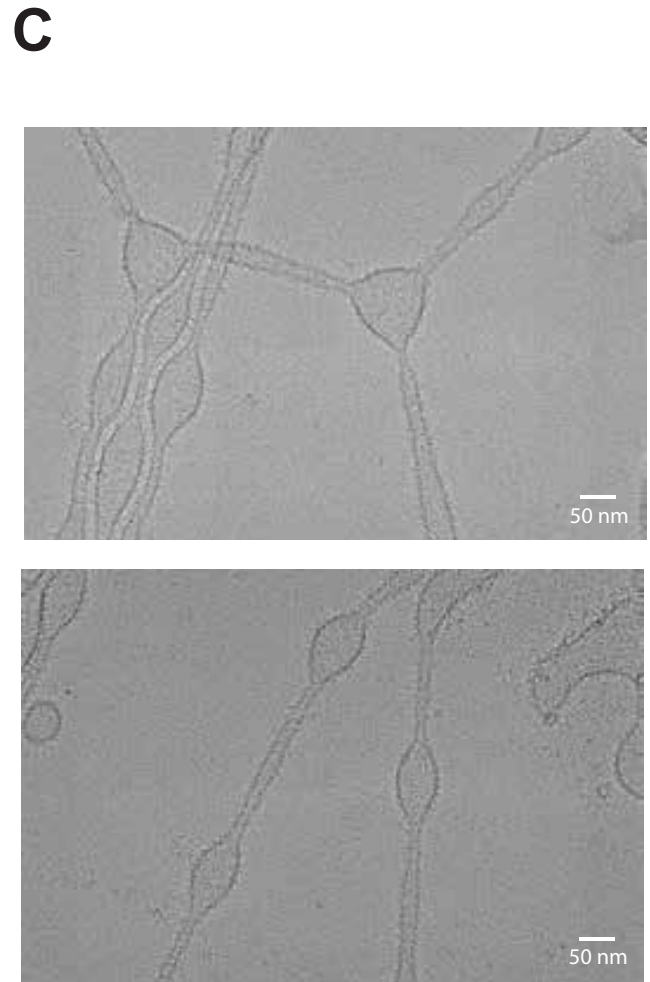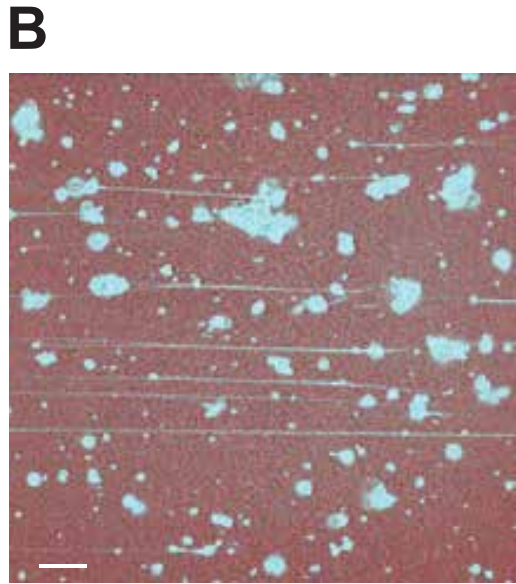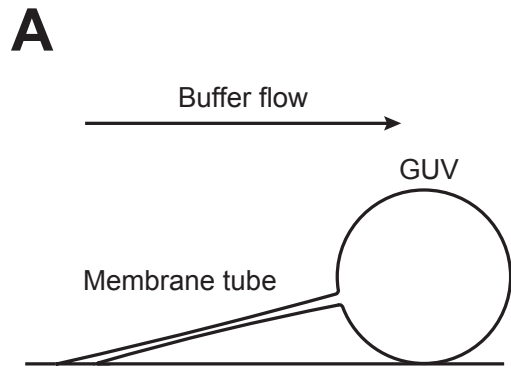
Figure 2.4 Flow tubes from surface adhered GUVs

Chapter 3: Membrane curvature sensing and stabilization by the LC3 lipidation machinery

This chapter contains work carried out in collaboration. Shanlin Rao carried out the molecular dynamics simulations. Sections of this chapter were previously published as:

Jensen, L. E., Rao, S., Schuschnig, M., Cada, A. K., Martens, S., Hummer, G., & Hurley, J. H. (2022). Membrane curvature sensing and stabilization by the autophagic LC3 lipidation machinery. *Science advances*, *8*(50), eadd1436. https://doi.org/10.1126/sciadv.add1436

Introduction

   The formation and stabilization of the cup-shaped membrane during phagophore expansion is associated with energetic penalties and barriers (Bahrami et al., 2017; Knorr et al., 2012; Sakai et al., 2020). Recent cryo-ET visualization of phagophores in yeast revealed that the membrane curvature at the phagophore rim approaches the maximum value possible given the thickness of the phospholipid bilayer (Bieber et al., 2022). The recruitment of membrane curvature inducing proteins to the phagophore rim is currently a leading model to explain how its high curvature is stabilized (Sakai et al., 2020). A number of core autophagy proteins have been shown to sense membrane curvature (Nguyen et al., 2017). The PI3KC3-C1 subunit ATG14 senses membrane curvature through its C-terminal BATS domain (Brier et al., 2019; Fan et al., 2011; Ohashi et al., 2020). Both the human phospholipid transporter ATG2A(Sakai et al., 2020) and the *Arabidopsis* ATG5 subunit of the ATG12–ATG5-ATG16L1 complex (Le Bars et al., 2014) localize to toroidal structures that appear to correspond to the phagophore rim. ATG3 (Nath et al., 2014) and the ATG12–ATG5-ATG16L1 complex (Lystad et al., 2019), which are both involved in the conjugation of ATG8 proteins to membranes, preferentially bind to small liposomes through amphipathic helices at or near their N-termini. Thus, both cell imaging (Le Bars et al., 2014) and *in vitro* binding (Lystad et al., 2019) data suggested that the ATG12–ATG5-ATG16L1 complex could stabilize the phagophore rim via a preference for high curvature membrane binding.

   Covalent conjugation of the ATG8 family proteins LC3A-C, GABARAP, and GABARAPL1/2 to the membrane lipid phosphatidylethanolamine (PE), hereafter referred to as "LC3 lipidation", contributes to phagophore expansion (Nguyen et al., 2016) and the recruitment of cargo and other autophagy proteins (Birgisdottir et al., 2019; Rogov et al., 2014). LC3 lipidation proceeds through a cascade of enzymes analogous to the ubiquitin E1/E2/E3 ligase mechanism (Figure 3.1A). The E1 ATG7 binds LC3, handing it off to the E2 ATG3, which works together with the E3 ATG12–ATG5-ATG16L1 to covalently conjugate LC3 to PE headgroups on the phagophore. The ATG12–ATG5-ATG16L1 is recruited to PI(3)P-positive autophagic membranes by the PROPPIN WIPI2 through its binding to a WIPI2 interacting region in ATG16L1 (Dooley et al., 2014; Strong et al., 2021). These reactions have been reconstituted *in vitro* on sonicated liposomes (Ichimura et al., 2004; Nath et al., 2014) and flat membranes (Fracchiolla et al., 2020). In this study, we sought to systematically examine the impact of curvature on this machinery using a precisely tunable and quantitative *in vitro* system, and to gain a detailed molecular view of the membrane interactions with the help of molecular dynamics simulations.

   Optical tweezers can be used pull membrane nanotubes from a giant unilamellar vesicle (GUV) and form a contiguous membrane system with regions of high and low curvature,
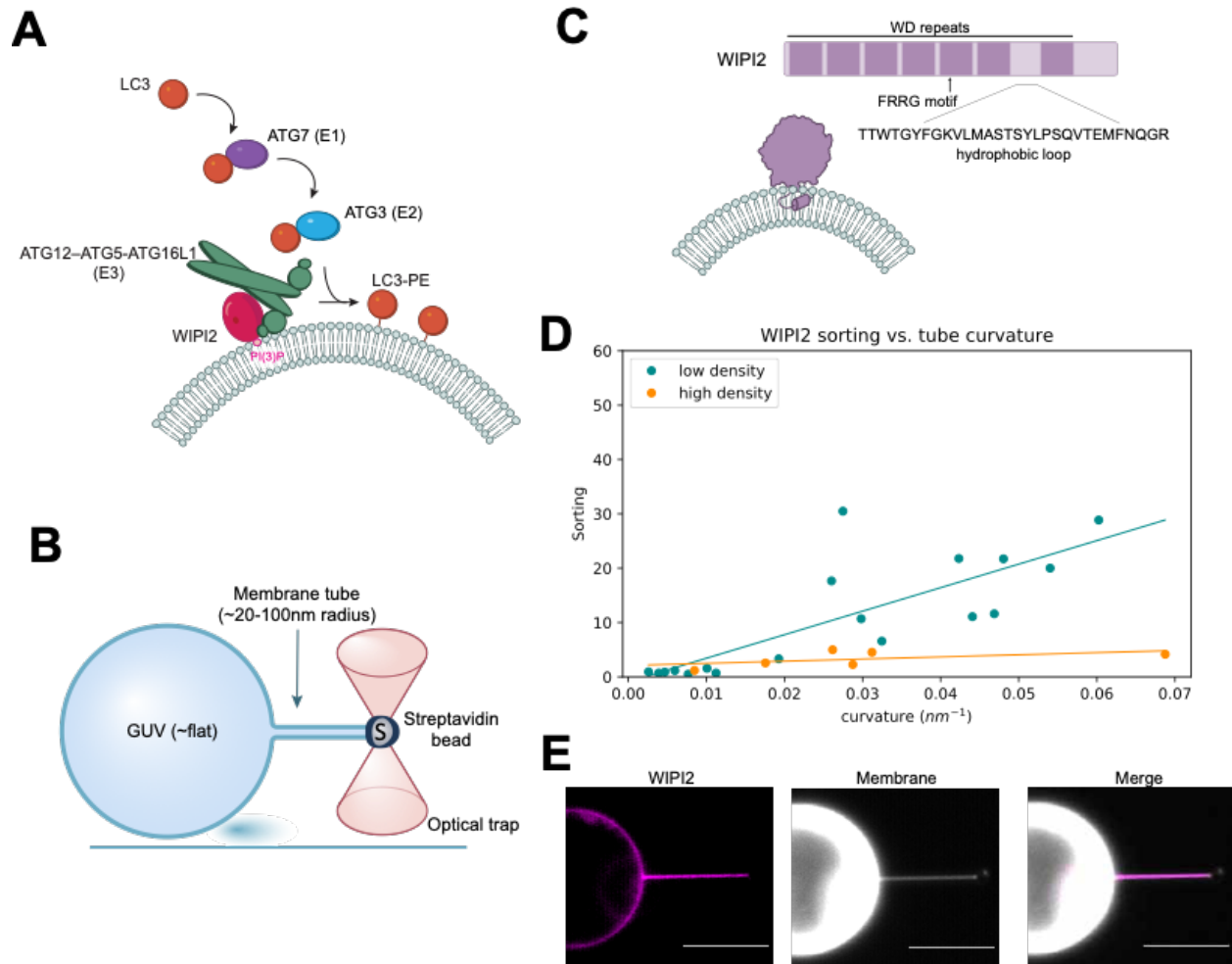
Figure 3.1 WIPI2 senses membrane curvature.
(A) Overview of LC3 lipidation machinery at a phospholipid bilayer. (B) Schematic of GUV/optical trap setup for quantification of membrane curvature sensing. (C) Graphical representation of WIPI2 domain architecture and interaction with curved membrane. (D) Plot of WIPI2 sorting versus membrane tube curvature at high (n = 6, r2 = 0.30) and low (n = 18, r2 = 0.64) surface densities of WIPI2 on the GUV surface. Each data point represents an individual membrane tube. (E) Representative confocal fluorescence microscopy images of WIPI2 localization on membrane tube and GUV surface. Scale bars, 10 μm.

enabling quantitation of the curvature sensitivity of proteins (Prevost et al., 2015; Sorre et al., 2009) (Figure 3.1B). This experimental setup can access nanoscale dimensions similar to the curvature of the phagophore rim (<30 nm (Nguyen et al., 2017)). The physics of membrane nanotubes pulled under force from an optical trap allows their radius to be measured by fluorescence microscopy even for dimensions far below the optical diffraction limit. Here, we used this approach to characterize the WIPI2 and ATG12–ATG5-ATG16L1 system and find that it is profoundly curvature sensitive.

WIPI2 senses positive membrane curvature

WIPI2 is responsible for the membrane recruitment of ATG12–ATG5-ATG16L1 in cells (Dooley et al., 2014; Strong et al., 2021), so we began by assessing how WIPI2 interacts with membranes of varying curvature. WIPI2 is a member of the PROPPIN family of proteins, which bind membranes through a hydrophobic loop (Baskaran et al., 2012) together with an FRRG motif which specifically recognizes PI(3)P (Baskaran et al., 2012; Dove et al., 2004; Krick et al., 2012; Watanabe et al., 2012) (Figure 3.1C). We used the membrane nanotube assay to measure the curvature sensitivity of WIPI2 by visualizing WIPI2 localization to highly curved membrane tubes and the essentially flat GUV from which they were pulled (Figure 3.1D). PI(3)P-positive GUVs were incubated with fluorescently labeled mCherry-WIPI2 and the curvature sensitivity of WIPI2 was assessed by its sorting ratio (S, the ratio of protein surface density on the tube to the protein density on the GUV surface (Sorre et al., 2009)). At the limit of low density, the sorting ratio describes the tendency of membrane bound proteins to preferentially associate with the curved tube compared to the molecularly flat GUV surface.

Analysis of WIPI2 localization showed that it preferentially binds to membrane tubes compared to the GUV surface, and more strongly sorts onto narrow tubes compared to wide tubes. The sorting dependence on curvature for WIPI2 is most apparent on GUVs with a low protein surface density (ϕ_v), reaching $S_w = 14\pm 5$ for tubes with radii between 20 nm and 40 nm (Figure 3.1D, E). As expected, the sorting ratio of WIPI2 diminishes with increasing protein surface density on the GUV, which is attributable to approaching surface area saturation on the tube (Prevost et al., 2015; Simunovic et al., 2016). A linear fit shows a monotonic increase in sorting with curvature, similar to proteins that are known to insert into lipid bilayers via amphipathic helices (Ambroggio et al., 2010).

To test whether the observed curvature-dependent sorting of WIPI2 is intrinsic to the protein itself and not due to enrichment of PI(3)P on the membrane tubes, we analyzed the localization of a fluorescently labeled PI(3)P probe, mCherry-FYVE. We found that, in contrast to WIPI2, mCherry-FYVE exhibited no enrichment on membrane tubes compared to the GUV surface (Figure 3.2A), indicating that sorting of WIPI2 is due to its inherent membrane curvature sensing activity.

ATG12–ATG5-ATG16L1 has enhanced curvature sorting

Because both WIPI2 and ATG16L1 contain membrane binding motifs, and because WIPI2 is required to recruit ATG12–ATG5-ATG16L1 to flat membranes (Fracchiolla et al., 2020), we sought to understand the relative roles of WIPI2 and ATG16L1. We pulled membrane nanotubes from GUVs incubated with mCherry-WIPI2 and ATG12–ATG5-ATG16L1-GFP and analyzed their respective recruitment to the membrane tube (Figure 3.3A, B, C). Just as for
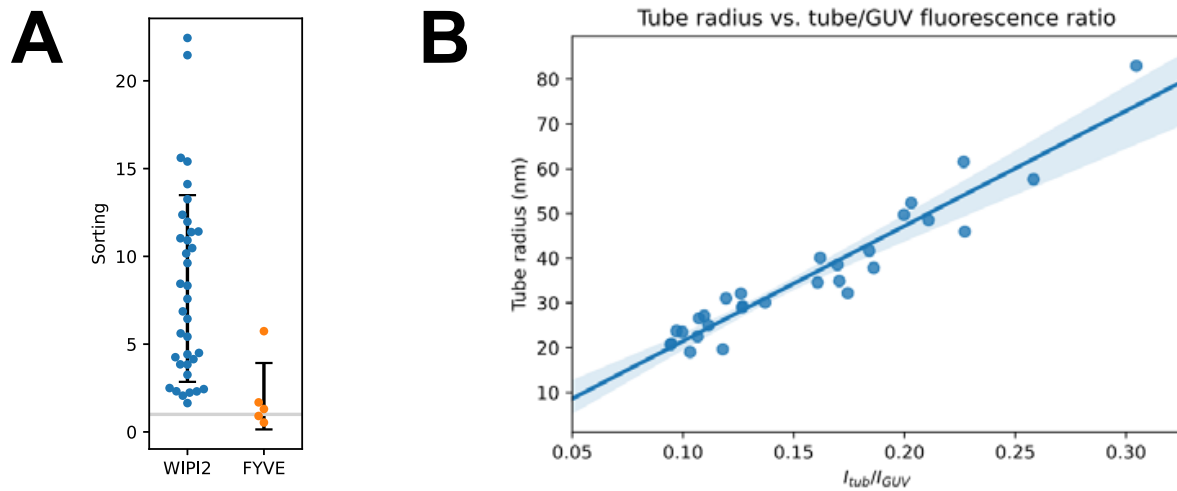
Figure 3.2 Membrane tube sorting and curvature quantification
(**A**) Swarm plot comparison of WIPI2 (blue) compared to FYVE (orange) sorting on membrane tubes. Black bars indicate standard deviation; grey horizontal line at S=1. (**B**) Tube radius calculated from optical trap force and GUV aspiration pressure vs. ratio of fluorescence intensity of membrane tube to GUV surface. Linear regression plotted as a solid blue line.
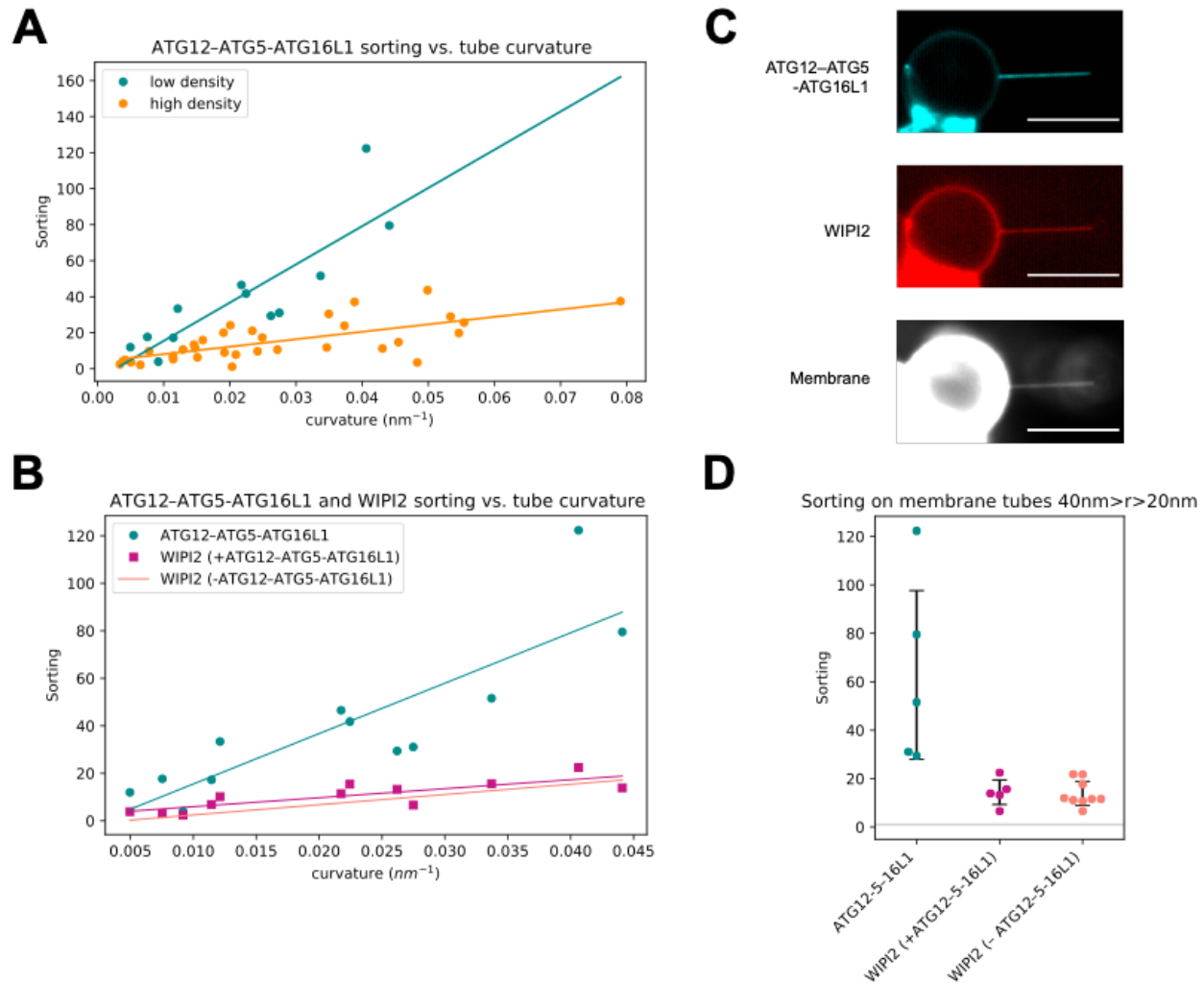
Figure 3.3 ATG12–ATG5-ATG16L1 has enhanced curvature sensitivity compared to WIPI2
(**A**) Quantification of ATG12–ATG5-ATG16L1 sorting onto membrane tubes at high (cyan, n = 12, r^2 = 0.47) and low (orange, n = 33, r^2 = 0.72) membrane surface densities of protein. Each data point represents an individual membrane tube. (**B**) Comparison of sorting dependence on curvature for ATG12–ATG5-ATG16L1 (cyan) and WIPI2 (magenta, r^2 = 0.66) with two-color fluorescence imaging compared to sorting of WIPI2 in the absence of ATG12–ATG5-ATG16L1 (salmon). Scale bars, 10 μm. (**C**) Representative image of membrane tube enrichment of ATG12–ATG5-ATG16L1 and WIPI2 from (A) and (B). (**D**) Swarmplot depicting the sorting of ATG12–ATG5-ATG16L1 and WIPI2 (n = 5), compared to WIPI2 in the absence of ATG12–ATG5-ATG16L1 (n = 9) on membrane tubes with radii between 20 and 40 nm, black bars indicate SD, and horizontal gray line at S = 1.

29

WIPI2, the sorting index S of ATG12–ATG5-ATG16L1 depends on protein surface density. Lower protein density on the GUV correlated with strong sorting of ATG12–ATG5-ATG16L1 onto membrane tubes (Figure 3.3A). ATG12–ATG5-ATG16L1 was more strongly enriched on membrane tubes than WIPI2, with a sorting ratio $S_{E3}=63\pm35$ for membrane tubes with radii between 20nm and 40nm, compared to a sorting ratio $S_W=15 \pm 4$ for WIPI2(Figure 3.3B, D).

ATG16L1 and WIPI2 curvature sensing is independent of ATG3

Having established the potent membrane curvature sensitivity of WIPI2 and ATG12–ATG5-ATG16L1, we next tested their curvature sensitivity in the presence of ATG3, the LC3 lipidation E2 enzyme. Previously identified as a membrane curvature sensor through an N-terminal amphipathic helix (Nath et al., 2014), we hypothesized that ATG3 might be able to even further increase the curvature dependent sorting of WIPI2 or ATG12–ATG5-ATG16L1 through a direct interaction.

First, we tested the interaction between ATG3 and ATG12–ATG5-ATG16L1. ATTO565 labeled ATG3 was incubated with GUVs alone or in the presence of unlabeled WIPI2 and ATG12–ATG5-ATG16L1-GFP. ATG3 was only recruited to the GUV surface in the presence of ATG12–ATG5-ATG16L1, and co-partitioned with ATG12–ATG5-ATG16L1 onto membrane tubes (Figure 3.4A). To assess the impact of ATG3 on the curvature sensitivity of ATG12–ATG5-ATG16L1 while controlling for potential differences in sorting induced by the fluorescent tags, we incubated GFP labeled ATG12–ATG5-ATG16L1 with unlabeled ATG3 and mCherry-WIPI2. We found that addition of ATG3 did not alter the partitioning of ATG12–ATG5-ATG16L1 onto membrane tubes compared to ATG12–ATG5-ATG16L1 in the presence of WIPI2 alone (Figure 3.4B). Despite the importance of its amphipathic helix for LC3 lipidation activity (Nath et al., 2014), ATG3 did not measurably augment the curvature sensitivity of WIPI2 and ATG12–ATG5-ATG16L1.

ATG16L1 helix2 drives curvature sensing

We next sought to understand the mechanism for the potent curvature sensitivity of ATG12–ATG5-ATG16L1 complex. A previous report had characterized the membrane interactions of amphipathic helix a2, located near the N-terminus of ATG16L1 (Lystad et al., 2019). On highly curved sonicated vesicles, the physiological requirement for WIPI2 membrane recruitment can be bypassed (Fracchiolla et al., 2020). Helix a2 was shown to be essential for WIPI2-independent activity of ATG12–ATG5-ATG16L1 on sonicated liposomes, and essential for LC3 lipidation and autophagic flux in both bulk and selective autophagy in cells (Lystad et al., 2019). We use the same FII mutation previously shown to block autophagy and LC3 lipidation in cells and assessed its impact on curvature sorting of ATG12–ATG5-ATG16L1.

A GFP-tagged version of the previously described FII mutant (F32A, I35A, I36A) of ATG16L1 was purified and incubated with GUVs in the presence of mCherry-WIPI2 (Figure 3.5A, B). The FII mutation was sufficient to ablate the curvature sensitivity of ATG12–5-16L, and caused a minor decrease in the sorting of WIPI2 onto membrane tubes (Figure 3.5C, D). We conclude that the molecular basis for the amplified curvature-dependent sorting we observed for ATG16L1 depends on hydrophobic residues in the amphipathic helix a2 of ATG16L1.
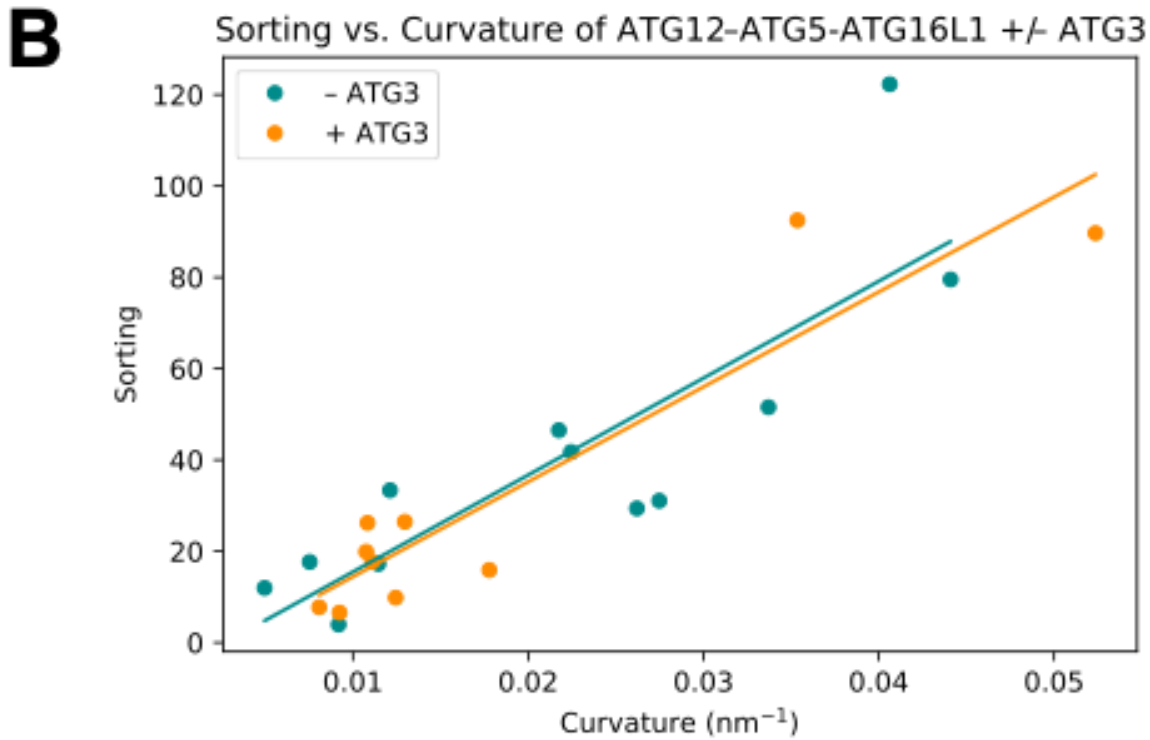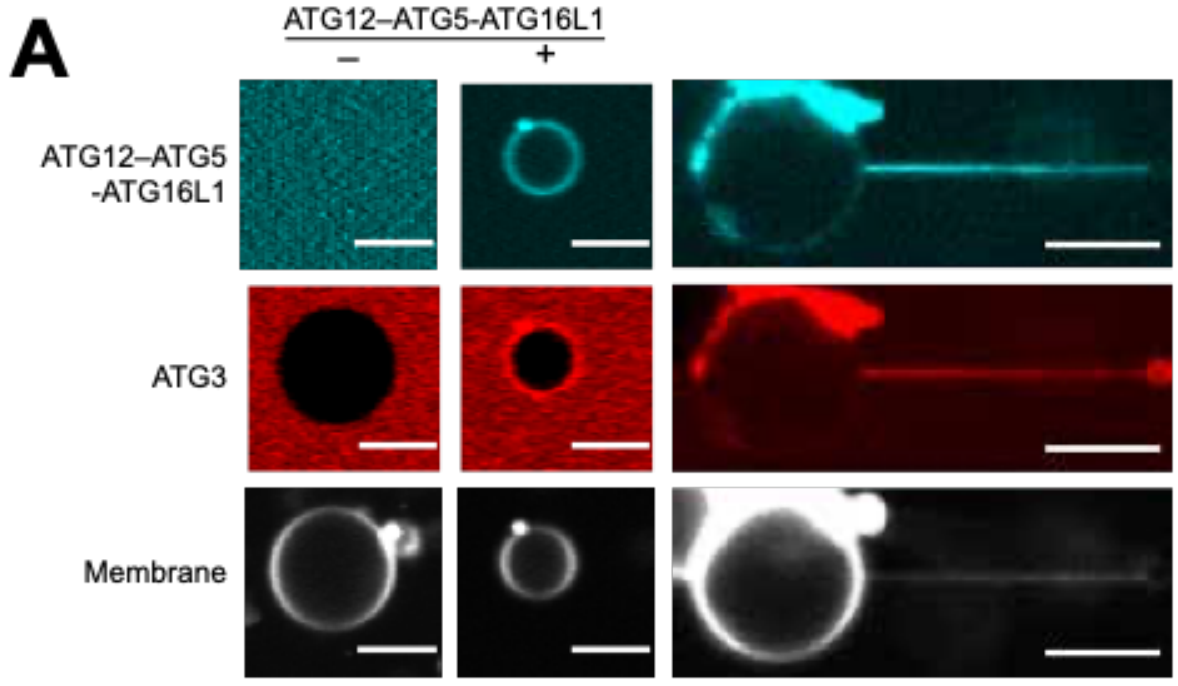
Figure 3.4 ATG12–ATG5-ATG16L1 senses curvature independently from ATG3
(**A**) ATG3 localization to GUVs and membrane tubes in the presence and absence of ATG12–ATG5-ATG16L1. Scale bars, 10 μm. (**B**) Curvature dependence of ATG12–ATG5-ATG16L1 sorting on membrane tubes in the presence (n = 9, r^2 = 0.86) and absence (n = 12, from <u>Fig. 2A</u>, r^2 = 0.72) of ATG3. Each data point represents an individual membrane tube.
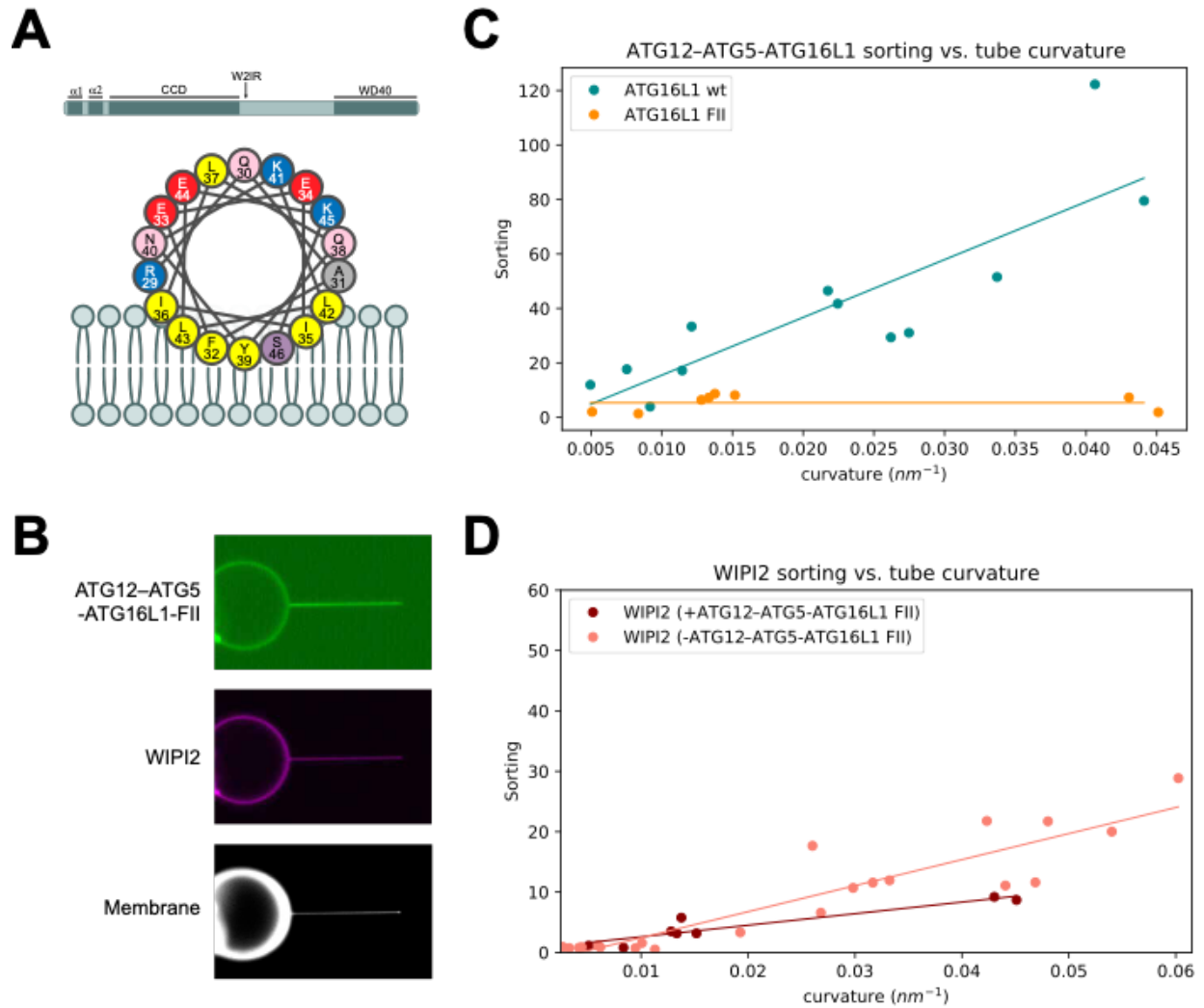
Figure 3.5 Mutagenesis affects ATG12–ATG5-ATG16L1 curvature sensitivity
(**A**) Graphical representation of the domain architecture of ATG16L1 and of the α2 membrane binding amphipathic helix. (**B**) Representative fluorescence microscopy image of E3-FII and WIPI2 localization on GUV and membrane tube surface. (**C**) Sorting versus curvature plot for ATG12–ATG5-ATG16L1 wt (n = 12, from Fig. 2A) compared to FII mutant (n = 8). (**D**) Sorting versus curvature plot for WIPI2 alone (n = 18, from Fig. 1D) or in the presence of ATG12–ATG5-ATG16L1 FII mutant (n = 8).

Mutation of helix2 also ablates LC3 lipidation activity

The loss of curvature sensitivity by the FII mutant is consistent with the previous report that ATG16L1 α2 is essential for LC3 lipidation and autophagosome formation (Lystad et al., 2019). In that report, it was shown that recruitment of ATG16L1 to WIPI2 puncta, which mark sites of autophagy initiation, is unimpaired. Similarly, we found that GUV recruitment of the ATG12–ATG5-ATG16L1 FII mutant, which blocks membrane recruitment by α2, is unimpaired, because WIPI2 binding through the WIPI2-interacting region of ATG16L1 drives this process. The α2 mutant leaves intact the ATG12-5 unit, responsible for the recruitment of ATG3 and, in turn, for LC3 lipidation. Nevertheless, we found that mutation of helix α2 abolished LC3 lipidation activity in vitro, consistent with (Lystad et al., 2019). We found that this was the case even in the presence of WIPI2 (Figure 3.6). In the presence of wildtype ATG16L1, LC3 is efficiently lipidated onto SUVs regardless of the presence of WIPI2, as observed by an increase in mobility of the LC3 band observed by SDS-PAGE of the lipidation reaction. In the presence of the FII mutant of ATG16L1, however, no LC3 is lipidated to SUVs even in the presence of WIPI2 after 2 hours incubation at 37˚C. Thus, ATG16L1 helix α2 has nonseparable roles in LC3 lipidation, directing ATG12–ATG5-ATG16L1 to sites of high curvature, and potentially in stabilizing the rim of the nascent phagophore.

ATG12–5-16L1 induces membrane curvature at high densities

Thermodynamic principles of curvature sensing proteins dictate that at sufficiently high protein density, a curvature sensor becomes a curvature inducer (Simunovic et al., 2016). Therefore, we wondered if ATG12–ATG5-ATG16L1 could induce membrane curvature at high surface densities at a physiologically plausible bulk concentration (100 nM). We analyzed time course images from nanotubes incubated with mCherry-WIPI2 and ATG12–ATG5-ATG16L1-GFP (Figure 3.3), assessing how membrane tube radius changed with increasing protein surface density on the membrane tube. In these experiments, protein is preincubated with GUVs before the membrane tube is formed; after pulling the membrane tube, protein diffuses onto the tube from the GUV until it reaches its equilibrium sorting value. Taking advantage of the changing protein surface density, we measured the tube radius before and after protein enrichment on the membrane tube. Enrichment of ATG12–ATG5-ATG16L1 on membrane tubes consistently correlated with a concomitant decrease in tube radius (Figure 3.7A). Visualizing a single representative tube over the course of several minutes shows that protein enrichment on the tube from ~600 to ~1700 dimers/μm^2 induces an increase in curvature from 50nm to 25nm radius, as calculated from the decrease in the fluorescence signal from the membrane label in the tube (Figure 3.7B, C). A decrease in fluorescence was not observed on tubes with already high curvature (Figure 3.7A).

In contrast, when the curvature of membrane tubes in the presence of only mCh-WIPI2 was monitored over time, no curvature induction was observed (Figure 3.8). This result is consistent with a model of protein density inducing membrane curvature. Because WIPI2 does not become highly enriched on the membrane tube, it does not reach sufficient surface density to alter the membrane curvature of the tube. Thus, this result does not indicate that WIPI2 *cannot* induce membrane curvature, but simply that it does not reach high enough densities to do so given the conditions of the experiment. Nevertheless, the lack of membrane curvature induction by WIPI2 importantly shows that membrane tube constriction in the presence of ATG12–ATG5-ATG16L1 is specific to the recruitment of ATG12–ATG5-ATG16L1.
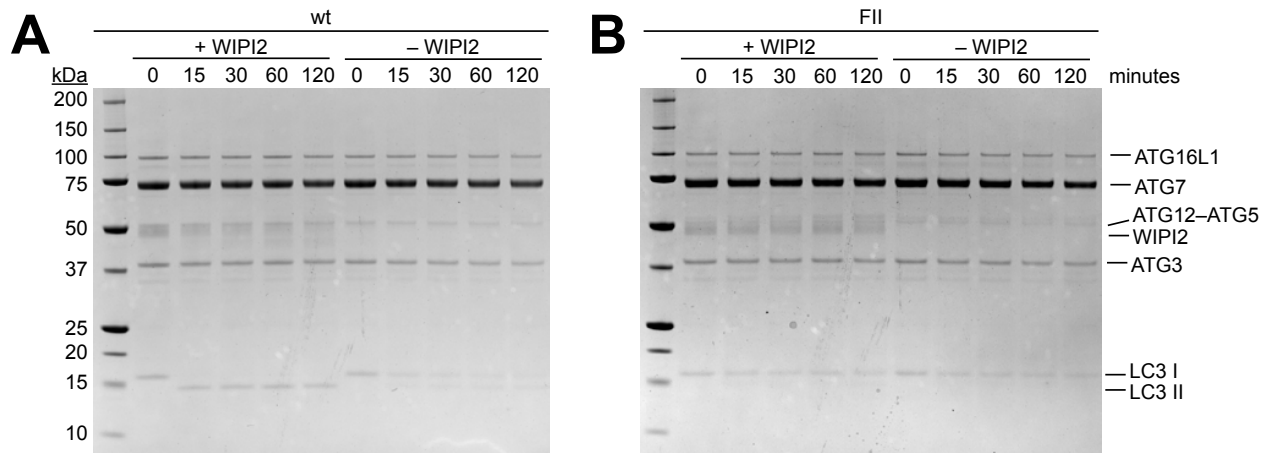
Figure 3.6 LC3 lipidation assay on SUVs
SDS-PAGE of LC3 lipidation reaction performed with purified proteins on SUVs in the presence of wildtype (A), or FII mutant (B) ATG16L1 protein. Reactions were performed with ATG3, ATG7, ATG12–ATG5-ATG16L1, LC3B, and +/– WIPI2. Gels show timepoints taken after incubation at 37˚C for 0, 15, 30, 60, and 120 minutes, in the presence of WIPI2 on the left of each gel, and in the absence of WIPI2 on the right. Lipidation of LC3 was monitored by increased mobility of the LC3 band, indicating conversion from LC3-I to the lipidated LC3-II.
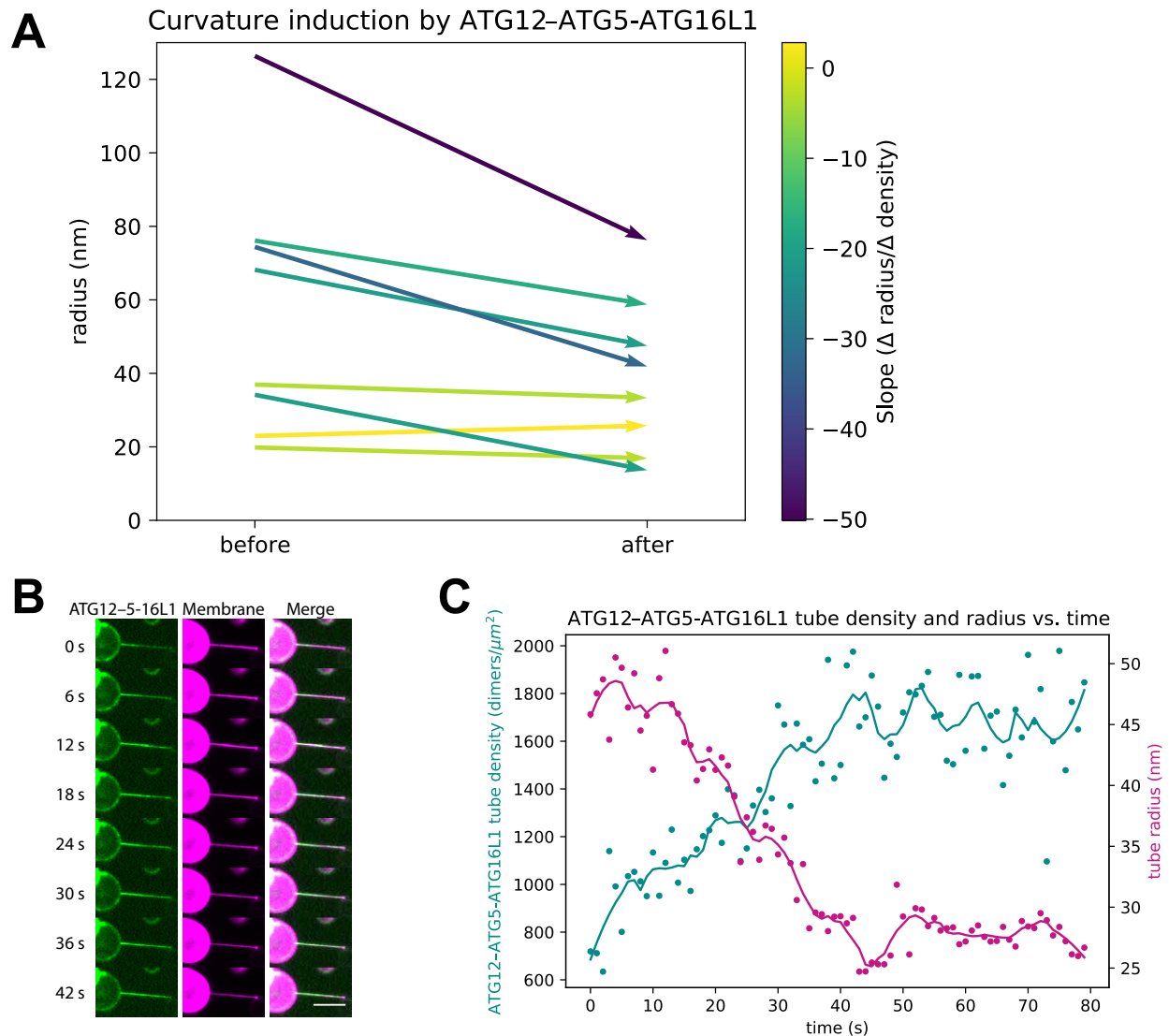
Figure 3.7 Curvature induction by ATG12–ATG5-ATG16L1

(**A**) Initial and final tube radii after the accumulation of ATG12–ATG5-ATG16L1 onto the membrane tube. Vectors color-coded for slope of the change in protein density over the change in tube radius, where darker colors indicate a steeper negative slope. (**B**) Montage of a single representative membrane tube showing ATG12–ATG5-ATG16L1 localization relative to the tube and membrane tube intensity over time. Snapshots of a continuous acquisition every 6 s, showing ATG16L1-GFP (green) and ATTO647N-DOPE membrane (magenta). Scale bars, 10 μm. (**C**) Quantification of protein binding and membrane tube radius from time course in (B). Surface density of ATG16L1 dimers on the membrane tube (cyan) and membrane tube radius (magenta) plotted against time (s) for an 80-s time course.
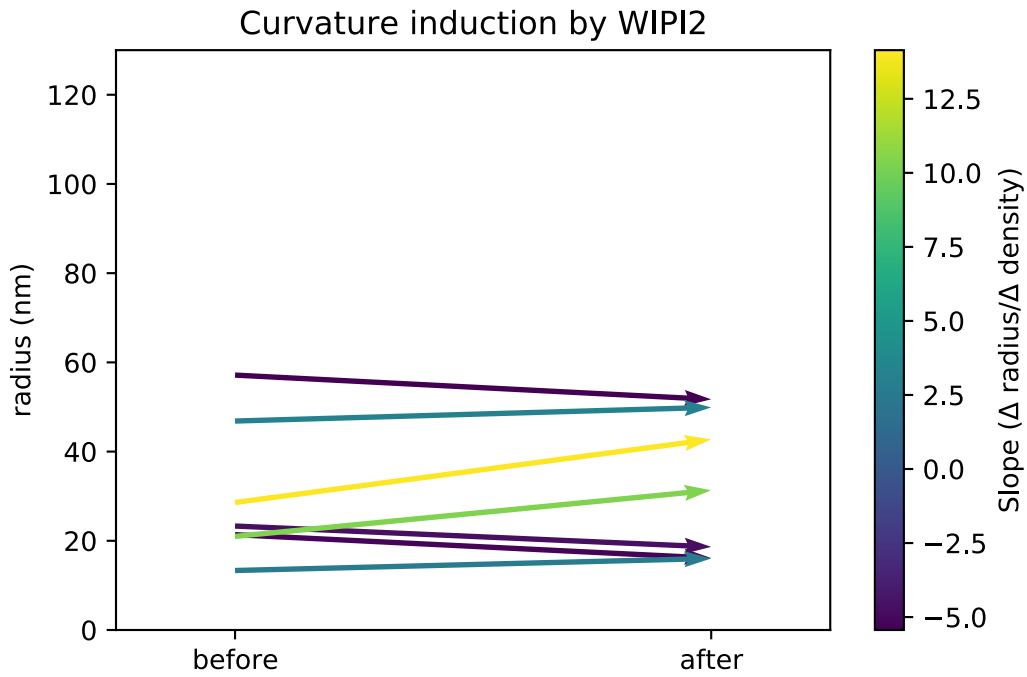
Figure 3.8 WIPI2 enrichment on membrane tubes does not constrict tubes
Tube radii before and after the accumulation of WIPI2 onto the membrane tube. Vectors color-coded for slope of the change in protein density over the change in tube radius, where darker colors indicate a steeper negative slope.

ATG12–ATG5-ATG16L1 retains curvature sensitivity independent of proper PROPPIN recruitment

Previous work has shown that ATG16L1 can be recruited to membranes by other PROPPIN proteins, including a yeast homolog of WIPI2, Atg21. Atg21 binds to a DE motif closer to the N-terminus of ATG16L1 (D101, E102), whereas WIPI2 binds to a region C-terminal to the coiled coil of ATG16L1 (Q217-E230) (Dooley et al., 2014; Strong et al., 2021). Recruitment of ATG12–ATG5-ATG16L1 by Atg21 does not stimulate the activity of ATG12–ATG5-ATG16L1 as does WIPI2 and is insufficient to promote the positive feedback loop to PI3KC3-C1 observed in the WIPI2/ATG12–ATG5-ATG16L1 system (Fracchiolla et al., 2020). Because Atg21 binds to ATG16L1 through an alternative site to WIPI2, we reasoned that Atg21-mediated recruitment of ATG12–ATG5-ATG16L1 to membranes might alter the conformation of the complex in a manner that would impact its membrane curvature sensitivity.

We pulled membrane tubes in the presence of Atg21 and GFP labeled ATG12–ATG5-ATG16L1 and compared the membrane tube enrichment of ATG12–ATG5-ATG16L1 to that in the presence of WIPI2. We found in initial experiments that ATG12–ATG5-ATG16L1 was still able to robustly partition onto the membrane tube (Figure 3.9), indicating that the curvature sensitivity of the ATG12–ATG5-ATG16L1 complex is independent of any conformational changes effected by Atg21-mediated recruitment.

Molecular dynamics simulations of curved membrane binding

To clarify the mechanism of membrane association and curvature sensing by ATG16L1, we performed molecular dynamics simulations. Structural work has shown how the N-terminus of ATG16L1 interacts with the other subunits of the ATG12–ATG5-ATG16L1 complex via helix α1 (Otomo et al., 2013). In atomistic molecular dynamics simulations of helix α2 of ATG16L1 as bound to ATG12–5 near negatively charged membranes (Figure 3.10A), membrane association of ATG16L1 occurred within the first few nanoseconds of each 1 μs replicate. A stable interaction interface was maintained between α1 and ATG5 (Figure 3.11A). Helix α2 exhibited considerable flexibility relative to α1, with swinging and rotation about the hinge region around Gln30 and Ala31. This led to spontaneous reorientation (by up to ~190° relative to the initial conformation; Figure 3.11B) of the hydrophobic face of α2, with the side chains of Phe32 and Ile36 brought to the protein-membrane interface (Figure 3.10B) in two of five replicates (two of ten ATG16L1 molecules simulated). These observations are consistent with membrane binding by the N-terminal region of ATG16L1 via exposure and insertion of hydrophobic side chains of α2. However, even though the hydrophobic residues formed contacts with the lipids, they did not insert into the headgroup region of the bilayer on the timescale of the simulations. Instead, helices α1 and α2 of ATG16L1 remained above the membrane and formed primarily electrostatic interactions of their basic residues, frequently involving negatively charged lipids (Figure 3.10B).

To examine the membrane binding configuration of ATG12–ATG5-ATG16L1 brought about by rotation of α2, a separate set of simulations was initiated using a remodeled structure of ATG16L1. Here, the hydrophobic face of α2 was embedded into the membrane prior to simulation (Figure 3.10C). Over a total simulation time of ~1.8 μs across six independent copies of the molecule, the side chains of Phe32, Ile35, and Ile36 remained stably embedded within the
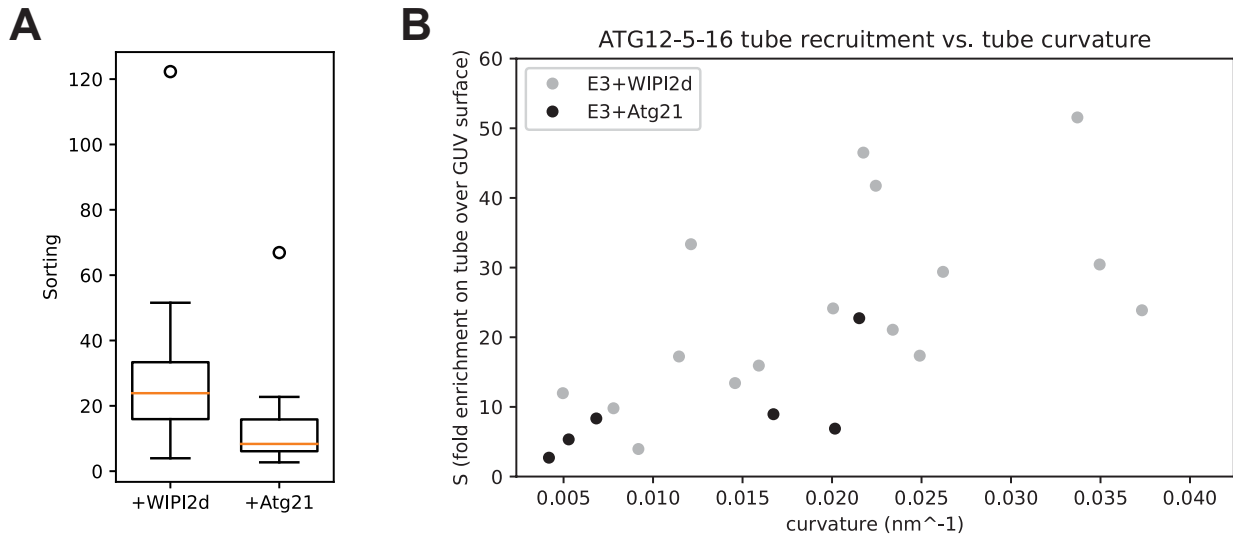
Figure 3.9 Curvature sensitivity of ATG12–ATG5-ATG16L1 with different PROPPINs
(**A**) Boxplot showing enrichment of ATG12–ATG5-ATG16L1 on membrane tubes in the presence of WIPI2 or Atg21. (**B**) Sorting vs. curvature plot showing enrichment of ATG12–ATG5-ATG16L1 in the presence of WIPI2 (grey) or Atg21 (black) at varying membrane tube curvature.
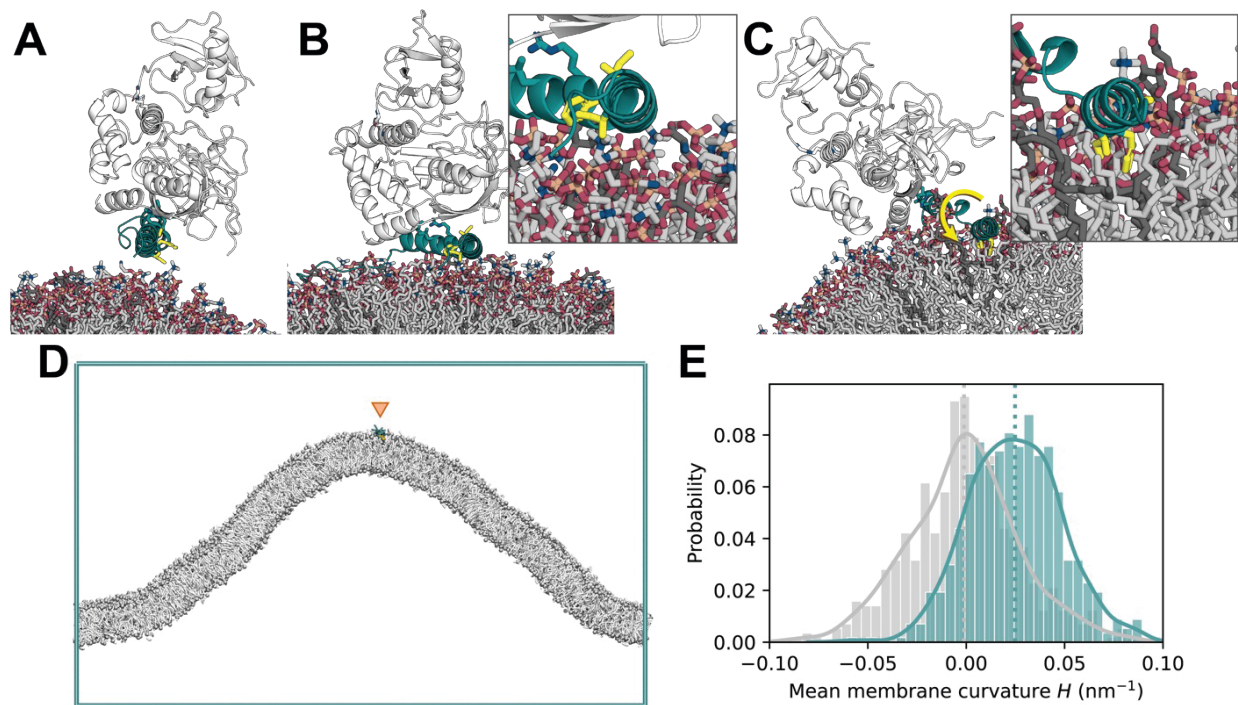
Figure 3.10 ATG16L1 helix α2 shows preference for positive curvature in MD simulations
(**A**) Initial structure (PDB ID: 4NAW) of ATG16L1 helix α2 (cyan) in complex with ATG12-5 (white) near the membrane. The hydrophobic-face residues Phe[32], Ile[35], and Ile[36] are highlighted as yellow sticks. Negatively charged lipids [PI(3)P, POPI, and DOPS] are shown as dark gray sticks, with neutral lipids (DOPC and DOPE) in lighter gray. (**B**) Snapshot of ATG1612–5-L1 interacting with the membrane surface during one (1 μs) simulation replicate, with rotation of the hydrophobic face by ~180°. (**C**) End frame of a 300-ns replicate with helix α2 embedded into the membrane. (**D**) End frame of a 50-μs coarse-grained curvature sampling simulation replicate with ATG16L1 helix α2 (residues 26 to 45; located at the positively curved cusp of the membrane fold). (**E**) Probability histogram of local mean curvature values sampled at the center of mass of helix α2 (cyan) and at random lipid phosphate positions (gray) during the same simulations, with data collected over six independent 50-μs replicates, after an equilibration period of 5 μs upon each membrane binding event.

membrane (Figure 3.11C) and maintained interactions with lipid acyl tails, whilst α1 mediated contact with ATG12–5 above the membrane (Figure 3.10C).

Amphipathic helix motifs have previously been shown to recognize packing defects in membranes, which increase with increasing membrane curvature(Bigay et al., 2005; Cui et al., 2011; Drin et al., 2007; Vamparys et al., 2013; Vanni et al., 2014; Vanni et al., 2013). The curvature preference of helix a2 was assessed using coarse-grained molecular dynamics simulations of the isolated ATG16L1 construct (residues 26-45) on buckled membranes (Bhaskara et al., 2019) (Figure 3.10D). In these longer (50 μs) simulations, multiple membrane insertion and dissociation events were observed on a microsecond timescale. During its periods of membrane association, α2 diffused within the buckled membrane and showed a strong preference for regions with high positive local curvature. Sampling at the center of mass of α2 (and allowing for an equilibration period for the helix to reach its preferred membrane regions), the distribution of local mean curvature H of the membrane profile showed a clear shift towards positive curvature relative to random samples of lipid headgroup positions, with a mean value of $H\sim0.025$ nm^{-1} (Figure 3.10E).

Residues 272-296 within the 6CD loop of WIPI2d (Strong et al., 2021) were identified to constitute a candidate curvature-sensing element based on secondary structure prediction (Drozdetskiy et al., 2015), analysis of physicochemical properties (Gautier et al., 2008), and atomistic molecular dynamics simulations. The prediction of two short amphipathic α-helices, respectively consisting of residues 272-284 and 290-296 (Figure 3.11D), was corroborated by observations of spontaneous helix formation and membrane interaction in these regions during atomistic molecular dynamics simulations of WIPI2d near the membrane, initially with an unstructured 6CD loop. In further simulations of the protein with the two predicted helices pre-modeled into the structure, spontaneous membrane insertion of residues ~271-300 was observed within 1.5 μs in one replicate (Figure 3.11E). The two putative PI(3)P binding sites (Baskaran et al., 2012; Krick et al., 2012; Liang et al., 2019) of WIPI2d, formed by blades 5 and 6 of the β-propeller, respectively, were also optimally positioned to bind PI(3)P in such a configuration (Figure 3.11E). These observations agree with previous studies suggesting amphipathic helix formation and membrane insertion of the 6CD region in the orthologous Atg18 protein (Busse et al., 2015; Gopaldass et al., 2017). Coarse-grained curvature-sampling simulations of WIPI2d 6CD residues 263-300 on buckled membranes yielded a mean local curvature of $H\sim0.015$ nm^{-1} at the center of mass of the construct (Figure 3.11F), supporting its role as a curvature sensor, albeit with weaker curvature sensitivity (and stronger membrane binding) compared with helix α2 of ATG16L1 (Figure 3.10E).

Previous work modeling membrane association of membrane curvature generating proteins has highlighted the depth of helix insertion into the membrane as a key regulator of the magnitude of curvature sensitivity (Campelo et al., 2008). We plotted the insertion depth of all-atom trajectories of WIPI2 loop and ATG16L1 a2 helix membrane insertion. In the membrane-bound state, the height z of the geometric center of the α2 helix backbone was located   around the level of the phosphate groups. By contrast, the two short helices of the WIPI2d 6CD loop inserted deeper into the membrane by ~5% and ~20% of the thickness of the monolayer, respectively (Figure 3.12A). We observed the same trend in the insertion depths of α2 and 6CD
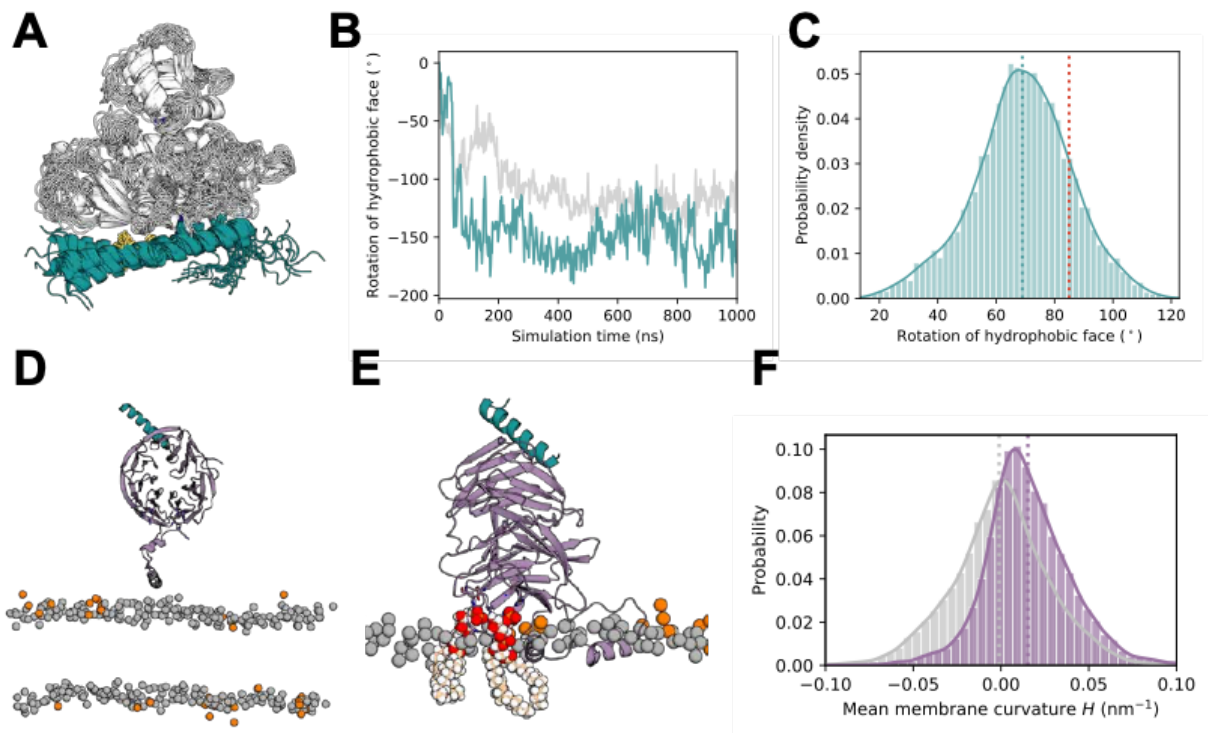
Figure 3.11 Membrane binding and curvature sensing of ATG12–5-16L1 and WIPI2d
(**A**) Flexibility of ATG16L1 helix 2, illustrated with a superimposition of ATG12-5–L1 conformations sampled at 50 ns intervals during one 1 μs simulation trajectory. The side chains of ATG16L1 helix 1 residues Ile17, Leu21, and Arg24 (cyan) at the interface with ATG5, and of helix 2 residues Phe32, Ile35, and Ile36 of the hydrophobic face (highlighted yellow) are shown in stick representation. (**B**) Reorientation of the helix 2 hydrophobic face of the aforementioned molecule (cyan) over the course of its simulation, and of a second copy of ATG12-5–L1 (grey) on the opposite membrane leaflet in the same replicate system. At each time point, the rotation angle (relative to the initial conformation) is defined by taking the outward-pointing normal to the plane through the Cα atoms of Phe32, Ile35, and Ile36. Rotation in the clockwise direction, as viewed from the C-terminal end of helix 2 corresponds to a positive value. (**C**) Distribution of helix 2 hydrophobic face rotation angles in simulations of a remodeled ATG16L1 structure in complex with ATG12-5, over a total simulation time of ~1.8 μs. Rotation angles are measured relative to the conformation in the crystal structure (PDB ID: 4NAW). The remodeled configuration had an initial value approximately in the –z direction into the membrane, as indicated by the red dotted line. The mean position of the distribution is indicated by the cyan dotted line. (**D**) Structure of WIPI2d (magenta) bound to residues 209-230 of ATG16L1 (PDB ID: 7MU2), with the WIPI2d 6CD residues 272-284 and 290-296 modelled as α-helices, placed above a PI(3)P-containing membrane. Residues forming the two putative PI(3)P binding sites in blades 5 and 6 are shown in stick representation. Phosphorus atoms of PI(3)P molecules are shown as orange spheres, with those of all other lipid headgroups colored grey. (**E**) Snapshot of WIPI2d after forming spontaneous membrane interactions during one (2 μs) simulation replicate, with residues ~271-300 embedded into the membrane. Two PI(3)P molecules, each occupying a binding site on WIPI2d, are highlighted as spheres. (**F**) Probability histogram of local mean curvature values sampled at the center of mass of WIPI2d 6CD residues 263-300 (magenta) and at random lipid phosphate positions (grey) during the same simulations, with data collected over the final 12 μs of six independent 20 μs replicate systems, each containing two copies of the protein construct, on either side of the buckled membrane.

in the coarse-grained simulation replicates (Figure 3.12B). Consistent with the membrane nanotube enrichment results, this finding supports a role for WIPI2 in strongly and stably associating with the membrane, whereas the ATG16L1 membrane insertion is responsible for weaker binding with heightened membrane curvature sensitivity.

Discussion

This study set out, in the first instance, to determine if ATG12–ATG5-ATG16L1 bound to membranes in a curvature-dependent manner in the physiologically relevant setting of WIPI2-driven recruitment. We found that WIPI2 is itself curvature-sensitive, but ATG12–ATG5-ATG16L1, following its recruitment by WIPI2, is even more sensitive. The sorting index for WIPI2-recruited ATG12–ATG5-ATG16L1 reaches a value of ~100 also seen for dedicated curvature sensors such as amphiphysin (Sorre et al., 2012). MD simulations show that WIPI2 inserts substantially into the hydrocarbon core of the membrane, while helix a2 of ATG16L1 inserts less deeply. Comparatively shallow membrane insertion into the upper part of the lipid monolayer by amphipathic helices has been shown to correlate with high curvature sensitivity (Campelo et al., 2008). Thus, the role of WIPI2 in this system is to drive membrane recruitment by binding tightly to PI(3)P and inserting deeply into the membrane, while ATG16L1 itself interacts weakly but in highly curvature dependent manner.

As noted previously (Sorre et al., 2009), curvature dependence is stronger at lower surface density. This likely represents the onset of saturation of the binding capacity of the membrane tube. It is also consistent with a model for curvature sensing in which self-association of ATG12–ATG5-ATG16L1 complexes with one another is neither required nor favorable. Curvature induction requires higher protein densities, at which the differential sorting of ATG12–ATG5-ATG16L1 to regions of high curvature is less evident.

There are some differences in the reported observations of ATG12–ATG5-ATG16L1 localization in cells between species. It is worth noting that ATG16L1 has almost negligible sequence similarity with yeast Atg16. The properties of yeast Atg16, which has been reported to tether (Romanov et al., 2012) and deform (Kaufmann et al., 2014) membranes, are therefore likely to differ from mammalian ATG16L1. In three-dimensional imaging of *Arabidopsis* cells, ATG5 is strikingly localized to toroidal zones that appear to correspond to the highly curved phagophore rim (Le Bars et al., 2014). In mammalian cells, however, two-dimensional EM imaging of thin sections in mouse embryonic stem cells suggested that ATG16L1 is uniformly localized on phagophores (Mizushima et al., 2001). Thus, the role of ATG12–ATG5-ATG16L1 in phagophore rim stabilization may vary in different organisms, cell types, and other conditions.

WIPI2 and ATG12–ATG5-ATG16L1 are exemplars of curvature-sensitive autophagy proteins whose curvature preference is strong enough that it could, in principle, contribute to stabilizing phagophore rim curvature. They are unlikely to be the only such proteins. Indeed, the binding and/or activity of mammalian PI3KC3-C1 (Ohashi et al., 2020) and ATG3 (Nath et al., 2014) have been shown to be curvature sensitive *in vitro*. We found that ATG3 does not further increase the curvature sensitivity of ATG12–ATG5-ATG16L1, however, this is likely to reflect saturation of the already very high sorting index for ATG12–ATG5-ATG16L1, making it difficult to measure any further incremental increase. Indeed, saturation of the measurement may have led us to underestimate the true curvature dependence of ATG12–ATG5-ATG16L1 itself. It
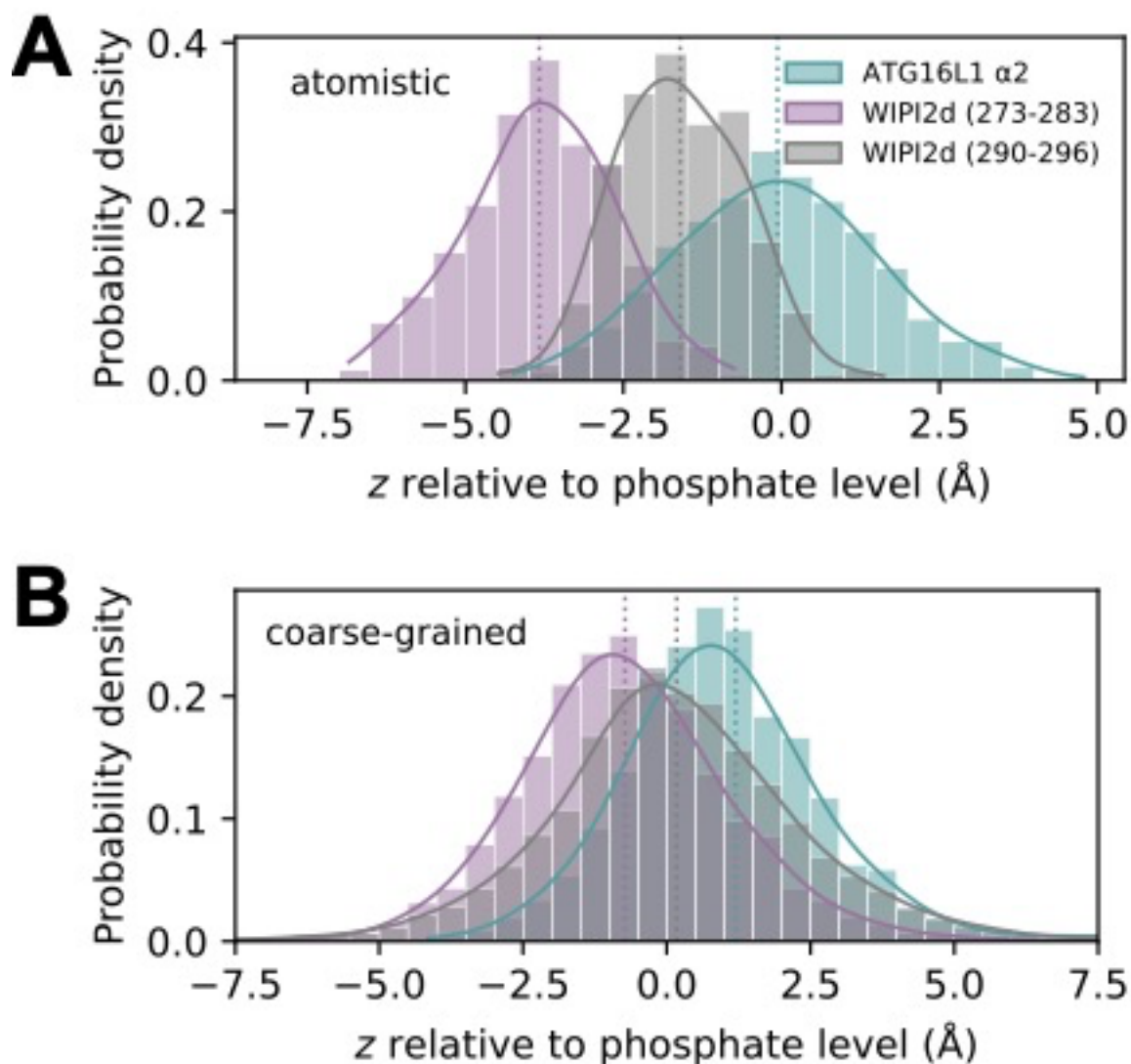
Figure 3.12 Membrane insertion depths of amphipathic helical elements within WIPI2d and ATG16L1

The z-positions of the center of geometry of WIPI2d (magenta) residues 273-283 (around a mean value of ~–3.6 Å) and 290-296 (~–1 Å) and of ATG16L1 helix α2 (cyan) are each measured relative to the level of phosphate groups of the membrane leaflet to which the protein is bound. The distribution of z-positions in one representative all-atom simulation replicate of WIPI2d or ATG12–5-16L1 is shown, respectively. Simulation trajectories are sampled at 1 ns intervals after an equilibration period following membrane insertion of the amphipathic helix.

seems reasonable that both PI3KC3-C1 and ATG3 could contribute to phagophore rim stabilization. *In vitro* data are still lacking for ATG2A, but its apparent phagophore rim localization (Sakai et al., 2020) makes ATG2A an intriguing candidate. Under curvature inducing conditions, it might be expected that the rim would be saturated and broader localization of ATG2A observed. At any rate, further biophysical and cell biological characterization of the curvature dependence of PI3KC3 and ATG2A, and comparison to the ATG12–ATG5-ATG16L1 data will be called for.

Finally, this study showed the power of using optically trapped membrane tubes to directly visualize the localization of autophagy proteins on a contiguous membrane surface of varying curvatures, analogous to the physiological curvature of a phagophore. Membrane tubes pulled from GUVs are currently the most powerful biophysical approach to disentangle multiplexed mechanisms of membrane affinity and membrane curvature sensitivity, like those observed in autophagy. Because autophagy proteins interact in a highly networked manner with one another, this method will be critical to distinguish the mechanisms of phagophore rim localization and stabilization from the stable recruitment of autophagy effectors to sites of autophagosome biogenesis. Importantly, such studies will be required to fully understand the physical basis of phagophore expansion, and to develop a more detailed model than proposed in Chapter 1 for how lipid flux, cargo adhesion, and membrane curvature impact cargo engulfment.

Methods

Protein Expression and Purification

ATG12–ATG5-ATG16L1-GFP constructs (RRID:Addgene_169077, Addgene_ 192290) were expressed and purified from Sf9 cells (ATCC Cat# CRL-1711, RRID:CVCL_0549) as described (Fracchiolla et al., 2020) (dx.doi.org/10.17504/protocols.io.br6qm9dw). Briefly, cells were resuspended in lysis buffer (50mM HEPES pH7.5, 300mM NaCl, 2mM TCEP, + Complete protease inhibitor (Roche)), and lysed by sonication. Lysate was clarified by centrifugation, and the soluble fraction applied to a streptactin Sepharose column (Cytiva). Upon elution from the strep column with 5mM desthiobiotin (Sigma), fractions were concentrated by filter centrifugation, and purified by gel filtration over a Superose 6 column (Cytiva). mCherry-WIPI2d (RRID:Addgene_178912) was expressed and purified from suspension HEK GnTI cells (Chang, Shi, et al., 2021) (dx.doi.org/10.17504/protocols.io.bvjnn4me). Cells were resuspended in lysis buffer (50mM HEPES pH7.5, 200mM $MgCl_2$, 10% glycerol, 1% Triton X-100, 1mM TCEP, +Complete protease inhibitor), and lysed by gentle rocking at 4°C for 30 minutes. Lysate was clarified by centrifugation, applied to a streptactin Sepharose column, and eluted with buffer containing 10mM desthiobiotin. GST-mCherry-FYVE (RRID:Addgene_192289, dx.doi.org/10.17504/protocols.io.ewov1n39pgr2/v1) and His-TEV-ATG3 (RRID:Addgene_169079, dx.doi.org/10.17504/protocols.io.btgknjuw) were expressed and purified from E. coli BL21(DE3) (NEB Cat# C2527) culture.

Protein Labeling

ATG3 was labeled with ATTO 565 NHS ester (ATTO-TEC). Briefly, 40µM ATG3 was mixed with 80µM ATTO 565 NHS ester in 50mM HEPES pH8.0, 150mM NaCl, 2mM TCEP. The reaction was carried out for 1 hour at room temperature, and buffer exchanged over a G-25 desalting column (Cytiva) into 50mM Tris, pH 8.0, 150mM NaCl, 2mM TCEP to quench the

reaction and remove any unconjugated dye. Labeling efficiency was assessed by the ratio of absorbance at 280 and 564 nm, correcting for dye absorbance at 280nm, using a Nanodrop spectrophotometer. (

GUV preparation

GUVs were prepared by polyvinyl alcohol (PVA) assisted swelling. Briefly, 100ul of 5% PVA was spotted onto a glass coverslip and dried at 50°C. 50nMol of lipids dissolved in chloroform were mixed (mol percent: 70% DOPC, 20% DOPE, 5% DOPS, 5% DO-PI(3)P, 0.3% ATTO647N-DOPE, 0.01% PEG2000-biotin-DSPE) and dried on the PVA layer overnight in a vacuum desiccator. GUVs were swelled for 30-60 minutes at room temperature in 100ul of sucrose solution slightly hypotonic to imaging buffer (320mOsm) as determined by freezing point depression osmometer (Osmette III, Precision Systems). (dx.doi.org/10.17504/protocols.io.3byl4b398vo5/v1)

Membrane Tube Assay

Proteins were mixed with fluorescently labeled GUVs and then added to a microscope chamber that had been passivated with 1mg/ml BSA in imaging buffer and subsequently rinsed with imaging buffer (20mM Tris, pH 8.0, 150mM NaCl, 2mM $MgCl_2$, 2mM TCEP). GUVs were allowed to settle before adding streptavidin coated silica beads (Spherotech) that had been diluted 1:1000 in imaging buffer. Using an optical trap, the bead was brought into contact with the biotinylated GUV surface and retracted to form a membrane tube. Protein bound to the GUV and tube membrane was monitored by confocal fluorescence imaging. (dx.doi.org/10.17504/protocols.io.ewov1n3dpgr2/v1)

Imaging and Image Analysis

Imaging of the membrane tubes was performed on a Nikon Ti-Eclipse microscope with Nikon A1 confocal unit, modified with an optical trap and micromanipulators (Cada et al., 2022; Schoneberg et al., 2018), using a Plan Apochromat 60X/1.20 water immersion objective (Nikon). A complete image dataset for this paper can be found at (10.5281/zenodo.6508734). Image files were processed in ImageJ (https://imagej.nih.gov/ij/, RRID:SCR_003070) to generate regions of interest (ROIs) containing segments of the membrane tube or of the GUV surface. ROIs were combined and analyzed using custom Python scripts (https://github.com/livjensen7/Jensen_etal_2022). Briefly, the ROIs were segmented based on the intensity of the membrane dye channel with an Otsu threshold for local maxima, and protein binding signal was quantified as the average value in the protein label channel masked with the membrane channel segmentation. Background was calculated as the average value of pixels not in the membrane channel mask and subtracted from the signal as calculated above. Protein enrichment on membrane tubes (S) was calculated as a ratio of protein intensity on the tube to protein intensity on the GUV surface, normalized for membrane intensity:

$$S = \frac{\frac{I_{prot,tube}}{I_{mem,tube}}}{\frac{I_{prot,GUV}}{I_{mem,GUV}}},$$

where I_{prot} and I_{mem} are the average intensity values from the ROI for the protein or membrane fluorescence channel, on the tube or GUV surface. (dx.doi.org/10.17504/protocols.io.5jyl891e9v2w/v1)

Tube Radius Calculation

　　Tube radii were calculated using a previously described method (Prevost et al., 2017) in which the ratio of membrane dye fluorescence in the tube ROI to that in the GUV ROI is multiplied by an experimentally derived calibration constant (k_{tub}):

$$R = k_{tub}\left(\frac{I_{mem,tube}}{I_{mem,GUV}}\right),$$

where R is the tube radius, and $I_{mem,tube}$ and $I_{mem,GUV}$ are the average intensity values of the membrane dye from the tube or GUV ROI.

　　To determine the value of k_{tub}, tubes were pulled from GUVs held on an aspiration pipette, and the membrane tension varied by changing the aspiration force with a microfluidic controller (MFCS-EZ, Fluigent) to generate tubes of varying radii. Membrane tension (σ) was determined from aspiration pressure and microscopy images as:

$$\sigma = \Delta P \frac{r_{pip}}{2(1-\frac{r_{pip}}{r_{GUV}})},$$

where ΔP is the difference in aspiration pressure from baseline, and r_{pip} and r_{GUV} are the radii of the aspiration pipette and the GUV, respectively.

　　Tube radius was subsequently calculated from membrane tension and force (F) felt by the bead in the optical trap as:

$$R = \frac{F}{4\pi\sigma},$$

and plotted against the ratio of tube to GUV membrane fluorescence (Fig. S1B). Then, k_{tub} was extracted from the slope of a linear least squares regression. (dx.doi.org/10.17504/protocols.io.x54v9y3rqg3e/v1)

Surface Density Calculation

　　Protein density on the GUV surface was calculated by drawing a relationship between known concentrations of protein and membrane label in bulk solution and on the GUV surface (Prevost et al., 2017). First, standard curves of GFP and DOPE-ATTO488 were generated from a serial dilution in imaging buffer + 0.1% Triton X-100. The ratio of the slopes of the linear fits was used to correct for differences in optical properties of the different fluorophores. Then, the fluorescence intensity of GUVs containing a range of known percentages of dye-conjugated lipid (0.01-1 mol%) was calculated and plotted against surface density of the dye-conjugated lipid (assuming 0.7nm^2/lipid) to give a relationship between intensity and GUV surface density. This was corrected by the ratio of intensities of the fluorophores in bulk solution. (dx.doi.org/10.17504/protocols.io.81wgb65nnlpk/v1).

LC3 lipidation assay

　　LC3B *in vitro* lipidation reaction was carried out as in (Fracchiolla et al., 2020). Liposomes extruded to 400nm from a 1mg/ml lipid suspension (70% DOPC, 20% DOPE, 5% DOPS, 5% PI(3)P) were mixed 1:1 with purified lipidation components to a final concentration of 1μM ATG3, 1μM ATG7, 500nM WIPI2, 100nM ATG12–5-16L1-GFP, 2.5μM LC3B in a reaction buffer containing 20mM Tris, pH8.0, 150mM NaCl, 1mM MgCl$_2$, 1mM TCEP, 1mM ATP. The reaction mix was incubated at 37˚C, and fractions were removed at 0, 15, 30, 60, and 120 minutes, quenched by adding 1x SDS loading buffer and heating to 60˚C for 10 minutes. LC3 lipidation was assessed by Coomassie-stained SDS-PAGE.

Molecular dynamics simulations

Molecular dynamics simulations were performed with GROMACS 2020 (Abraham et al., 2015), using the CHARMM36m force field (Huang et al., 2017) for all-atom simulations and the MARTINI 3 force field (Souza et al., 2021) and Gō-MARTINI model (Poma et al., 2017) for coarse-grained systems.

Atomistic models of the ATG12–ATG5-ATG16L1 and WIPI2d-ATG16L1 complexes were based on crystal structures with PDB IDs 4NAW (Metlagel et al., 2014) and 7MU2 (Strong et al., 2021), respectively. The ATG16L1 N-terminal helix in the former complex was replaced by a more complete structure (PDB ID: 4TQ0 (Kim et al., 2015)) and residues 1-9 were added using the DEMO server (Zhou et al., 2019) to give a model of residues 1-50. A second model of the same region was generated in PyMOL (Delano, 2002) by rotation of helix α2 relative to α1 at the Gln30/Ala31 hinge. For WIPI2d, residues 262-299 of the 6CD region were modeled either (i) as an unstructured loop using SWISS-MODEL (Waterhouse et al., 2018) or (ii) with two short helices based on the structure predicted by AlphaFold (Jumper et al., 2021; Varadi et al., 2022), in two alternative models. Unstructured ATG12 residues 1-52 and WIPI2d residues 1-11 and 362-425 were excluded from the models. The Lys130 side chain of ATG5 was connected to the backbone carbonyl of ATG12 Gly140 by an isopeptide bond. Exposed N- or C-terminal groups at the end(s) of each incomplete structure or truncated construct were neutralized. His183 and His255 at the putative PI(3)P binding sites of WIPI2d were protonated.

All membranes were prepared initially in a coarse-grained representation using the *insane* method (Wassenaar et al., 2015) and consisted of 60% DOPC, 20% DOPE, 5% DOPS, 10% POPI, and 5% PI(3)P based on the ER lipid composition (Li et al., 2021). Buckled membranes were constructed using LipidWrapper (Durrant & Amaro, 2014) by fitting the height (amplitude) of the membrane as a sine function of its *x*-coordinate. For all-atom simulations, the CG2AT2 tool (Vickery & Stansfeld, 2021) was used to convert each equilibrated membrane system to an atomistic representation. All simulation systems were solvated with 150 mM of aqueous NaCl, using TIP3P or coarse-grained water. Atomistic models of ATG12–ATG5-ATG16L1 or WIPI2d were placed above membranes after CG2AT2 conversion (upon removal of coarse-grained solvent). In the case of the remodeled ATG16L1, the embedded helix α2 configuration was obtained by insertion into either leaflet of the buckled membrane at the coarse-grained stage, with all particles of the helix around or below the level of phosphate particles and the hydrophobic face oriented towards the membrane core. Lipids clashing with the embedded helix were removed from both leaflets, followed by protein-membrane equilibration and CG2AT2 conversion of the system as described above. The CG2AT2 'align' option was used, with the initial atomistic ATG12–ATG5-ATG16L1 complex containing the remodeled ATG16L1 (in its conformation prior to simulation) aligned to and replacing the back-mapped protein in the CG2AT output for subsequent equilibration. Simulation replicates were independently prepared and equilibrated, with the simulation cells having approximate dimensions of 14 x 14 x 20 nm^3 for atomistic WIPI2d simulations, 32 x 14 x 28 nm^3 for simulations of atomistic ATG12–ATG5-ATG16L1 on either side of curved membranes (with two copies per replicate system), and 63 x 28 x 38 nm^3 for coarse-grained curvature-sampling simulations. The *xy* dimensions of buckled membrane systems were fixed during simulation.

Each coarse-grained membrane system was equilibrated for 200 ns, with atomistic systems further equilibrated for 10 ns upon conversion from coarse-grained representation. Harmonic positional restraints were applied to non-hydrogen protein atoms or backbone beads during equilibration, with a force constant of 1000 kJ mol^{-1}. In the case of buckled membranes, a weaker (10 kJ mol^{-1}) restraint in z was also applied to the phosphorus atoms or phosphate beads of lipid headgroups to preserve the initial distance between protein and membrane at the equilibration stage. System temperature and pressure were maintained at 310 K and 1 bar, using the velocity-rescaling thermostat (Bussi et al., 2007) and a semi-isotropic Parrinello-Rahman barostat (Parrinello & Rahman, 1981) during the production phase. Atomistic and coarse-grained systems were simulated with integration time steps of 2 fs and 20 fs, respectively. For the atomistic simulations, long-range electrostatic interactions were treated using the smooth particle mesh Ewald method (Darden et al., 1993; Essmann et al., 1995) with a real-space cut-off of 1 nm, a Fourier spacing of 0.12 nm, and charge interpolation through fourth-order B-splines. The LINCS algorithm was used to constrain covalent bonds involving hydrogen atoms (Hess et al., 1997).

Simulation trajectories were analyzed through MDAnalysis 2.0 (Gowers et al., 2016; Michaud-Agrawal et al., 2011) in Python 3.6. The local curvature of buckled membranes during simulation was estimated using the MemCurv software package (https://github.com/bio-phys/MemCurv) following the protocol established by Bhaskara et al. and the same parameter settings as previously described (Bhaskara et al., 2019). Sampling at 10 ns intervals, membrane profiles were approximated using a 2D Fourier expansion and optimized by least-squares fitting. The mean curvature H at any given position of interest were derived from the shape operator of the approximated profile along the membrane surface (Bhaskara et al., 2019).

Chapter 4: Membrane curvature sensing by members of the Class III PI3K complex family

Introduction

Another pair of core autophagy complexes that are known to sense membrane curvature are the VPS34-containing class III phosphatidylinositol-3-phosphate kinase complexes I and II (Complex I and Complex II). These kinase complexes are heterotetrameric assemblies that share the subunits Beclin1 (BECN1), VPS34, and VPS15. The fourth subunit is ATG14L in the case of Complex I, or UVRAG for Complex II. Complex I acts early in autophagy to generate PI(3)P that recruits downstream autophagy effectors such as the WIPI family of proteins (Figure 4.1). Complex II plays a role in autophagosome maturation as well as in endosome trafficking. Both Complex I and Complex II preferentially bind small vesicles over large vesicles *in vitro*, although C1 binds to membranes with higher affinity (Brier et al., 2019). The C-terminal BATS domain of ATG14L directs Complex I to curved membranes (Fan et al., 2011). The curvature sensitivity of Complex II has been less well-characterized. We set out to investigate the molecular mechanisms of membrane curvature sensing by both Complex I and Complex II to uncover the basis for their differential regulation in the cell and activity at different stages of autophagy.

While the BATS domain of ATG14L contains an ALPS motif (472-488) that is critical for the high affinity recruitment of C1 to membrane surfaces, both C1 and C2 contain other known membrane associating motifs, summarized in
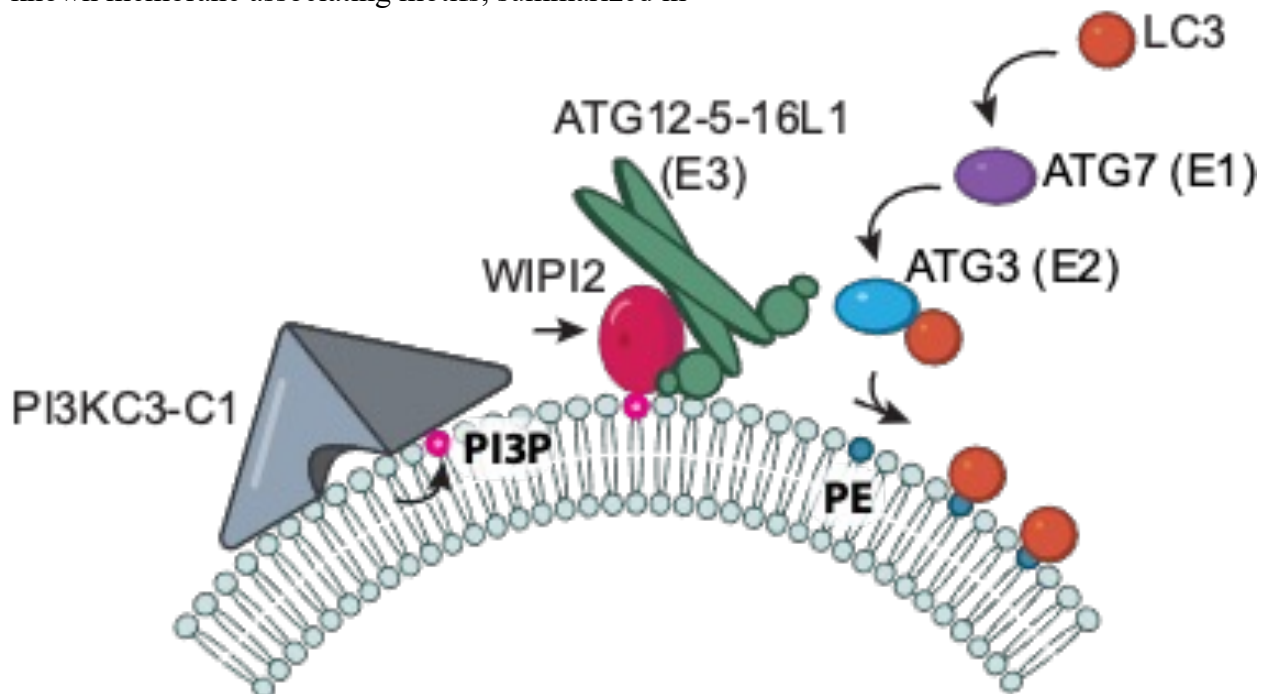

Figure 4.1 PI3KC3-C1 acts upstream of LC3 lipidation machinery
PI3KC3-C1 catalyzes the production of PI(3)P, which recruits the LC3 lipidation machinery through WIPI2.

Table 4.1. BECN1 contains several membrane interacting regions, including an aromatic finger in its BARA domain (F359, F360, W361) and a double phenylalanine motif (F270, F274) that also interacts with membranes in a manner dependent on regulation by dynamics of β sheet 1 in its BARA domain (Chang et al., 2019; Huang et al., 2012). Additionally, hydrogen deuterium exchange coupled to mass spectrometry (HDX-MS) reveals that several other regions in BECN1 that are protected in the presence of membranes (Ohashi et al., 2020). VPS15 is myristoylated at its N-terminus, although its myristoylation is dispensable for membrane association and normal growth in yeast (Herman et al., 1991). Finally, the catalytic subunit VPS34 also interacts with membranes through its activation loop and its C-terminal helix(Rostislavleva et al., 2015). The C-terminal helix of VPS34 is not only essential for catalytic activity of the kinase but is also protected by membranes in HDX-MS experiments (Miller et al., 2010; Ohashi et al., 2020). In addition to the intrinsic membrane association of the PI3K complexes, they also form complexes the small GTPases Rab1 and Rab5 (Christoforidis et al., 1999; Tremel et al., 2021).

The molecular architecture of the Class III PI3K complexes has been extensively studied, revealing regulatory sites on an overall v-shaped structure (Baskaran et al., 2014; Chen et al., 2023; Miller et al., 2010; Rostislavleva et al., 2015; Tremel et al., 2021; Young et al., 2019). Together with biochemical evidence for multiple membrane targeting regions within Complex I and Complex II, the structural information provides a framework for investigating how these varied membrane interactors could work together to interface with a membrane surface. Because the engagement of multiple membrane curvature sensing motifs has been shown to amplify the curvature sensitivity of other proteins *in vitro* (Mesmin et al., 2007), we reasoned that the presence of many membrane association regions, while not necessarily highly curvature sensitive on their own, might contribute to the overall curvature sensitivity of the PI3KC3 complexes.
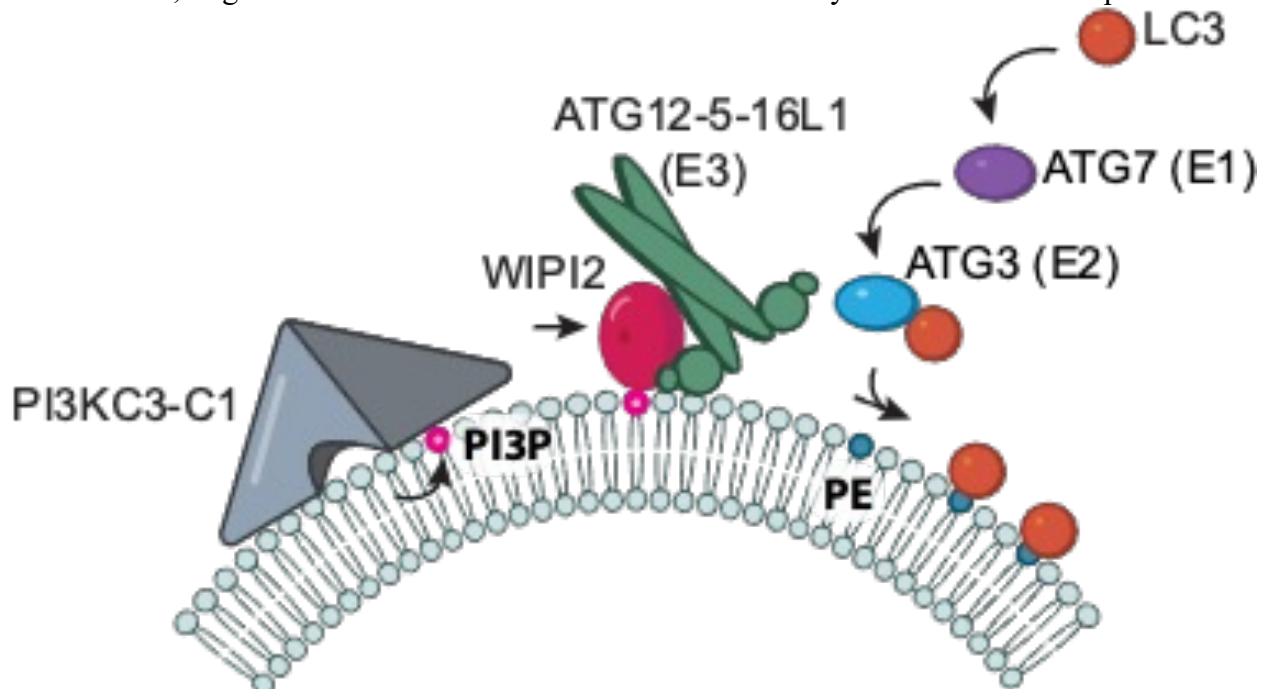

Figure 4.1 PI3KC3-C1 acts upstream of LC3 lipidation machinery
PI3KC3-C1 catalyzes the production of PI(3)P, which recruits the LC3 lipidation machinery through WIPI2.

Table 4.1 Membrane interacting regions in PI3KC3 complex subunits

Protein	Membrane interacting residues	Source
ATG14L	ALPS motif (472-488)	(Fan et al., 2011)
BECN1	Aromatic finger (F359, F360, W361)	(Huang et al., 2012)
BECN1	FF motif (F270, F274)	
VPS15	N-terminal myristoylation	
VPS34	Activation loop	
VPS34	C-terminal helix	

Results

To characterize the curvature sensitivity of the PI3K complexes, I again set out to reconstitute the membrane association of purified fluorescently labeled protein with membrane tubes pulled from GUVs with an optical trap. Because the curvature sensitivity of Complex I has been most well-studied, I first purified wild type Complex I to quantify its curvature sensitivity on membrane tubes. I purified Complex I containing fluorescently labeled GFP-ATG14L from suspension HEK cell culture and incubated it with GUVs (65% DOPC, 20% DOPE, 10% DOPI, 5% DOPS, 0.3% ATTO647N DOPE, 0.01% DSPG-PEG2000-biotin). Consistent with previous data showing that Complex I preferentially associates with highly curved vesicles, I observed a curvature dependence of Complex I localization on membrane tubes pulled from GUVs (Figure 4.2A, B). At low surface densities, Complex I had increasing enrichment on membrane tubes with increasing curvature, up to 50-fold enriched on membrane tubes compared to the GUV surface.

I next repeated the experiment with GFP-UVRAG labeled Complex II, to compare the curvature sensitivity of the two complexes. Initially, I used the same composition GUVs as for Complex I but was unable to see recruitment to the GUV surface. Because previous experiments have characterized the relatively weaker membrane affinity of Complex II to Complex I, I reasoned that increasing the fraction of charged lipid headgroups in the GUVs would drive electrostatic interactions with the protein, increasing its recruitment to GUVs. Therefore, I increased the fraction of DOPS from 5% to 20% (50% DOPC, 20% DOPE, 10% DOPI, 20% DOPS, 0.3% ATTO647N DOPE, 0.01% DSPG-PEG2000-biotin), and observed robust recruitment of Complex II to the GUV surface. Upon pulling membrane tubes from GUVs in the presence of Complex II on these GUVs, I found that for initial replicates, Complex II is similarly curvature sensitive to Complex I (Figure 4.2C,D). Nevertheless, additional replicates on membrane tubes of high curvature will be needed to confirm this. Together, these results suggest that in conditions where the proteins bind membranes, both Class III PI3K complexes are potent membrane curvature sensors.

Discussion

The mechanism by which the activity of the two Class III PI3K complexes are directed to their specific membrane substrates during autophagy and endosome trafficking is a key unanswered question in understanding the specific regulation of autophagy initiation relative to other membrane trafficking events in the cell. Here, we set out to develop a more quantitative understanding of the membrane curvature sensitivity of different Class III PI3K complexes to better understand their differential recruitment and regulation in the cell. We found that, consistent with previous reports, Complex I was indeed highly curvature sensitive. Surprisingly,

I also observed in preliminary experiments that Complex II was similarly curvature sensitive, despite not containing the well-characterized curvature sensor ATG14L. While more data is needed to corroborate this finding, it points to a model in which either Complex II contains a complementary membrane curvature sensor, perhaps in UVRAG, or in which other membrane associating regions of both protein complexes act to promote membrane curvature sensitivity.

Future experiments could examine the role that known membrane interacting regions, as well as putative membrane interactors selected through modeling, might play in membrane curvature sensitivity by conducting a rational mutagenesis screen for membrane tube enrichment. Other parameters that could be modulated in this context are the lipid composition and the presence of other PI3K interactors. This method of optically trapped membrane tubes pulled from GUVs is uniquely suited to investigating the differential roles of membrane curvature sensing per se, and high affinity membrane recruitment, and so is primed to provide important missing information about the physiologically relevant regulation of the Class III PI3K complexes. Much has been made of a potential mechanism by which ATG14L could direct Complex I to highly curved autophagy initiation sites or early phagophores through its uniquely curvature sensitive BATS domain, yet this mechanism does not account for the observation that Complex II is similarly curvature sensitive, if more weakly associated with membranes. Instead, it is possible that other regulatory factors such as Rab1 and Rab5 could play a more outsize role in directing the activity of the PI3K complexes in the cell.

Finally, future membrane tube experiments could provide critical functional data to support structural studies into the orientation of PI3K complexes with respect to the membrane surface. Intriguingly, while some biochemical data supports the model that PI3K interacts with the membrane as an "upside down V," there is not yet direct structural evidence to support this. Understanding the molecular pose of the complex with respect to the membrane is crucial to understanding not only the mechanism of catalysis of these kinase complexes, but also how and why they preferentially associate with and act at specific membrane substrates.

Methods

Protein purification
PI3KC3 Complex I and Complex II (composed of constructs in Table 4.2) were purified from suspension HEK cell culture. Cell pellets from 300ml of culture were resuspended in 40 ml of lysis buffer (50mM HEPES pH7.4, 200mM NaCl, 1mM $MnCl_2$, 10% glycerol, 1% Triton X-100, 10mM TCEP, 1x Complete Protease Inhibitor tablet (Roche)), and lysed by rocking at 4˚C for 30 minutes. Lysate was clarified by centrifugation at 35,000 x g for 45 min at 4˚C. The clarified lysate was incubated with 1ml of glutathione Sepharose 4B resin pre-equilibrated in wash buffer (50mM HEPES, pH7.4, 200mM NaCl, 10mM TCEP, 1mM $MnCl_2$) for 4 hours with gentle inversion every 30 minutes. Lysate-bead slurry was applied to a gravity column and washed with 20ml of wash buffer at 4˚C. Protein was eluted from the column with wash buffer containing 50mM reduced glutathione and pH readjusted to 7.4. Eluate was treated with TEV protease overnight at 4˚C, then applied to a Streptactin Sepharose column pre-equilibrated with wash buffer at 4˚C. Column was washed with 20ml of wash buffer, and then protein eluted with wash buffer containing 10mM desthiobiotin. Protein concentration was evaluated by absorbance at 280nm and stored at 4˚C for use within 48 hours.
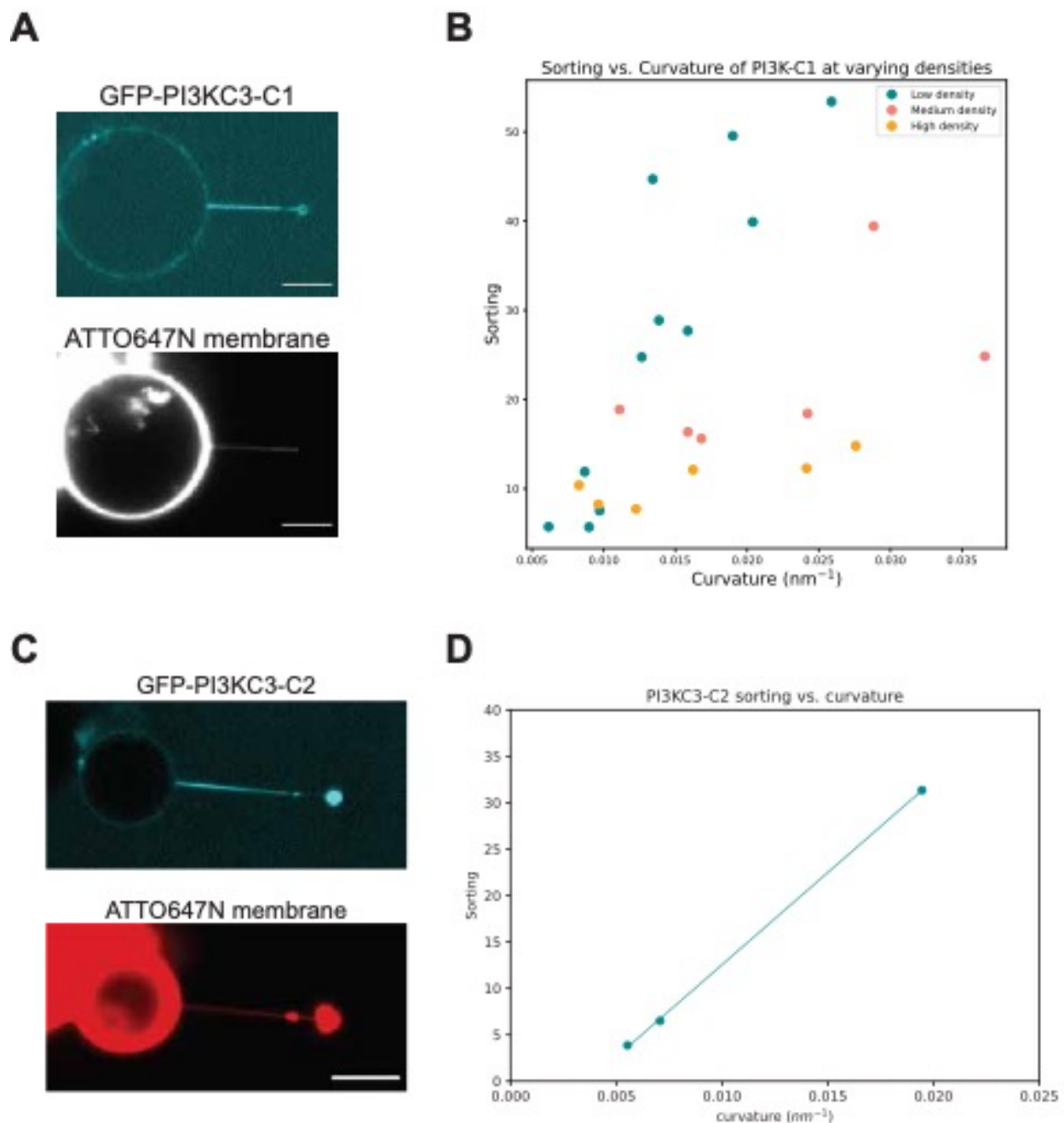
Figure 4.2 Membrane curvature sensitivity of PI3KC3-C1 and PI3KC3-C2
(**A**) Representative confocal fluorescence microscopy image of GFP-labeled PI3KC3-C1 localization (dark cyan) on a membrane tube pulled from a GUV (grey). (**B**) Sorting vs. curvature plot of PI3KC3-C1 enrichment on membrane tubes of varying curvature. Each point represents a single membrane tube. GUVs were binned into 3 classes based on surface density of PI3KC3-C1 on the GUV surface (dark cyan: low density, salmon: medium density, yellow orange: high density). (**C**) Confocal fluorescence microscopy of GFP-labeled PI3KC3-C2 localization (dark cyan) on a membrane tube pulled from a GUV (red). (**D**) Sorting vs. curvature plot of PI3KC3-C2 enrichment on membrane tubes of varying curvature with a linear fit line. Each point represents a single membrane tube.

54

Table 4.2 PI3K Constructs

Complex	Subunit	Construct
C1/C2	VPS34	pCAG-VPS34
C1/C2	VPS15	pCAG-VPS15-2xStrep
C1/C2	BECN1	pCAG-BECN1
C1	ATG14L	pCAG-GST-TEV-GFP-ATG14L
C2	UVRAG	pCAG-GST-TEV-GFP-UVRAG

Membrane tube experiments

GUVs were made in the same method as above. Briefly, 50nmol of lipid was dried into a film on a PVA support and swelled with 100μl of sucrose solution iso-osmotic to the imaging buffer. GUVs were composed of (65% DOPC, 20% DOPE, 10% DOPI, 5% DOPS, 0.3% ATTO647N-DOPE, 0.01% PEG2000-biotin-DSPE) for Complex I experiments or (50% DOPC, 20% DOPE, 10% DOPI, 20% DOPS, 0.3% ATTO647N-DOPE, 0.01% PEG2000-biotin-DSPE) of Complex II experiments. GUVs were mixed with 100nM fluorescently labeled PI3K protein and added to flow cell imaging chambers. Membrane tubes were pulled with optically trapped 1μm streptavidin-coated silica beads. Protein enrichment on membrane tubes was evaluated by segmenting confocal fluorescence images of the membrane tube and GUV surface and quantifying the fluorescence signal across the segmented region. Membrane tube radius was quantified as above by relating the fluorescence intensity of the membrane tube with a scaling factor calculated from a standard curve of membrane tube radii calculated from force measurements from the optical trap (see above).

Chapter 5: Conclusions and outstanding questions

The physical mechanism of autophagosome membrane expansion and shaping is among the most pressing unanswered questions in autophagy research. Because autophagosome biogenesis is fundamentally a membrane remodeling process, understanding how the phagophore membrane is shaped around cargo is central to developing a holistic description of autophagy. However, uncovering how membrane shape contributes to autophagosome biogenesis in the context of a cell is hampered by the complexity of the cellular milieu and the highly networked and redundant interactions of the autophagy initiation machinery. To this end, the work presented here has shown how *in vitro* reconstitution and quantitative biophysical measurements are powerful techniques to directly characterize the interaction between core autophagy proteins and membrane substrates of varied curvature.

Future experiments on membrane curvature sensitivity in autophagy could investigate the curvature sensitivity of other core autophagy proteins. This is a line of inquiry well-suited to a structure-function approach. That is, a screen for mutants that alter the strident membrane curvature of the phagophore rim as observed by cryo-ET would be complemented by *in vitro* reconstitution of mutant proteins on membrane tubes as described here. Such an approach could provide a comprehensive understanding of how multiple curvature sensitive autophagy proteins might be acting together to stabilize the phagophore rim. Follow-up experiments could characterize the mechanism by which curvature stabilizing proteins dissociate from the phagophore rim at later stages of phagophore expansion. Finally, it would be interesting to investigate what role membrane curvature plays in the recruitment of ESCRT proteins specifically to sites of phagophore closure.

References

Abraham, M. J., Murtola, T., Schulz, R., Páll, S., Smith, J. C., Hess, B., & Lindahl, E. (2015). GROMACS: High performance molecular simulations through multi-level parallelism from laptops to supercomputers. *SoftwareX*, *1-2*, 19-25. https://doi.org/10.1016/j.softx.2015.06.001

Agudo-Canalejo, J., Schultz, S. W., Chino, H., Migliano, S. M., Saito, C., Koyama-Honda, I., Stenmark, H., Brech, A., May, A. I., Mizushima, N., & Knorr, R. L. (2021). Wetting regulates autophagy of phase-separated compartments and the cytosol. *Nature*, *591*(7848), 142-146. https://doi.org/10.1038/s41586-020-2992-3

Ambroggio, E., Sorre, B., Bassereau, P., Goud, B., Manneville, J. B., & Antonny, B. (2010). ArfGAP1 generates an Arf1 gradient on continuous lipid membranes displaying flat and curved regions. *EMBO J*, *29*(2), 292-303. https://doi.org/10.1038/emboj.2009.341

Bahrami, A. H., Lin, M. G., Ren, X., Hurley, J. H., & Hummer, G. (2017). Scaffolding the cup-shaped double membrane in autophagy. *PLoS Comput Biol*, *13*(10), e1005817. https://doi.org/10.1371/journal.pcbi.1005817

Baskaran, S., Carlson, L. A., Stjepanovic, G., Young, L. N., Kim, D. J., Grob, P., Stanley, R. E., Nogales, E., & Hurley, J. H. (2014). Architecture and dynamics of the autophagic phosphatidylinositol 3-kinase complex. *Elife*, *3*. https://doi.org/10.7554/eLife.05115

Baskaran, S., Ragusa, M. J., Boura, E., & Hurley, J. H. (2012). Two-site recognition of phosphatidylinositol 3-phosphate by PROPPINs in autophagy. *Mol Cell*, *47*(3), 339-348. https://doi.org/10.1016/j.molcel.2012.05.027

Bhaskara, R. M., Grumati, P., Garcia-Pardo, J., Kalayil, S., Covarrubias-Pinto, A., Chen, W., Kudryashev, M., Dikic, I., & Hummer, G. (2019). Curvature induction and membrane remodeling by FAM134B reticulon homology domain assist selective ER-phagy. *Nat Commun*, *10*(1), 2370. https://doi.org/10.1038/s41467-019-10345-3

Bieber, A., Capitanio, C., Erdmann, P. S., Fiedler, F., Beck, F., Lee, C. W., Li, D., Hummer, G., Schulman, B. A., Baumeister, W., & Wilfling, F. (2022). In situ structural analysis reveals membrane shape transitions during autophagosome formation. *Proc Natl Acad Sci U S A*, *119*(39), e2209823119. https://doi.org/10.1073/pnas.2209823119

Bigay, J., Casella, J. F., Drin, G., Mesmin, B., & Antonny, B. (2005). ArfGAP1 responds to membrane curvature through the folding of a lipid packing sensor motif. *EMBO J*, *24*(13), 2244-2253. https://doi.org/10.1038/sj.emboj.7600714

Birgisdottir, A. B., Mouilleron, S., Bhujabal, Z., Wirth, M., Sjottem, E., Evjen, G., Zhang, W., Lee, R., O'Reilly, N., Tooze, S. A., Lamark, T., & Johansen, T. (2019). Members of the autophagy class III phosphatidylinositol 3-kinase complex I interact with GABARAP and GABARAPL1 via LIR motifs. *Autophagy*, *15*(8), 1333-1355. https://doi.org/10.1080/15548627.2019.1581009

Brier, L. W., Ge, L., Stjepanovic, G., Thelen, A. M., Hurley, J. H., & Schekman, R. (2019). Regulation of LC3 lipidation by the autophagy-specific class III phosphatidylinositol-3 kinase complex. *Mol Biol Cell*, *30*(9), 1098-1107. https://doi.org/10.1091/mbc.E18-11-0743

Busch, D. J., Houser, J. R., Hayden, C. C., Sherman, M. B., Lafer, E. M., & Stachowiak, J. C. (2015). Intrinsically disordered proteins drive membrane curvature. *Nat Commun*, *6*, 7875. https://doi.org/10.1038/ncomms8875

Busse, R. A., Scacioc, A., Krick, R., Perez-Lara, A., Thumm, M., & Kuhnel, K. (2015). Characterization of PROPPIN-Phosphoinositide Binding and Role of Loop 6CD in PROPPIN-Membrane Binding. *Biophys J*, *108*(9), 2223-2234. https://doi.org/10.1016/j.bpj.2015.03.045

Bussi, G., Donadio, D., & Parrinello, M. (2007). Canonical sampling through velocity rescaling. *J Chem Phys*, *126*(1), 014101. https://doi.org/10.1063/1.2408420

Cada, A. K., Pavlin, M. R., Castillo, J. P., Tong, A. B., Larsen, K. P., Ren, X., Yokom, A., Tsai, F.-C., Shiah, J., Bassereau, P. M., Bustamante, C. J., & Hurley, J. H. (2022). Reconstitution reveals friction-driven membrane scission by the human ESCRT-III proteins CHMP1B and IST1. *bioRxiv*. https://doi.org/10.1101/2022.02.03.479062

Cail, R. C., & Drubin, D. G. (2023). Membrane curvature as a signal to ensure robustness of diverse cellular processes. *Trends Cell Biol*, *33*(5), 427-441. https://doi.org/10.1016/j.tcb.2022.09.004

Campelo, F., McMahon, H. T., & Kozlov, M. M. (2008). The hydrophobic insertion mechanism of membrane curvature generation by proteins. *Biophys J*, *95*(5), 2325-2339. https://doi.org/10.1529/biophysj.108.133173

Canham, P. B. (1970). The minimum energy of bending as a possible explanation of the biconcave shape of the human red blood cell. *J Theor Biol*, *26*(1), 61-81. https://doi.org/10.1016/s0022-5193(70)80032-7

Chang, C., Jensen, L. E., & Hurley, J. H. (2021). Autophagosome biogenesis comes out of the black box. *Nat Cell Biol*, *23*(5), 450-456. https://doi.org/10.1038/s41556-021-00669-y

Chang, C., Shi, X., Jensen, L. E., Yokom, A. L., Fracchiolla, D., Martens, S., & Hurley, J. H. (2021). Reconstitution of cargo-induced LC3 lipidation in mammalian selective autophagy. *Sci Adv*, *7*(17). https://doi.org/10.1126/sciadv.abg4922

Chang, C., Young, L. N., Morris, K. L., von Bulow, S., Schoneberg, J., Yamamoto-Imoto, H., Oe, Y., Yamamoto, K., Nakamura, S., Stjepanovic, G., Hummer, G., Yoshimori, T., & Hurley, J. H. (2019). Bidirectional Control of Autophagy by BECN1 BARA Domain Dynamics. *Mol Cell*, *73*(2), 339-353 e336. https://doi.org/10.1016/j.molcel.2018.10.035

Chen, M., Ren, X., Cook, A. S. I., & Hurley, J. H. (2023). *bioRxiv*. https://doi.org/10.1101/2023.06.01.543278

Chowdhury, S., Otomo, C., Leitner, A., Ohashi, K., Aebersold, R., Lander, G. C., & Otomo, T. (2018). Insights into autophagosome biogenesis from structural and biochemical analyses of the ATG2A-WIPI4 complex. *Proceedings of the National Academy of Sciences of the United States of America*, *115*(42), E9792-E9801. https://doi.org/10.1073/pnas.1811874115

Christoforidis, S., Miaczynska, M., Ashman, K., Wilm, M., Zhao, L., Yip, S. C., Waterfield, M. D., Backer, J. M., & Zerial, M. (1999). Phosphatidylinositol-3-OH kinases are Rab5 effectors. *Nat Cell Biol*, *1*(4), 249-252. https://doi.org/10.1038/12075

Cui, H., Lyman, E., & Voth, G. A. (2011). Mechanism of membrane curvature sensing by amphipathic helix containing proteins. *Biophys J*, *100*(5), 1271-1279. https://doi.org/10.1016/j.bpj.2011.01.036

Cuvelier, D., Derenyi, I., Bassereau, P., & Nassoy, P. (2005). Coalescence of membrane tethers: experiments, theory, and applications. *Biophysical Journal*, *88*(4), 2714-2726. https://doi.org/DOI 10.1529/biophysj.104.056473

Dai, J., & Sheetz, M. P. (1995). Mechanical properties of neuronal growth cone membranes studied by tether formation with laser optical tweezers. *Biophys J*, *68*(3), 988-996. https://doi.org/10.1016/S0006-3495(95)80274-2

Dar, S., Kamerkar, S. C., & Pucadyil, T. J. (2015). A high-throughput platform for real-time analysis of membrane fission reactions reveals dynamin function. *Nat Cell Biol*, *17*(12), 1588-1596. https://doi.org/10.1038/ncb3254

Dar, S., Kamerkar, S. C., & Pucadyil, T. J. (2017). Use of the supported membrane tube assay system for real-time analysis of membrane fission reactions. *Nat Protoc*, *12*(2), 390-400. https://doi.org/10.1038/nprot.2016.173

Darden, T., York, D., & Pedersen, L. (1993). Particle mesh Ewald: AnN·log(N) method for Ewald sums in large systems. *The Journal of Chemical Physics*, *98*(12), 10089-10092. https://doi.org/10.1063/1.464397

Delano, W. L. (2002). PyMOL: An open-source molecular graphics tool. *CCP4 Newsletter On Protein Crystallography*, *40*, 82-92.

Deserno, M. (2007). Fluid lipid membranes – a primer. https://www.cmu.edu/biolphys/deserno/pdf/membrane_theory.pdf

Deserno, M. (2015). Fluid lipid membranes: from differential geometry to curvature stresses. *Chem Phys Lipids*, *185*, 11-45. https://doi.org/10.1016/j.chemphyslip.2014.05.001

Dooley, H. C., Razi, M., Polson, H. E., Girardin, S. E., Wilson, M. I., & Tooze, S. A. (2014). WIPI2 links LC3 conjugation with PI3P, autophagosome formation, and pathogen clearance by recruiting Atg12-5-16L1. *Mol Cell*, *55*(2), 238-252. https://doi.org/10.1016/j.molcel.2014.05.021

Dove, S. K., Piper, R. C., McEwen, R. K., Yu, J. W., King, M. C., Hughes, D. C., Thuring, J., Holmes, A. B., Cooke, F. T., Michell, R. H., Parker, P. J., & Lemmon, M. A. (2004). Svp1p defines a family of phosphatidylinositol 3,5-bisphosphate effectors. *EMBO J*, *23*(9), 1922-1933. https://doi.org/10.1038/sj.emboj.7600203

Drin, G., & Antonny, B. (2010). Amphipathic helices and membrane curvature. *FEBS Lett*, *584*(9), 1840-1847. https://doi.org/10.1016/j.febslet.2009.10.022

Drin, G., Casella, J. F., Gautier, R., Boehmer, T., Schwartz, T. U., & Antonny, B. (2007). A general amphipathic alpha-helical motif for sensing membrane curvature. *Nat Struct Mol Biol*, *14*(2), 138-146. https://doi.org/10.1038/nsmb1194

Drozdetskiy, A., Cole, C., Procter, J., & Barton, G. J. (2015). JPred4: a protein secondary structure prediction server. *Nucleic Acids Res*, *43*(W1), W389-394. https://doi.org/10.1093/nar/gkv332

Durrant, J. D., & Amaro, R. E. (2014). LipidWrapper: an algorithm for generating large-scale membrane models of arbitrary geometry. *PLoS Comput Biol*, *10*(7), e1003720. https://doi.org/10.1371/journal.pcbi.1003720

Essmann, U., Perera, L., Berkowitz, M. L., Darden, T., Lee, H., & Pedersen, L. G. (1995). A smooth particle mesh Ewald method. *The Journal of Chemical Physics*, *103*(19), 8577-8593. https://doi.org/10.1063/1.470117

Evans, E., & Needham, D. (1987). Physical-Properties of Surfactant Bilayer-Membranes - Thermal Transitions, Elasticity, Rigidity, Cohesion, and Colloidal Interactions. *Journal of Physical Chemistry*, *91*(16), 4219-4228. https://doi.org/DOI 10.1021/j100300a003

Fan, W., Nassiri, A., & Zhong, Q. (2011). Autophagosome targeting and membrane curvature sensing by Barkor/Atg14(L). *Proc Natl Acad Sci U S A*, *108*(19), 7769-7774. https://doi.org/10.1073/pnas.1016472108

Fracchiolla, D., Chang, C., Hurley, J. H., & Martens, S. (2020). A PI3K-WIPI2 positive feedback loop allosterically activates LC3 lipidation in autophagy. *J Cell Biol*, *219*(7). https://doi.org/10.1083/jcb.201912098

Gautier, R., Douguet, D., Antonny, B., & Drin, G. (2008). HELIQUEST: a web server to screen sequences with specific alpha-helical properties. *Bioinformatics*, *24*(18), 2101-2102. https://doi.org/10.1093/bioinformatics/btn392

Gopaldass, N., Fauvet, B., Lashuel, H., Roux, A., & Mayer, A. (2017). Membrane scission driven by the PROPPIN Atg18. *EMBO J*, *36*(22), 3274-3291. https://doi.org/10.15252/embj.201796859

Gowers, R. J., Linke, M., Barnoud, J., Reddy, T. J. E., Melo, M. N., Seyler, S. L., Domański, J., Dotson, D. L., Buchoux, S., Kenney, I. M., & Beckstein, O. (2016). MDAnalysis: A Python Package for the Rapid Analysis

of Molecular Dynamics Simulations. *Proc. of the 15th Python in Science Conf. (SciPy 2016)*, 98-105.

Hayashi-Nishino, M., Fujita, N., Noda, T., Yamaguchi, A., Yoshimori, T., & Yamamoto, A. (2009). A subdomain of the endoplasmic reticulum forms a cradle for autophagosome formation. *Nat Cell Biol*, *11*(12), 1433-1437. https://doi.org/10.1038/ncb1991

Heinrich, M., Tian, A., Esposito, C., & Baumgart, T. (2010). Dynamic sorting of lipids and proteins in membrane tubes with a moving phase boundary. *Proc Natl Acad Sci U S A*, *107*(16), 7208-7213. https://doi.org/10.1073/pnas.0913997107

Heinrich, V., & Waugh, R. E. (1996). A piconewton force transducer and its application to measurement of the bending stiffness of phospholipid membranes. *Ann Biomed Eng*, *24*(5), 595-605. https://doi.org/10.1007/BF02684228

Helfrich, W. (1973). Elastic properties of lipid bilayers: theory and possible experiments. *Z Naturforsch C*, *28*(11), 693-703. https://doi.org/10.1515/znc-1973-11-1209

Herman, P. K., Stack, J. H., & Emr, S. D. (1991). A genetic and structural analysis of the yeast Vps15 protein kinase: evidence for a direct role of Vps15p in vacuolar protein delivery. *EMBO J*, *10*(13), 4049-4060. https://doi.org/10.1002/j.1460-2075.1991.tb04981.x

Hess, B., Bekker, H., Berendsen, H. J. C., & Fraaije, J. G. E. M. (1997). LINCS: A linear constraint solver for molecular simulations. *Journal of Computational Chemistry*, *18*(12), 1463-1472. https://doi.org/10.1002/(sici)1096-987x(199709)18:12<1463::Aid-jcc4>3.0.Co;2-h

Hooy, R. M., Iwamoto, Y., Tudorica, D. A., Ren, X., & Hurley, J. H. (2022). Self-assembly and structure of a clathrin-independent AP-1:Arf1 tubular membrane coat. *Sci Adv*, *8*(42), eadd3914. https://doi.org/10.1126/sciadv.add3914

Huang, J., Rauscher, S., Nawrocki, G., Ran, T., Feig, M., de Groot, B. L., Grubmuller, H., & MacKerell, A. D., Jr. (2017). CHARMM36m: an improved force field for folded and intrinsically disordered proteins. *Nat Methods*, *14*(1), 71-73. https://doi.org/10.1038/nmeth.4067

Huang, W., Choi, W., Hu, W., Mi, N., Guo, Q., Ma, M., Liu, M., Tian, Y., Lu, P., Wang, F. L., Deng, H., Liu, L., Gao, N., Yu, L., & Shi, Y. (2012). Crystal structure and biochemical analyses reveal Beclin 1 as a novel membrane binding protein. *Cell Res*, *22*(3), 473-489. https://doi.org/10.1038/cr.2012.24

Ichimura, Y., Imamura, Y., Emoto, K., Umeda, M., Noda, T., & Ohsumi, Y. (2004). In vivo and in vitro reconstitution of Atg8 conjugation essential for autophagy. *J Biol Chem*, *279*(39), 40584-40592. https://doi.org/10.1074/jbc.M405860200

Johansen, T., & Lamark, T. (2020). Selective Autophagy: ATG8 Family Proteins, LIR Motifs and Cargo Receptors. *J Mol Biol*, *432*(1), 80-103. https://doi.org/10.1016/j.jmb.2019.07.016

Jumper, J., Evans, R., Pritzel, A., Green, T., Figurnov, M., Ronneberger, O., Tunyasuvunakool, K., Bates, R., Zidek, A., Potapenko, A., Bridgland, A., Meyer, C., Kohl, S. A. A., Ballard, A. J., Cowie, A., Romera-Paredes, B., Nikolov, S., Jain, R., Adler, J., . . . Hassabis, D. (2021). Highly accurate protein structure prediction with AlphaFold. *Nature*, *596*(7873), 583-589. https://doi.org/10.1038/s41586-021-03819-2

Kaufmann, A., Beier, V., Franquelim, H. G., & Wollert, T. (2014). Molecular mechanism of autophagic membrane-scaffold assembly and disassembly. *Cell*, *156*(3), 469-481. https://doi.org/10.1016/j.cell.2013.12.022

Kim, J. H., Hong, S. B., Lee, J. K., Han, S., Roh, K. H., Lee, K. E., Kim, Y. K., Choi, E. J., & Song, H. K. (2015). Insights into autophagosome maturation revealed by the structures of ATG5 with its interacting partners. *Autophagy*, *11*(1), 75-87. https://doi.org/10.4161/15548627.2014.984276

Klionsky, D. J., Petroni, G., Amaravadi, R. K., Baehrecke, E. H., Ballabio, A., Boya, P., Bravo-San Pedro, J. M., Cadwell, K., Cecconi, F., Choi, A. M. K., Choi, M. E., Chu, C. T., Codogno, P., Colombo, M. I., Cuervo, A. M., Deretic, V., Dikic, I., Elazar, Z., Eskelinen, E. L., . . . Pietrocola, F. (2021). Autophagy in major human diseases. *EMBO J*, *40*(19), e108863. https://doi.org/10.15252/embj.2021108863

Knorr, R. L., Dimova, R., & Lipowsky, R. (2012). Curvature of double-membrane organelles generated by changes in membrane size and composition. *PLoS One*, *7*(3), e32753. https://doi.org/10.1371/journal.pone.0032753

Krick, R., Busse, R. A., Scacioc, A., Stephan, M., Janshoff, A., Thumm, M., & Kuhnel, K. (2012). Structural and functional characterization of the two phosphoinositide binding sites of PROPPINs, a beta-propeller protein family. *Proc Natl Acad Sci U S A*, *109*(30), E2042-2049. https://doi.org/10.1073/pnas.1205128109

Le Bars, R., Marion, J., Le Borgne, R., Satiat-Jeunemaitre, B., & Bianchi, M. W. (2014). ATG5 defines a phagophore domain connected to the endoplasmic reticulum during autophagosome formation in plants. *Nat Commun*, *5*, 4121. https://doi.org/10.1038/ncomms5121

Li, L., Tong, M., Fu, Y., Chen, F., Zhang, S., Chen, H., Ma, X., Li, D., Liu, X., & Zhong, Q. (2021). Lipids and membrane-associated proteins in autophagy. *Protein Cell*, *12*(7), 520-544. https://doi.org/10.1007/s13238-020-00793-9

Liang, R., Ren, J., Zhang, Y., & Feng, W. (2019). Structural Conservation of the Two Phosphoinositide-Binding Sites in WIPI Proteins. *J Mol Biol*, *431*(7), 1494-1505. https://doi.org/10.1016/j.jmb.2019.02.019

Lystad, A. H., Carlsson, S. R., de la Ballina, L. R., Kauffman, K. J., Nag, S., Yoshimori, T., Melia, T. J., & Simonsen, A. (2019). Distinct functions of ATG16L1 isoforms in membrane binding and LC3B lipidation in autophagy-related processes. *Nat Cell Biol*, *21*(3), 372-383. https://doi.org/10.1038/s41556-019-0274-9

MacDonald, R. C., MacDonald, R. I., Menco, B. P., Takeshita, K., Subbarao, N. K., & Hu, L. R. (1991). Small-volume extrusion apparatus for preparation of large, unilamellar vesicles. *Biochim Biophys Acta*, *1061*(2), 297-303. https://doi.org/10.1016/0005-2736(91)90295-j

Maeda, S., Otomo, C., & Otomo, T. (2019). The autophagic membrane tether ATG2A transfers lipids between membranes. *Elife*, *8*. https://doi.org/10.7554/eLife.45777

Maeda, S., Yamamoto, H., Kinch, L. N., Garza, C. M., Takahashi, S., Otomo, C., Grishin, N. V., Forli, S., Mizushima, N., & Otomo, T. (2020). Structure, lipid scrambling activity and role in autophagosome formation of ATG9A. *Nat Struct Mol Biol*, *27*(12), 1194-1201. https://doi.org/10.1038/s41594-020-00520-2

Matoba, K., Kotani, T., Tsutsumi, A., Tsuji, T., Mori, T., Noshiro, D., Sugita, Y., Nomura, N., Iwata, S., Ohsumi, Y., Fujimoto, T., Nakatogawa, H., Kikkawa, M., & Noda, N. N. (2020). Atg9 is a lipid scramblase that mediates autophagosomal membrane expansion. *Nat Struct Mol Biol*, *27*(12), 1185-1193. https://doi.org/10.1038/s41594-020-00518-w

Melia, T. J., Lystad, A. H., & Simonsen, A. (2020). Autophagosome biogenesis: From membrane growth to closure. *J Cell Biol*, *219*(6). https://doi.org/10.1083/jcb.202002085

Mesmin, B., Drin, G., Levi, S., Rawet, M., Cassel, D., Bigay, J., & Antonny, B. (2007). Two lipid-packing sensor motifs contribute to the sensitivity of ArfGAP1 to membrane curvature. *Biochemistry*, *46*(7), 1779-1790. https://doi.org/10.1021/bi062288w

Metlagel, Z., Otomo, C., Ohashi, K., Takaesu, G., & Otomo, T. (2014). Structural insights into E2-E3 interaction for LC3 lipidation. *Autophagy*, *10*(3), 522-523. https://doi.org/10.4161/auto.27594

Michaud-Agrawal, N., Denning, E. J., Woolf, T. B., & Beckstein, O. (2011). MDAnalysis: a toolkit for the analysis of molecular dynamics simulations. *J Comput Chem*, *32*(10), 2319-2327. https://doi.org/10.1002/jcc.21787

Miller, S., Tavshanjian, B., Oleksy, A., Perisic, O., Houseman, B. T., Shokat, K. M., & Williams, R. L. (2010). Shaping development of autophagy inhibitors with the structure of the lipid kinase Vps34. *Science*, *327*(5973), 1638-1642. https://doi.org/10.1126/science.1184429

Mizushima, N., Yamamoto, A., Hatano, M., Kobayashi, Y., Kabeya, Y., Suzuki, K., Tokuhisa, T., Ohsumi, Y., & Yoshimori, T. (2001). Dissection of autophagosome formation using Apg5-deficient mouse embryonic stem cells. *J Cell Biol*, *152*(4), 657-668. https://doi.org/10.1083/jcb.152.4.657

Mizushima, N., Yoshimori, T., & Ohsumi, Y. (2011). The role of Atg proteins in autophagosome formation. *Annu Rev Cell Dev Biol*, *27*, 107-132. https://doi.org/10.1146/annurev-cellbio-092910-154005

Nakatogawa, H. (2020). Mechanisms governing autophagosome biogenesis. *Nat Rev Mol Cell Biol*, *21*(8), 439-458. https://doi.org/10.1038/s41580-020-0241-0

Nath, S., Dancourt, J., Shteyn, V., Puente, G., Fong, W. M., Nag, S., Bewersdorf, J., Yamamoto, A., Antonny, B., & Melia, T. J. (2014). Lipidation of the LC3/GABARAP family of autophagy proteins relies on a membrane-curvature-sensing domain in Atg3. *Nat Cell Biol*, *16*(5), 415-424. https://doi.org/10.1038/ncb2940

Nguyen, N., Shteyn, V., & Melia, T. J. (2017). Sensing Membrane Curvature in Macroautophagy. *J Mol Biol*, *429*(4), 457-472. https://doi.org/10.1016/j.jmb.2017.01.006

Nguyen, T. N., Padman, B. S., Usher, J., Oorschot, V., Ramm, G., & Lazarou, M. (2016). Atg8 family LC3/GABARAP proteins are crucial for autophagosome-lysosome fusion but not autophagosome formation during PINK1/Parkin mitophagy and starvation. *J Cell Biol*, *215*(6), 857-874. https://doi.org/10.1083/jcb.201607039

Ohashi, Y., Tremel, S., Masson, G. R., McGinney, L., Boulanger, J., Rostislavleva, K., Johnson, C. M., Niewczas, I., Clark, J., & Williams, R. L. (2020). Membrane characteristics tune activities of endosomal and autophagic human VPS34 complexes. *Elife*, *9*. https://doi.org/10.7554/eLife.58281

Osawa, T., Kotani, T., Kawaoka, T., Hirata, E., Suzuki, K., Nakatogawa, H., Ohsumi, Y., & Noda, N. N. (2019). Atg2 mediates direct lipid transfer between membranes for autophagosome formation. *Nature Structural & Molecular Biology*, *26*(4), 281-+. https://doi.org/10.1038/s41594-019-0203-4

Otomo, C., Metlagel, Z., Takaesu, G., & Otomo, T. (2013). Structure of the human ATG12~ATG5 conjugate required for LC3 lipidation in autophagy. *Nat Struct Mol Biol*, *20*(1), 59-66. https://doi.org/10.1038/nsmb.2431

Park, D., Wu, Y., Wang, X., Gowrishankar, S., Baublis, A., & De Camilli, P. (2023). Synaptic vesicle proteins and ATG9A self-organize in distinct vesicle phases within synapsin condensates. *Nat Commun*, *14*(1), 455. https://doi.org/10.1038/s41467-023-36081-3

Parrinello, M., & Rahman, A. (1981). Polymorphic transitions in single crystals: A new molecular dynamics method. *Journal of Applied Physics*, *52*(12), 7182-7190. https://doi.org/10.1063/1.328693

Pickrell, A. M., & Youle, R. J. (2015). The roles of PINK1, parkin, and mitochondrial fidelity in Parkinson's disease. *Neuron*, *85*(2), 257-273. https://doi.org/10.1016/j.neuron.2014.12.007

Poma, A. B., Cieplak, M., & Theodorakis, P. E. (2017). Combining the MARTINI and Structure-Based Coarse-Grained Approaches for the Molecular Dynamics Studies of Conformational Transitions in Proteins. *J Chem Theory Comput*, *13*(3), 1366-1374. https://doi.org/10.1021/acs.jctc.6b00986

Prevost, C., Tsai, F. C., Bassereau, P., & Simunovic, M. (2017). Pulling Membrane Nanotubes from Giant Unilamellar Vesicles. *J Vis Exp*(130). https://doi.org/10.3791/56086

Prevost, C., Zhao, H., Manzi, J., Lemichez, E., Lappalainen, P., Callan-Jones, A., & Bassereau, P. (2015). IRSp53 senses negative membrane curvature and phase separates along membrane tubules. *Nat Commun*, *6*, 8529. https://doi.org/10.1038/ncomms9529

Ragusa, M. J., Stanley, R. E., & Hurley, J. H. (2012). Architecture of the Atg17 complex as a scaffold for autophagosome biogenesis. *Cell*, *151*(7), 1501-1512. https://doi.org/10.1016/j.cell.2012.11.028

Renard, H. F., Simunovic, M., Lemiere, J., Boucrot, E., Garcia-Castillo, M. D., Arumugam, S., Chambon, V., Lamaze, C., Wunder, C., Kenworthy, A. K., Schmidt, A. A., McMahon, H. T., Sykes, C., Bassereau, P., & Johannes, L. (2015). Endophilin-A2 functions in membrane scission in clathrin-independent endocytosis. *Nature*, *517*(7535), 493-496. https://doi.org/10.1038/nature14064

Rogov, V., Dotsch, V., Johansen, T., & Kirkin, V. (2014). Interactions between autophagy receptors and ubiquitin-like proteins form the molecular basis for selective autophagy. *Mol Cell*, *53*(2), 167-178. https://doi.org/10.1016/j.molcel.2013.12.014

Romanov, J., Walczak, M., Ibiricu, I., Schuchner, S., Ogris, E., Kraft, C., & Martens, S. (2012). Mechanism and functions of membrane binding by the Atg5-Atg12/Atg16 complex during autophagosome formation. *EMBO J*, *31*(22), 4304-4317. https://doi.org/10.1038/emboj.2012.278

Rostislavleva, K., Soler, N., Ohashi, Y., Zhang, L., Pardon, E., Burke, J. E., Masson, G. R., Johnson, C., Steyaert, J., Ktistakis, N. T., & Williams, R. L. (2015). Structure and flexibility of the endosomal Vps34 complex reveals the basis of its function on membranes. *Science*, *350*(6257), aac7365. https://doi.org/10.1126/science.aac7365

Roux, A., Cuvelier, D., Nassoy, P., Prost, J., Bassereau, P., & Goud, B. (2005). Role of curvature and phase transition in lipid sorting and fission of membrane tubules. *EMBO J*, *24*(8), 1537-1545. https://doi.org/10.1038/sj.emboj.7600631

Sakai, Y., Koyama-Honda, I., Tachikawa, M., Knorr, R. L., & Mizushima, N. (2020). Modeling Membrane Morphological Change during Autophagosome Formation. *iScience*, *23*(9), 101466. https://doi.org/10.1016/j.isci.2020.101466

Sawa-Makarska, J., Baumann, V., Coudevylle, N., von Bulow, S., Nogellova, V., Abert, C., Schuschnig, M., Graef, M., Hummer, G., & Martens, S. (2020). Reconstitution of autophagosome nucleation defines Atg9 vesicles as seeds for membrane formation. *Science*, *369*(6508), 1206-+. https://doi.org/10.1126/science.aaz7714

Schoneberg, J., Pavlin, M. R., Yan, S., Righini, M., Lee, I. H., Carlson, L. A., Bahrami, A. H., Goldman, D. H., Ren, X., Hummer, G., Bustamante, C., & Hurley, J. H. (2018). ATP-dependent force generation and membrane scission by ESCRT-III and Vps4. *Science*, *362*(6421), 1423-1428. https://doi.org/10.1126/science.aat1839

Schutter, M., Giavalisco, P., Brodesser, S., & Graef, M. (2020). Local Fatty Acid Channeling into Phospholipid Synthesis Drives Phagophore Expansion during Autophagy. *Cell*, *180*(1), 135-+. https://doi.org/10.1016/j.cell.2019.12.005

Simunovic, M., Prevost, C., Callan-Jones, A., & Bassereau, P. (2016). Physical basis of some membrane shaping mechanisms. *Philos Trans A Math Phys Eng Sci*, *374*(2072). https://doi.org/10.1098/rsta.2016.0034

Snead, W. T., & Stachowiak, J. C. (2018). Structure Versus Stochasticity-The Role of Molecular Crowding and Intrinsic Disorder in Membrane Fission. *J Mol Biol*, *430*(16), 2293-2308. https://doi.org/10.1016/j.jmb.2018.03.024

Sorre, B., Callan-Jones, A., Manneville, J. B., Nassoy, P., Joanny, J. F., Prost, J., Goud, B., & Bassereau, P. (2009). Curvature-driven lipid sorting needs proximity to a demixing point and is aided by proteins. *Proc Natl Acad Sci U S A*, *106*(14), 5622-5626. https://doi.org/10.1073/pnas.0811243106

Sorre, B., Callan-Jones, A., Manzi, J., Goud, B., Prost, J., Bassereau, P., & Roux, A. (2012). Nature of curvature coupling of amphiphysin with membranes depends on its bound density. *Proc Natl Acad Sci U S A*, *109*(1), 173-178. https://doi.org/10.1073/pnas.1103594108

Souza, P. C. T., Alessandri, R., Barnoud, J., Thallmair, S., Faustino, I., Grunewald, F., Patmanidis, I., Abdizadeh, H., Bruininks, B. M. H., Wassenaar, T. A., Kroon, P. C., Melcr, J., Nieto, V., Corradi, V., Khan, H. M., Domanski, J., Javanainen, M., Martinez-Seara, H., Reuter, N., . . . Marrink, S. J. (2021). Martini 3: a general purpose force field for coarse-grained molecular dynamics. *Nat Methods*, *18*(4), 382-388. https://doi.org/10.1038/s41592-021-01098-3

Strong, L. M., Chang, C., Riley, J. F., Boecker, C. A., Flower, T. G., Buffalo, C. Z., Ren, X., Stavoe, A. K., Holzbaur, E. L., & Hurley, J. H. (2021). Structural basis for membrane recruitment of ATG16L1 by WIPI2 in autophagy. *Elife*, *10*. https://doi.org/10.7554/eLife.70372

Tremel, S., Ohashi, Y., Morado, D. R., Bertram, J., Perisic, O., Brandt, L. T. L., von Wrisberg, M. K., Chen, Z. A., Maslen, S. L., Kovtun, O., Skehel, M., Rappsilber, J., Lang, K., Munro, S., Briggs, J. A. G., & Williams, R. L. (2021). Structural basis for VPS34 kinase activation by Rab1 and Rab5 on membranes. *Nat Commun*, *12*(1), 1564. https://doi.org/10.1038/s41467-021-21695-2

Vamparys, L., Gautier, R., Vanni, S., Bennett, W. F., Tieleman, D. P., Antonny, B., Etchebest, C., & Fuchs, P. F. (2013). Conical lipids in flat bilayers induce packing defects similar to that induced by positive curvature. *Biophys J*, *104*(3), 585-593. https://doi.org/10.1016/j.bpj.2012.11.3836

Vanni, S., Hirose, H., Barelli, H., Antonny, B., & Gautier, R. (2014). A sub-nanometre view of how membrane curvature and composition modulate lipid packing and protein recruitment. *Nat Commun*, *5*, 4916. https://doi.org/10.1038/ncomms5916

Vanni, S., Vamparys, L., Gautier, R., Drin, G., Etchebest, C., Fuchs, P. F., & Antonny, B. (2013). Amphipathic lipid packing sensor motifs: probing bilayer defects with hydrophobic residues. *Biophys J*, *104*(3), 575-584. https://doi.org/10.1016/j.bpj.2012.11.3837

Varadi, M., Anyango, S., Deshpande, M., Nair, S., Natassia, C., Yordanova, G., Yuan, D., Stroe, O., Wood, G., Laydon, A., Zidek, A., Green, T., Tunyasuvunakool, K., Petersen, S., Jumper, J., Clancy, E., Green, R., Vora, A., Lutfi, M., . . . Velankar, S. (2022). AlphaFold Protein Structure Database: massively expanding the structural coverage of protein-sequence space with high-accuracy models. *Nucleic Acids Res*, *50*(D1), D439-D444. https://doi.org/10.1093/nar/gkab1061

Vickery, O. N., & Stansfeld, P. J. (2021). CG2AT2: an Enhanced Fragment-Based Approach for Serial Multi-scale Molecular Dynamics Simulations. *J Chem Theory Comput*, *17*(10), 6472-6482. https://doi.org/10.1021/acs.jctc.1c00295

von Bülow, S., & Hummer, G. (2020). Kinetics of Atg2-mediated lipid transfer from the ER can account for phagophore expansion. *bioRxiv*. https://doi.org/10.1101/2020.05.12.090977

Wassenaar, T. A., Ingolfsson, H. I., Bockmann, R. A., Tieleman, D. P., & Marrink, S. J. (2015). Computational Lipidomics with insane: A Versatile Tool for Generating Custom Membranes for Molecular Simulations. *J Chem Theory Comput*, *11*(5), 2144-2155. https://doi.org/10.1021/acs.jctc.5b00209

Watanabe, Y., Kobayashi, T., Yamamoto, H., Hoshida, H., Akada, R., Inagaki, F., Ohsumi, Y., & Noda, N. N. (2012). Structure-based analyses reveal distinct binding sites for Atg2 and phosphoinositides in Atg18. *J Biol Chem*, *287*(38), 31681-31690. https://doi.org/10.1074/jbc.M112.397570

Waterhouse, A., Bertoni, M., Bienert, S., Studer, G., Tauriello, G., Gumienny, R., Heer, F. T., de Beer, T. A. P., Rempfer, C., Bordoli, L., Lepore, R., & Schwede, T. (2018). SWISS-MODEL: homology modelling of protein structures and complexes. *Nucleic Acids Res*, *46*(W1), W296-W303. https://doi.org/10.1093/nar/gky427

Wirth, M., Zhang, W., Razi, M., Nyoni, L., Joshi, D., O'Reilly, N., Johansen, T., Tooze, S. A., & Mouilleron, S. (2019). Molecular determinants regulating selective binding of autophagy adapters and receptors to ATG8 proteins. *Nat Commun*, *10*(1), 2055. https://doi.org/10.1038/s41467-019-10059-6

Yamamoto, H., Kakuta, S., Watanabe, T. M., Kitamura, A., Sekito, T., Kondo-Kakuta, C., Ichikawa, R., Kinjo, M., & Ohsumi, Y. (2012). Atg9 vesicles are an important membrane source during early steps of autophagosome formation. *J Cell Biol*, *198*(2), 219-233. https://doi.org/10.1083/jcb.201202061

Yla-Anttila, P., Vihinen, H., Jokita, E., & Eskelinen, E. L. (2009). 3D tomography reveals connections between the phagophore and endoplasmic reticulum. *Autophagy*, *5*(8), 1180-1185. <Go to ISI>://WOS:000275580800012

Young, L. N., Goerdeler, F., & Hurley, J. H. (2019). Structural pathway for allosteric activation of the autophagic PI 3-kinase complex I. *Proc Natl Acad Sci U S A*, *116*(43), 21508-21513. https://doi.org/10.1073/pnas.1911612116

Yuan, F., Alimohamadi, H., Bakka, B., Trementozzi, A. N., Day, K. J., Fawzi, N. L., Rangamani, P., & Stachowiak, J. C. (2021). Membrane bending by protein phase separation. *Proc Natl Acad Sci U S A*, *118*(11). https://doi.org/10.1073/pnas.2017435118

Zeno, W. F., Thatte, A. S., Wang, L., Snead, W. T., Lafer, E. M., & Stachowiak, J. C. (2019). Molecular Mechanisms of Membrane Curvature Sensing by a Disordered Protein. *J Am Chem Soc*, *141*(26), 10361-10371. https://doi.org/10.1021/jacs.9b03927

Zhou, X., Hu, J., Zhang, C., Zhang, G., & Zhang, Y. (2019). Assembling multidomain protein structures through analogous global structural alignments. *Proc Natl Acad Sci U S A*, *116*(32), 15930-15938. https://doi.org/10.1073/pnas.1905068116